

This dissertation has been 63-2955
microfilmed exactly as received

ANDERSON, James Robert, 1932-
THE FERMI SURFACE OF LEAD.

Iowa State University of Science and Technology
Ph.D., 1962
Physics, solid state

University Microfilms, Inc., Ann Arbor, Michigan

THE FERMI SURFACE OF LEAD

by

James Robert Anderson

A Dissertation Submitted to the
Graduate Faculty in Partial Fulfillment of
The Requirements for the Degree of
DOCTOR OF PHILOSOPHY

Major Subject: Physics

Approved:

Signature was redacted for privacy.

In Charge of Major Work

Signature was redacted for privacy.

Head of Major Department

Signature was redacted for privacy.

Dean of Graduate College

Iowa State University
Of Science and Technology
Ames, Iowa

1962

TABLE OF CONTENTS

	Page
ABSTRACT	x
1. INTRODUCTION	1
1.1. The Fermi Surface	1
1.2. Brillouin Zones: Reduced and Extended Zone Pictures	3
1.3. Experimental Methods for Studying the Fermi Surface	9
1.3.1. Kohn effect	9
1.3.2. Ultrasonic attenuation in a magnetic field	10
1.3.3. Anomalous skin effect	13
1.3.4. Magnetoresistance	14
1.3.5. Cyclotron resonance	16
1.4. de Haas-van Alphen Effect	19
1.5. Outline of the Present Investigation	23
2. EXPERIMENTAL PROCEDURE	25
2.1. General Considerations	25
2.2. Pulse System	28
2.3. de Haas-van Alphen Signal	44
2.4. Rotating System	50
2.5. Samples and Preparation	53
2.6. Cryostats and Pumping System	54

	Page
3. OSCILLATION PERIODS AND AMPLITUDES: THEIR MEASUREMENT AND THEIR ERRORS	60
3.1. Examination of Photographs and Period Measurements	60
3.2. Errors	75
3.3. Amplitude Measurements	84
4. EXPERIMENTAL RESULTS	90
4.1. The Empty Lattice or Single OPW Model for Lead	90
4.2. Period Measurements for Symmetry Orientations	94
4.3. Orientation Dependence of dHVA Periods	103
4.4. Cyclotron Mass Measurements	109
4.5. Comparison of Experimental and Calculated Amplitudes	112
5. DESCRIPTION OF THE FERMI SURFACE	115
5.1. Introduction	115
5.2. Fourier Expansion Method	115
5.3. Orthogonalized-Plane-Wave Method	118
5.4. Determination of the Fermi Surface	126
6. COMPARISON OF EXPERIMENTAL AND CALCULATED RESULTS	146
6.1. dHVA Effect	146
6.1.1 Extremal areas at symmetry directions	146
6.1.2. Orientation dependence	153
6.1.3. Angular range for the existence of orbits	155

	Page
6.1.4. Cyclotron mass and electronic specific heat	157
6.2. Extremal Dimensions of the Fermi Surface	169
6.2.1. Kohn effect	169
6.2.2. Magnetoacoustic effect	173
6.3. Surface Area	174
6.4. Open Orbits	179
6.5. Fitting the β Oscillations into a Particular Model of the Fermi Surface	184
7. CONCLUDING DISCUSSION AND SUGGESTIONS FOR FURTHER STUDY	189
8. PRELIMINARY DHVA STUDIES OF IRON	194
9. REFERENCES	200
10. ACKNOWLEDGEMENTS	206
11. APPENDIX	208
11.1. Appendix A: Determination of Constant Energy Curves Near U	208
11.2. Appendix B: Determination of Constant Energy Curves about W	217
11.3. Appendix C: Spin-Orbit Coupling	225

LIST OF TABLES

Table		Page
4.1	dHvA periods and extremal areas for lead	100
4.2	Comparison of calculated and experimental pickup voltages	114
6.1	Angular range for existence of orbits	156
6.2	Cyclotron masses	160
6.3	Adjusted single OPW masses compared with experimental masses	167
6.4	Extremal dimensions of Fermi surface of lead	171
6.5	Effect of Bragg planes on surface area	177

LIST OF FIGURES

Figure		Page
1.1	Remapping procedure for a constant energy contour for a two-dimensional square lattice	6
1.2	Examples of open orbits	8b
1.3	Illustration of the Kohn effect	11
1.4	Drift velocity for different types of extremal orbits	18
2.1	Block diagram of dHVA equipment	27
2.2	Circuit for charging and discharging capacitor bank	30
2.3	Schematic drawing of pulse coil	32
2.4	Field profiles for a pulse solenoid	34
2.5a	Pulse coil compensation circuit	36
2.5b	Twin T filter circuit	36
2.6	Nuclear magnetic resonance circuit for calibration of pulse coils	38
2.7	Examples of current through the pulse solenoid	41
2.8	Diagram of calibration and bucking circuit: Part I	42
2.9	Diagram of calibration and bucking circuit: Part II	43
2.10	Sample holders, pickup coils, and rotating mechanism	47
2.11	Preamplifier and filter for dHVA signal	49
2.12	Block diagram of sample orientation circuit	52
2.13	Schematic diagram of stainless steel helium cryostat	55b

Figure		Page
2.14a	Helium cryostat	57
2.14b	Liquid nitrogen container	57
3.1	Examples of dHvA oscillations in lead	62
3.2	Examples of dHvA oscillations in lead	65
3.3	Plot of $1/H$ at oscillation maxima versus integers	67
3.4	Plot of $1/H$ at oscillation maxima versus integers	69
3.5	Envelope of transient resonance, gliding tone effect	72
4.1	Fundamental Brillouin zone for the fcc lattice	91
4.2	Fermi surfaces of fcc metals according to the single OPW approximation	93
4.3	Single OPW model of third band Fermi surface of lead	96
4.4	Pipe model of third band Fermi surface of lead	97
4.5	Orientation dependence of dHvA periods in a (100) plane	105
4.6	Single OPW areas normal to the $[001]$ direction	107
4.7	Plot of $\log_{10} A/T$ versus T for β and γ oscillations	111
5.1	Fermi surface of copper	119b
5.2	OPW matrix elements in zinc	125
5.3	Orbit ζ	130
5.4	$\star \zeta$ versus V_{111}	131
5.5	$\star \zeta$ versus V_{200}	132

Figure		Page
5.6	'Windmill' orbit ν	135
5.7	\star_{ν} versus V_{111}	136
5.8	\star_{ν} versus V_{200}	137
5.9	Matrix elements versus K for different metals	140
5.10	Modification of the free-electron sphere by the lattice potential for a (110) cross-section through Γ	142
5.11	$E(\underline{k})$ along symmetry lines	143
5.12	$E(\underline{k})$ along symmetry lines	144
6.1	Second-band and third-band Fermi surfaces for a (110) section through Γ	147
6.2	Third-band orbit ω	148
6.3	Hole surface for a (100) section through Γ	149
6.4	Third-band orbits ξ and η	150
6.5	$[111]$ orbits: α , ζ , θ , and σ	151
6.6	Orientation dependence of dHvA periods calculated from the two-parameter models	154
6.7	Plot of \star versus E for the orbits $[100]$ ν and $[110]$ ω	158
6.8	Plot of \star versus E for the orbits $[110]$ ζ and $[110]$ α	159
6.9a	Modified velocities for the $[110]$ ζ orbit	164
6.9b	Modified velocities for the $[100]$ ν orbit	164
6.10	Phonon dispersion curve for lead	170
6.11	Modification of free-electron sphere by a Bragg plane	176

Figure		Page
6.12	Stereogram of magnetic field directions for which open orbits were found to exist	180
6.13	Type I open orbits as given by the single OPW model	182
6.14	Type I open orbit as given by the single OPW model	183
8.1	Examples of dHvA oscillations in iron	195b
8.2	Derivative method for determining periods in iron	199
11.1	Plot of second-band and third-band constant energy surfaces for a (110) section through Γ	212
11.2	$E(\underline{k})$ curves along the symmetry line U - W	214
11.3	Plot of second-band and third-band constant energy surfaces for a (100) section which contains orbit ν	222
11.4	Plot of second-band and third-band energy surfaces for a (110) section which contains orbit W	224
11.5	$E(\underline{k})$ along the symmetry line U - W showing the effect of spin-orbit coupling	232
11.6	$E(\underline{k})$ along the symmetry line U - W showing the effect of spin-orbit coupling	233
11.7	Energy levels at W as a function of the spin-orbit coupling parameter	236

ABSTRACT

Knowledge of the Fermi surface is one of the most important requirements for understanding the properties of a metal. A very powerful tool for studying this surface is the de Haas-van Alphen effect, the oscillations in the magnetic susceptibility with magnetic field found in metal single crystals at very low temperatures. Gold originally studied the de Haas-van Alphen effect in lead using pulsed magnetic fields up to a maximum of 80 kG. His results indicated that the Fermi surface was much like a free-electron surface, and that valuable additional information should become available by extending the measurements to higher fields. In the present study an apparatus has been designed and constructed to extend the magnetic fields to 200 kG. With the aid of these higher fields many new features of the Fermi surface in lead have been quantitatively determined. The shape of the Fermi surface can be well explained in terms of an orthogonalized-plane-wave model using only two parameters, the two Fourier components of the pseudopotential, V_{111} and V_{200} . While the orthogonalized-plane-wave approach is successful in describing the shape of the Fermi surface, the calculated cyclotron masses are too small by a factor of order two. The theoretical implications of this are discussed briefly. Shortly before this thesis was completed, de Haas-van Alphen oscillations

were observed in iron whiskers, the first time that the effect has been observed in a ferromagnetic metal. Preliminary results show that the saturation magnetization in iron must be taken into account in order to determine the true periods of the oscillations.

1. INTRODUCTION

1.1. The Fermi Surface

The Fermi surface of a metal is defined as the constant energy surface in momentum space at which there is a discontinuity in the momentum distribution of the electrons at absolute zero. Knowledge of the shape of this Fermi surface is very important in understanding the properties of a metal. For example, the electrical conductivity of a metal is determined by the scattering of electrons and this scattering can only take place between initial and final states which lie close to the Fermi surface.

When one notes that electron-electron interactions are of the same order of magnitude as the kinetic energy of an electron, it seems at first sight surprising that a discontinuity in the momentum distribution could exist. This problem has been given a great amount of theoretical attention recently,¹ and Luttinger in collaboration with Kohn and Ward (Luttinger 1960; Luttinger and Ward 1960) has treated the electron-electron interaction and, to all orders of perturbation theory, the existence of such a discontinuity has been obtained. From the experimental point of view, as we shall see later, there is no doubt about the existence of a well-

¹See Luttinger (1961) and Falicov and Heine (1961) who give further references.

defined Fermi surface.

In order to calculate many physical properties, such as transport behavior, scattering probabilities are needed in addition to details of the Fermi surface, and the theoretical expressions usually take the form of complicated integrals from which it is in general impossible to separate out the details of the Fermi surface. However, there is a class of experiments which depends principally on the details of the Fermi surface and to only a lesser extent on scattering probabilities. Such experiments are the de Haas-van Alphen (dHvA) effect, cyclotron resonance effect, magnetoresistance effect, magnetoacoustic effect, and the Kohn effect. In general, the quantum mechanical theories used for interpretation of the results of these experiments are based on the one electron approximation. In reality, one is dealing with a system of interacting particles; but, as several authors have shown, the system can be described in terms of individual 'quasi-particles' which are uncorrelated. (See, for example, Pines 1955.)

The main experiments giving direct information about the Fermi surfaces of metals have been described in several reviews (Pippard 1961; Harrison and Webb 1960; Lax 1958), and we will give only a short summary of these experiments in Section 1.3. In order to clarify this discussion we begin with a review of the concept of Brillouin zones in the follow-

ing section.

1.2. Brillouin Zones: Reduced and Extended Zone Pictures

If the crystal lattice were ignored, the energy surfaces for a system of independent electrons would be spheres in momentum space; this space we shall also refer to as the reciprocal lattice or wave vector space (k-space). In this case the radius of the Fermi sphere (the constant energy surface enclosing all the occupied states at absolute zero) would be $k_F = (3\pi^2 n)^{1/3}$ where n is the density of free 'conduction' electrons in the metal.

When a small lattice potential is added thus creating a periodic structure, the primary effect is to produce planes of energy discontinuity in k-space defined by the equation $k^2/2 = \underline{k} \cdot \underline{K}$ where \underline{K} is a vector of the reciprocal lattice and the magnitude of \underline{k} is $2\pi/\lambda$ (Brillouin 1953). These planes, called Bragg planes, break up the reciprocal lattice into zones. The region cut off by those planes nearest the origin of the reciprocal lattice is a polyhedron called the first Brillouin zone. (Any figure with the same boundaries as the first Brillouin zone will be referred to as the primitive zone or cell.) The second zone is made up of all regions of k-space that can be reached from the origin by crossing only one Bragg plane. The third zone is found by crossing

two Bragg planes and so on. It can be shown that all Brillouin zones have the same volume and can be mapped into the primitive zone by reciprocal lattice translations \underline{K} (Brillouin 1953, p. 243).

The importance of this division into Brillouin zones may be seen by considering the motion of an electron in k -space. Using a semiclassical approach, we assume that the electron is a localized particle whose motion in an electromagnetic field is described by the equation

$$\hbar \frac{d\underline{k}}{dt} = \underline{F} \quad (1.1)$$

where \underline{F} is the Lorentz force. If only a quasi-steady magnetic field, \underline{H} , is present, Equation 1.1 becomes

$$\hbar \frac{d\underline{k}}{dt} = \frac{e\underline{r} \times \underline{H}}{c} \quad (1.2)$$

where $\dot{\underline{r}}$ is the velocity of the electron. Thus we see that in k -space the electron moves around an orbit that is the intersection of a constant energy surface with a plane normal to \underline{H} . (Also, from Equation 1.2 we see that the orbit in real space is related to the orbit in k -space by a scaling factor $\frac{c\hbar}{eH}$.) If this orbit intersects a Bragg plane, in general the plane will not be crossed because of the energy gap, and the electron will be 'Bragg reflected' (The wave vector is changed by a reciprocal lattice vector.) to an equivalent point on the

boundary of the zone from which it will continue along the orbit. Thus the orbit will remain in only one zone and if this zone is remapped into the primitive zone, the orbit will appear continuous.

This remapping consists of displacing each section by an appropriate reciprocal lattice translation in order to bring it into the primitive zone. The result is called the reduced-zone scheme. Pippard (1961) has shown a good example of this remapping procedure for a two-dimensional square lattice (Figure 1.1); the constant energy contour was originally a circle, but it has been broken up by the Bragg planes. We see that the second zone contour maps into a square shape, the third forms a star and the fourth forms small pockets at the corners of the remapped zone. The energy varies continuously with k in each remapped zone which we shall often refer to as a band.

When the lattice potential (or pseudopotential described in Section 5.2) is allowed to vanish but symmetry is maintained, the only effect is to alter the connectivity of the constant energy spheres as they intersect the Bragg planes. This is called the 'empty lattice' or 'single-orthogonalized-plane-wave' approximation. The spherical free electron surface is divided into portions, each of which may be mapped into the primitive zone in the manner pictured above. This procedure was used by Gold (1958b) in describing the Fermi

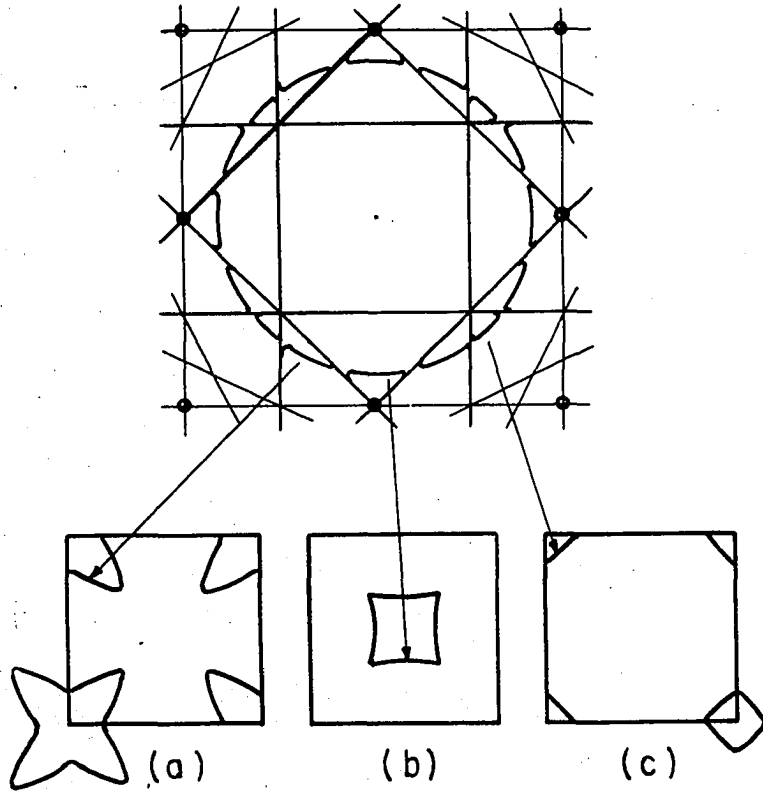


Figure 1.1. Remapping procedure for a constant energy contour for a two-dimensional square lattice

(after Pippard 1961)

- a. Third zone
- b. Second zone
- c. Fourth zone

surface of lead. This method can be extremely complicated in three dimensions, but Harrison (1959) has described a method for carrying out this mapping simply. Harrison's method consists of drawing free-electron spheres about each reciprocal-lattice point. The regions enclosed by only one sphere are occupied regions belonging to the first zone. Those enclosed by two spheres belong to both the first and second zones, and so on.

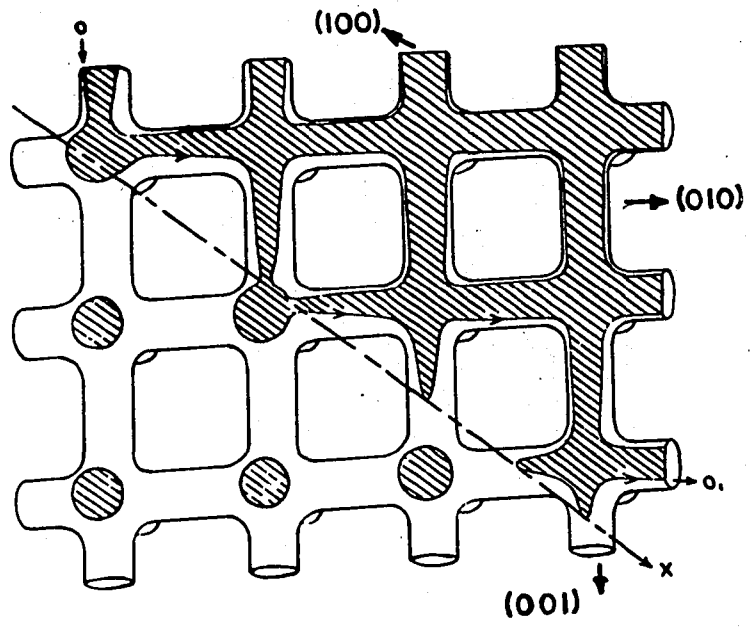
The primitive zone may be considered as a repeating unit of the reciprocal lattice and when this is done we have the 'repeated-zone scheme'. In this case, crossing a Bragg plane into an identical neighboring cell is equivalent to Bragg reflection.

Sometimes the remapping produces a multiply-connected Fermi surface and in this case the possibility of open orbits exists. The idea of open orbits is best discussed with a picture using this repeated zone scheme. Figure 1.2a shows an example (Chambers 1960, p. 110) of an open orbit running in the $[010]$ direction for a periodically repeating Fermi surface of intersecting $[100]$ cylinders. The electron path extends indefinitely in this repeated zone scheme. The concept of open orbits will be important when we discuss magnetoresistance in the next section.

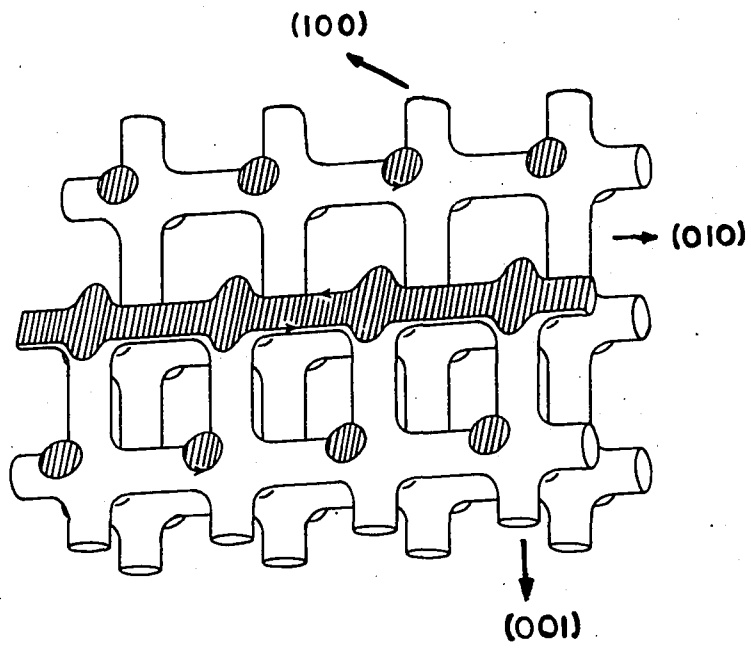
Figure 1.2. Examples of open orbits (Chambers 1960)

a. H in (010) plane

b. H tilted away from [100] in an arbitrary direction



b.



a.

1.3. Experimental Methods for Studying the Fermi Surface

1.3.1. Kohn effect

Although the Kohn effect has been found in only one metal, lead (Brockhouse et al. 1961), we will begin with this experiment because of its essential simplicity. In this experiment the dispersion curves for lattice vibrations are determined by inelastic scattering of low energy neutrons or x-rays. Kohn (1959) has predicted the occurrence of kinks in these curves, theoretically corresponding to logarithmic infinities of slope. For a simply-connected convex Fermi surface Woll and Kohn (1962) show that these kinks should occur at values of phonon wave vector satisfying the relation $\underline{q} + \underline{K} = 2\underline{k}_F$, where \underline{K} is a reciprocal lattice vector and \underline{k}_F is a wave vector on the Fermi surface. It seems reasonable to extend this result to more complex forms of the Fermi surface by assuming \underline{q} satisfies

$$\underline{q} + \underline{K} = \underline{D}_e \quad (1.3)$$

where \underline{D}_e is an extremal distance ('calipered' dimension) across the Fermi surface. Thus we have a method for obtaining extremal dimensions of the Fermi surface.

Physically the Kohn effect is due to the influence of conduction electrons on the effective forces between ion cores.

Let us, for simplicity, consider a spherical Fermi surface and assume $\underline{K} = 0$. A phonon with wave vector \underline{q} propagates through the lattice creating electron-hole pairs with zero energy loss. This can be pictured as the scattering of an electron from one part of the Fermi surface to another.

Figure 1.3 shows the spherical Fermi surface in a repeated zone scheme. When $|\underline{q}|$ becomes greater than the diameter of the Fermi surface $2k_F$, this scattering can no longer take place and the shielding of the ion cores by the conduction electrons will decrease sharply. This decrease in shielding increases the forces between the ions and the phonon frequency will increase as shown in the kink at (c). Similarly, downward kinks can occur when $|\underline{q} + \underline{K}|$ passes from outside to inside the Fermi surface as \underline{q} increases; such kinks are shown at (e) and (f). Brockhouse et al. (1961) have studied this effect in some detail in lead and their results will be discussed in Chapter 6. Paskin and Weiss (1962) have also found similar kinks in the dispersion curve using x-rays.

1.3.2. Ultrasonic attenuation in a magnetic field

Attenuation of sound waves in a magnetic field is another approach for studying the Fermi surface and, in fact, gives similar information to that obtained from the Kohn effect. In this experiment the electron mean free path must be longer than the sound wavelength and therefore very pure metals and

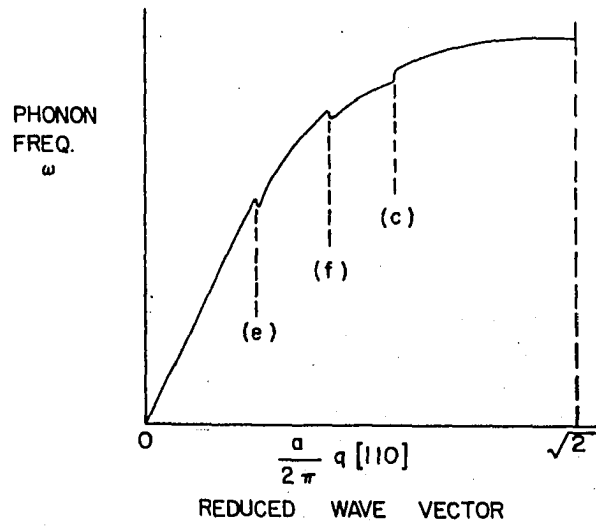
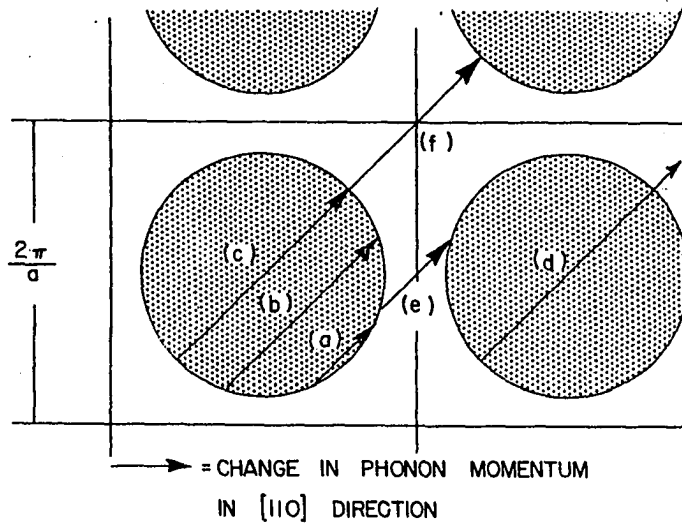


Figure 1.3. Illustration of the Kohn effect

liquid helium temperatures are required. The results are rather complicated and sometimes difficult to interpret. Pippard (1960a) has considered this problem for arbitrary Fermi surfaces and found oscillations quasi-periodic in $1/H$ may occur which depend on 'calipered' dimensions of the Fermi surface normal to the magnetic field and the direction of sound propagation. Cohen, Harrison, and Harrison (1960) have looked at the problem in detail for a free electron gas in a background of positive charge of the same density. For the skin depth much less than the sound wavelength λ and for waves propagating perpendicular to the magnetic field direction, they show that maxima in attenuation occur at

$$qR = n\pi \text{ as } qR \rightarrow \infty. \quad (1.4)$$

Here $q = 2\pi/\lambda$ and R is the radius of the orbit in real space. Using the scaling factor which relates orbits in real space in a magnetic field \underline{H} to those in k -space, we may write Equation 1.4 as

$$D_e = \frac{e\lambda}{\hbar c \Delta(1/H)} \quad (1.5)$$

Here D_e should be the same extremal dimension of the Fermi surface as in the Kohn effect, and $\Delta(1/H)$ is the period of the oscillations. Using longitudinal waves, Rayne (1962, p. 223) has observed several oscillations in attenuation in very pure

lead samples and used Equation 1.5 to estimate extremal dimensions of the Fermi surface. We shall return to a discussion of these results in Chapter 6.

1.3.3. Anomalous skin effect

In this experiment microwaves are incident upon the plane surface of a sample and the surface resistance is determined by measuring the power absorbed. In the extreme anomalous limit (skin depth much less than mean free path) the surface impedance (Pippard 1960b) is given by

$$Z_{\omega} = \alpha \frac{\pi\omega}{S} (1 - \sqrt{3} i) \quad (1.6)$$

where $S^3 = \frac{we^2}{\pi\hbar} \int |\rho_y| dk_y$ and α is a number between 1 and 2 which depends upon the behavior of electrons hitting the surface ($\alpha = \sqrt{3}$ for diffuse scattering). ρ_y is the radius of curvature in a plane normal to the sample surface at an 'effective point' where $\nabla_k E$ has no component normal to the sample surface.

Study of the anomalous skin effect has been quite valuable for metals with single-sheet Fermi surfaces such as copper (Pippard 1957). For a metal with a Fermi surface of several sheets, however, the contributions from all sheets are combined in the surface resistance and can not be separated. In general for such metals the anomalous skin effect can be used

to determine only the total area of the Fermi surface, S , from the average of $(R_{\infty})_{av}^{-3}$ over all surface orientations according to the formula

$$(R_{\infty})_{av}^{-3} = \frac{e^2 S}{(4)(3^{3/2})\pi^4 \hbar \omega^2} \quad (1.7)$$

Here R_{∞} is the real part of the surface impedance and $(R_{\infty})_{av}^{-3}$ is obtained by averaging over all current directions parallel to the sample surface for a fixed crystal surface orientation. However, S is most readily determined from measurements of $(\overline{R_{\infty}})_{av}$ on polycrystalline samples. Here one must assume that $(R_{\infty})_{av}^{-3}$ can be replaced by $(\overline{R_{\infty}})_{av}^{-3}$ and that the crystallites have no preferred orientation.

1.3.4. Magnetoresistance

The study of the resistance of metals in the limit of large magnetic fields is one of the simplest methods for investigating the connectivity of the Fermi surface. That is, the regions of existence of open orbits can be found from a study of magnetoresistance as a function of crystal orientation. Lifshitz, Azbel, and Kaganov (1957) have worked out the theory of magnetoresistance for an arbitrary dispersion relation using a linearized Boltzmann equation. The results for compensation (equal numbers of holes and electrons causing cancellation of the linear Hall term σ_{xy} in the conductivity

tensor) are quite different from those for non-compensation.

The presence of open orbits is determined by saturation or nonsaturation of the magnetoresistance in the limit of large magnetic fields. The longitudinal magnetoresistance (current in direction of magnetic field) always saturates, but for the transverse magnetoresistance there are several possibilities:

a. For an uncompensated metal saturation occurs for all directions of field and current, if there are either no open orbits or open orbits in two perpendicular directions. For open orbits in only one direction nonsaturation occurs for all directions of magnetic field perpendicular to the open orbit direction except for current perpendicular to both the field and open orbit directions; in this case saturation occurs and the open orbit direction is determined.

b. In the case of a compensated metal, nonsaturation occurs for all directions of field and current if there are no open orbits. For open orbits, the results for a compensated metal are the same as for an uncompensated one.

Alekseevskii and Gaidukov have used the above considerations quite successfully in their study of the magnetoresistance of tin (Alekseevskii et al. 1961) and lead (Alekseevskii and Gaidukov 1962).

Study of the Hall coefficient R_H for large magnetic fields can also help to determine whether open or closed

orbits are present. For closed orbits or open orbits in only one direction the Hall coefficient tends to a constant value at high fields. On the other hand, for open orbits in two directions $R_H \rightarrow 1/H^2$ as $H \rightarrow \infty$. So far very little use has been made of the high-field Hall coefficient in metals.

1.3.5. Cyclotron resonance

Cyclotron resonance in metals, Azbel-Kaner effect (Azbel and Kaner 1956, 1957), is used to determine the cyclotron mass, which is a differential property of the Fermi surface. Here a magnetic field is applied parallel to the specimen surface with an rf electric field perpendicular to the magnetic field. A series of resonances periodic in $1/H$ is observed and the cyclotron mass m^* is obtained from this period according to the formula

$$m^* = \frac{e}{c\omega} \frac{1}{\Delta(1/H)}, \quad (1.8)$$

where ω is the frequency of the electromagnetic field. The cyclotron mass is defined as

$$m^* = \frac{\hbar^2}{2\pi} \frac{dA}{dE_F} \quad (1.9)$$

where A is the area enclosed by the orbit formed by the intersection of an energy surface with a plane $k_z = \text{constant}$, perpendicular to the magnetic field; the energy derivative is

evaluated at the Fermi surface.

In practice it is difficult to align the magnetic field exactly parallel to the specimen surface and also the surface is not perfectly smooth. Therefore, this experiment usually picks out sections of the Fermi surface for which $\bar{v}_z = 0$, where \bar{v}_z is the average velocity in the direction of the magnetic field. Harrison (1960b) has shown that $\bar{v}_z = 0$ for an extremal orbit, that is, for $\frac{\partial A}{\partial k_z} = 0$.

Usually the extremal section will lie in a plane of mirror symmetry where $v_z = 0$ at all points on the orbit. Figure 1.4a shows such an orbit. However, one frequently finds extremal sections that do not lie in a mirror plane and where only the average velocity \bar{v}_z is zero; Figure 1.4b is an example of this. One can distinguish between these two possibilities by varying the rf polarization. If resonance is observed with current parallel to the field, it must be due to an orbit for which only the average value $\bar{v}_z = 0$. Such polarization studies have been carried out by Young (ca. 1962), Khaikin and Mina (1962), and Kip, Langenberg, and Moore (1961). In general it is not possible to associate the cyclotron mass directly with the relevant orbit without additional information, but this difficulty is not present in the de Haas-van Alphen effect which we discuss in Section 1.4.

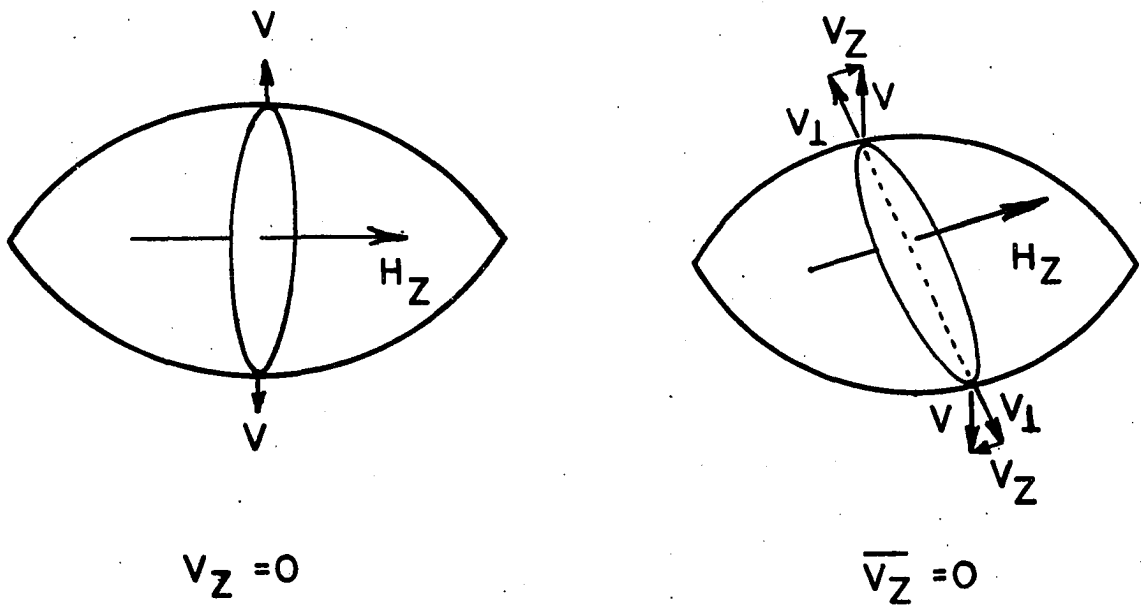


Figure 1.4. Drift velocity for different types of extremal orbits

1.4. de Haas-van Alphen Effect

In the present investigation the de Haas-van Alphen effect was used to study the Fermi surface and we therefore discuss this experiment in somewhat more detail.

The de Haas-van Alphen (dHvA) effect, oscillations of magnetic susceptibility periodic in $1/H$ observed in metal single crystals at low temperatures, is one of the most powerful tools for studying the shape of the Fermi surface and its differential properties.

The existence of oscillations can be shown in a relatively simple manner by considering the effect of a uniform magnetic field \underline{H} in the z direction. It is assumed that the motion of an electron in a state with wave number \underline{k} is described by the Lorentz force equation

$$\hbar \dot{\underline{k}} = \frac{e}{c} \underline{v} \times \underline{H} \quad (1.1)$$

where $\underline{v} = \frac{1}{\hbar} \nabla_{\underline{k}} E$ represents the electron velocity. In the presence of the magnetic field electrons move in quantized orbits in the $x - y$ plane while the motion in the z direction is not affected.

Onsager (1952) applied the Bohr-Sommerfeld quantization rule to this problem for an arbitrary dispersion law $E(\underline{k})$:

$$\oint \underline{p} \cdot d\underline{q} = (n + \gamma) 2\pi\hbar \quad ; \quad (1.10)$$

where \underline{p} is the momentum canonically conjugate to the space coordinate \underline{q} in the presence of the magnetic field. He found that the quantized orbits in k -space enclose areas given by

$$A = \frac{2\pi(n + \gamma)eH}{hc} \quad (1.11)$$

Here γ is a constant and equals $1/2$ in the free electron case.

Since k_z is not affected by quantization, we consider a thin disk in k -space of thickness δk_z . The quantized levels can then be thought of as cylinders with height δk_z and enclosing the cross-sectional areas A . It can be shown that the Fermi energy shifts very little with field and that this effect can be neglected (Pippard 1961, p. 23). As H increases the cylinders expand according to Equation 1.11 and eventually pass through the Fermi surface. The energy of the system U fluctuates with a period determined by the rate at which these cylinders move through the Fermi surface. For a disk at k_z this period becomes

$$P = \Delta(1/H) = \frac{2\pi e}{hc A(k_z)} \quad (1.12)$$

where $A(k_z)$ is the cross-sectional area of the Fermi surface at k_z . The magnetization, given by $-dU/dH$ at $0^\circ K$, oscillates with the same period and can be expressed in a Fourier series in the form

$$\delta M(k_z) = \sum_r C_r(k_z) \sin \left[\frac{2\pi e r}{\hbar c A(k_z)} \left(\frac{1}{H} \right) \right] \delta k_z. \quad (1.13)$$

Because the phase of oscillations is large, typically 10^3 - 10^4 for metals, the extremal values of $A(k_z)$ predominate when we integrate over k_z . If higher harmonics are neglected, the magnetization oscillates with period

$$P = \frac{2\pi e}{\hbar c A_0}, \quad (1.14)$$

where A_0 is an extremal area of the Fermi surface normal to H , as for example in Figure 1.4. In real metals several periods may be found since the Fermi surface may have several extremal areas. Because of the periodic nature of the effect it is possible, as with cyclotron resonance and the magneto-acoustic effect, to separate out the contributions from different extremal sections.

We have considered the effect only at absolute zero, but at higher temperatures the Fermi surface is no longer sharply defined and the amplitudes of the oscillations decrease.

Lifshitz and Kosevich (1955) have calculated the oscillatory part of the magnetization for an arbitrary dispersion law including the effects of a finite temperature as well as a spin term. The result is that the oscillating part of the magnetization for a uniform applied magnetic field, H , in the z direction is given by:

$$\frac{M_{osc}}{V} = \frac{2kT}{\sqrt{2\pi}} \left(\frac{e}{\hbar c}\right)^{\frac{3}{2}} \left(\frac{\hbar c A_0(E_F)}{2\pi e}\right) \left|\frac{\partial^2 A}{\partial k_z^2}\right|_0^{-\frac{1}{2}} H^{-\frac{1}{2}} \times \quad (1.15)$$

$$\sum_{r=1}^{\infty} \frac{\sin \left[\frac{\hbar c A_0(E_F)}{eH} + \frac{\pi}{4} - 2\pi r \gamma \right] \cos \frac{\pi r m^*}{m}}{r^{\frac{1}{2}} \sinh \lambda r}$$

Here V is the volume of the sample, and $A_0(E_F)$ is the extremal area of the Fermi surface in a plane normal to the magnetic field given in wave vector units, cm^{-2} . The cyclotron mass is defined as in Section 1.3 by $m^* = \frac{\hbar^2}{2\pi} \frac{\partial A_0}{\partial E_F}$. Here

$$\lambda = \frac{2\pi^2 m^* ckT}{e\hbar H} \quad \text{and} \quad \left|\frac{\partial^2 A}{\partial k_z^2}\right|_0 \quad \text{is the magnitude of a curvature}$$

factor and shows that the amplitude is greater if the cross-sectional area changes only slowly about an extremum. γ is a phase factor which would be $1/2$ for a quadratic dispersion law. In general λ is large enough that only one term need be kept in the summation and $(\sinh \lambda)^{-1}$ becomes $2e^{-\lambda}$.

Equation 1.15 neglects collision broadening and Dingle (1952) has shown that each harmonic in the summation should be multiplied by a term of the form

$$e^{-\frac{2\pi^2 r m^* ckx}{e\hbar H}}$$

to take this into account. $x = \frac{\hbar}{\pi k \tau}$ is an effective temperature which is found experimentally to be of the order of $1^\circ - 2^\circ \text{K}$, and τ is an appropriate relaxation time. Equation 1.15 can be written in the form

$$M_{\text{osc}} \cong M_0(H, T) \sin \left[\frac{\hbar c A_0(E_F)}{eH} + \frac{\pi}{4} - 2\pi\gamma \right] \quad (1.16)$$

where $M_0(H, T)$ varies only slowly with H .

From Equation 1.16 extremal areas of the Fermi surface normal to the magnetic field can be calculated from the periods of oscillations, and by studying the orientation dependence of these periods the shape of the Fermi surface can be inferred. Furthermore, from the variation of $M_0(H, T)$ with temperature and magnetic field the cyclotron mass and the collision broadening temperature, respectively, can be determined.

1.5. Outline of the Present Investigation

In the work presented here the de Haas-van Alphen effect has been studied in lead and the results used to describe the Fermi surface. Gold (1958b) originally investigated this effect in lead using pulsed magnetic fields up to a maximum of 80 kG. His results indicated that the Fermi surface was much like a free-electron surface and according to this model additional valuable information should become available by

extending such measurements to higher fields. Therefore, in the present study an apparatus was designed and constructed to extend the range of pulsed fields to 200 kG and this is described in Chapter 2. In Chapter 3 the measurements are described and possible errors are considered. As was hoped, several new de Haas-van Alphen periods were found for the magnetic field along symmetry directions; these results are described in Chapter 4. From these measurements many new features of the Fermi surface have been quantitatively determined. In fact, the shape of the Fermi surface can be well explained in terms of an orthogonalized-plane-wave model using only two parameters, two Fourier components of the pseudo-potential, V_{111} and V_{200} . This calculation is described in Chapter 5. In Chapter 6 the two parameter model is related to various experimental results. In Chapter 7 the results are summarized and some suggestions for further study are made. In addition some preliminary results on the de Haas-van Alphen effect in iron whiskers are reported in the last chapter.

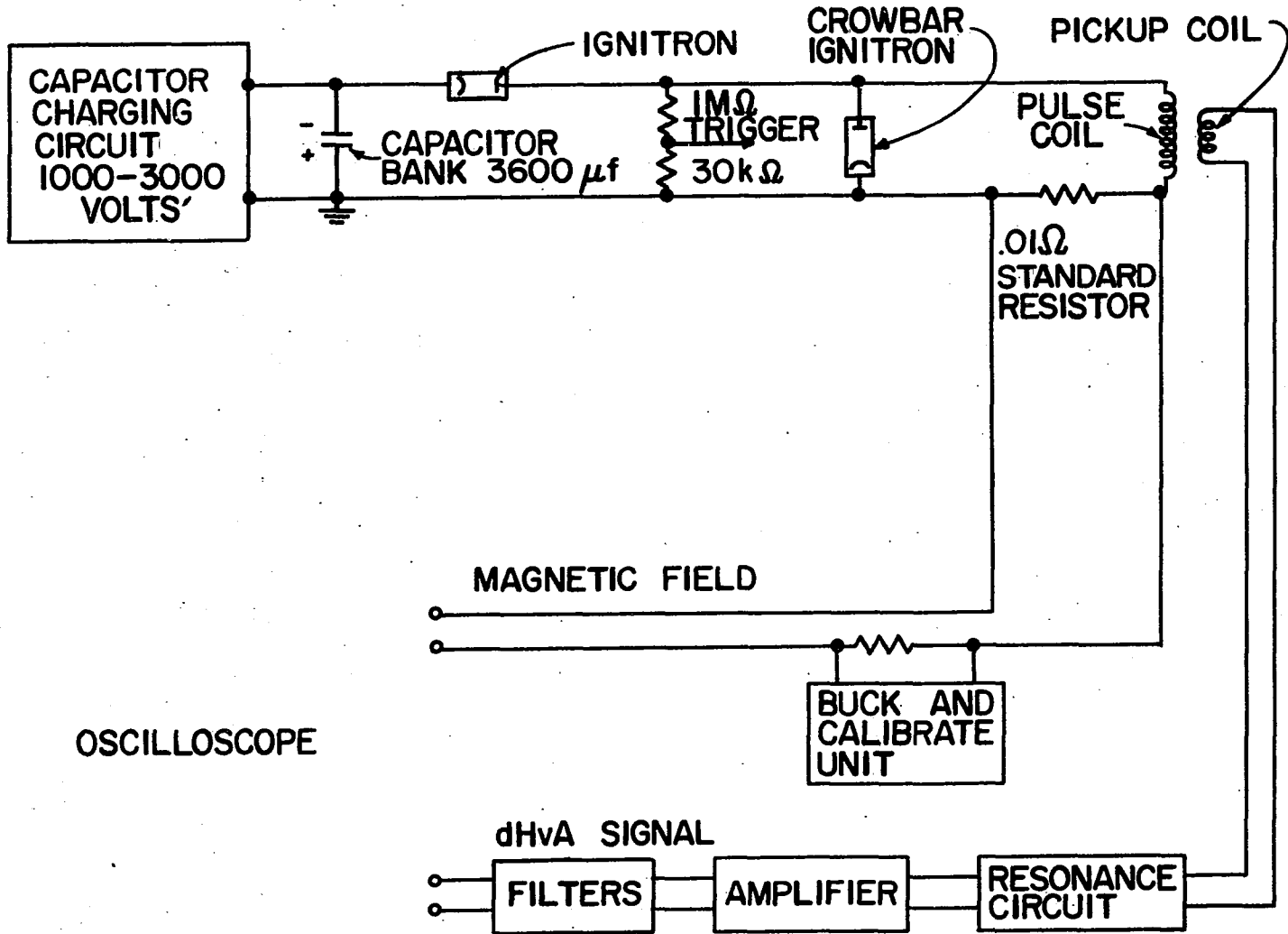
2. EXPERIMENTAL PROCEDURE

2.1. General Considerations

In the present study measurements of the magnetic susceptibility of lead single crystals were carried out at low temperatures using the pulsed field technique developed originally by Shoenberg (1957). These measurements required extremely homogeneous, large, magnetic fields and temperatures between 1°K and 4°K. The equipment that was constructed to satisfy these requirements will be described in succeeding sections.

Figure 2.1 shows a block diagram of the experimental apparatus. The sample, a tiny needle of lead in this case, is put inside a compensated pickup coil which is then placed at the center of a pulse solenoid. A time varying magnetic field is produced by discharging a bank of capacitors through this solenoid. As the field varies, a signal is induced in the pickup coil which contains, in addition to a slowly varying component due to imperfect compensation, a component proportional to dM/dt where M is the magnetization of the sample. The slowly varying component is filtered out and the oscillatory part, the dHvA signal, which is usually of the order of millivolts, is amplified and observed on one trace of a dual-beam oscilloscope. Simultaneously the second trace of the oscilloscope shows the current passing through the pulse

Figure 2.1. Block diagram of dHvA equipment



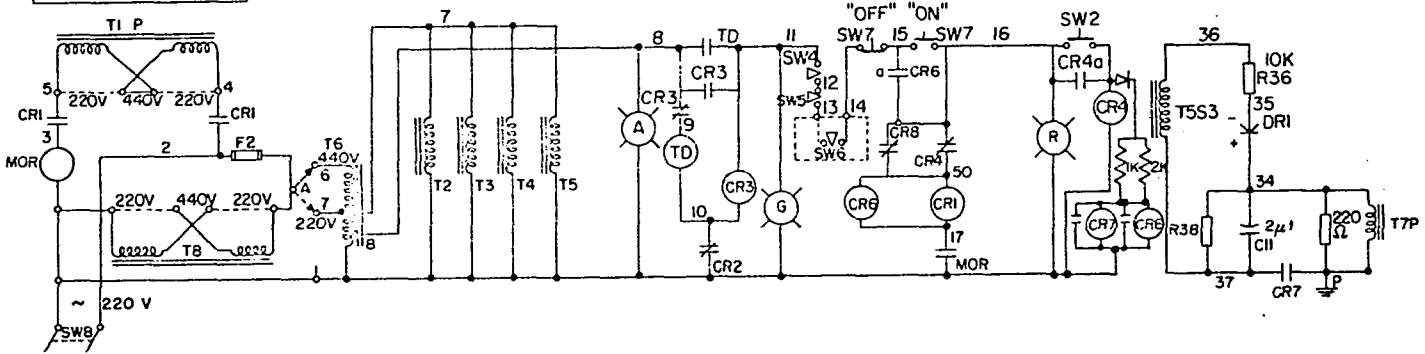
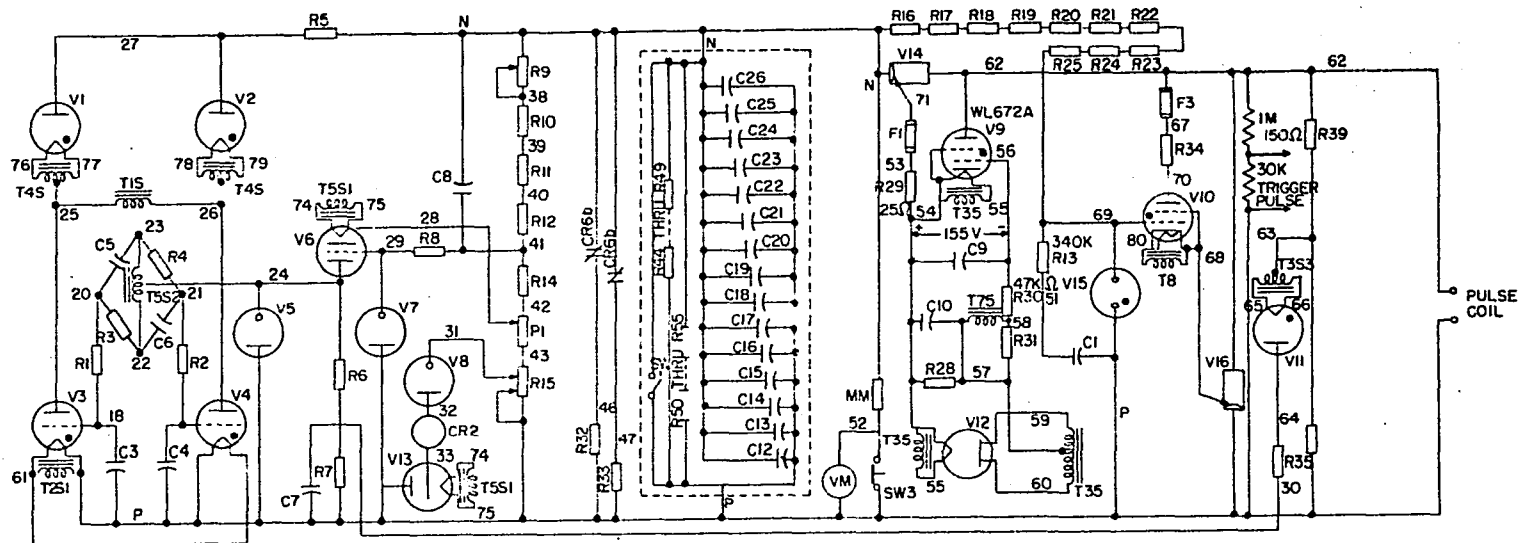
coil. The traces are photographed and periods and amplitudes are determined from the film.

2.2. Pulse System

The pulse-field system consisted of a large bank of capacitors, the unit for charging and discharging these capacitors, and the pulse coil.

Thirty G.E. oil-filled 120 μ F capacitors capable of being charged to 3000 volts were used in the present experiment. The equipment for charging and switching the capacitors was a Raytheon Model 8100 Impulse Magnetizer. This unit was capable of charging the capacitors to any voltage between 1000 and 3000 volts and then, by means of an ignitron switch, discharging the capacitors through the pulse coil. The ignitron was a type WL-5550 which would handle 15 millisecond pulses of over 1500 amperes maximum quite satisfactorily. However, since this apparatus had been constructed for commercial use in magnetizing or welding, modifications were necessary in order to use it in our experiment. We found that several relays, which were opening and closing unnecessarily during a pulse, produced large spikes on the trace showing the de Haas-van Alphen signal. It was possible to delay these effects until the pulse was over by making minor modifications in the circuit. Figure 2.2 shows the modified circuit diagram for the charging unit.

Figure 2.2. Circuit for charging and discharging capacitor bank
(modified Raytheon impulse magnetizer circuit)



The heart of the entire experiment is the pulse coil. The coil needs to be strong to withstand the large forces during a pulse and must be carefully compensated to produce a homogeneous magnetic field.

With these thoughts in mind, several pulse solenoids, similar to those described by Gold (1958a) and Priestley (1961) were constructed. The coils were wound with rectangular copper wire (0.030" x 0.045") with a "Lewmex" Grade M insulation about 0.002" thick.¹ Figure 2.3 shows a completed coil. This coil was 12 centimeters long and contained 12 layers of wire with about 100 turns per layer. The inside diameter was 1.6 centimeters and the outside diameter approximately 3.8 centimeters. The coil was wound on a split brass mandrel covered with a layer of paper which could be removed from the completed coil to allow more working space inside. An epoxy resin, Araldite D, was applied with a brush during the winding to bond the turns together and a sheet of thin graph paper was placed between the layers of wire for additional electrical insulation. After the winding was completed, the coil was placed under a heat lamp for about 24 hours in order to cure the Araldite. Then a sheet of Scotch-ply reinforced plastic²

¹This wire was obtained from London Electric Wire Company and Smith's Ltd., London, England.

²Manufactured by Minnesota Mining and Manufacturing Company.

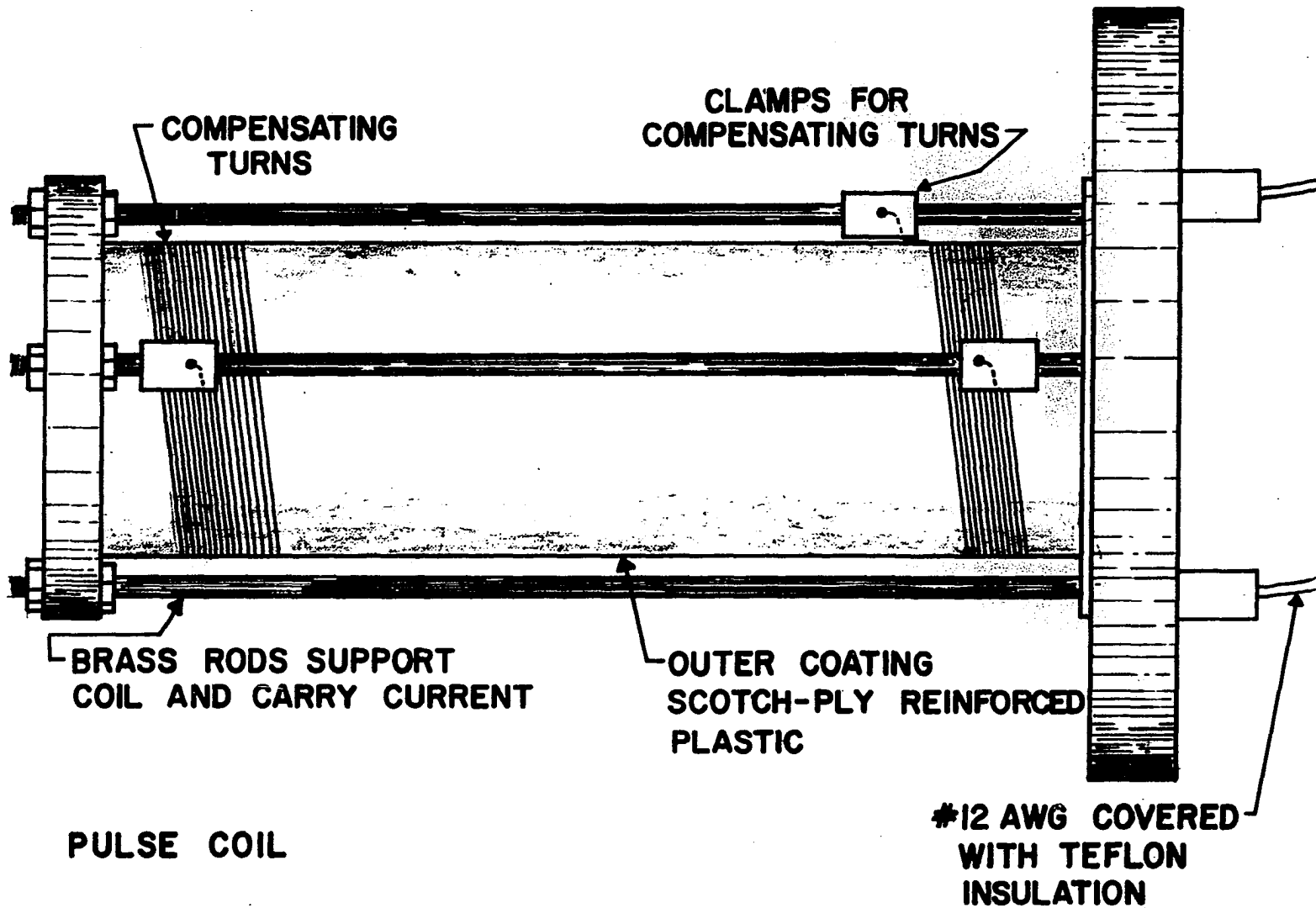


Figure 2.3. Schematic drawing of pulse coil
 (The obliquity of the compensating turns is exaggerated)

was wrapped around the coil, prestressed mylar,¹ was wrapped around this thermal setting Scotch-ply, and the coil heated at 135°C for about 5 hours. Heating caused the mylar to shrink so that the Scotch-ply made a strong outer coating for the coil.

Great care was taken in compensating the pulse coils in order to obtain the homogeneity required for observation of dHvA oscillations. (For periods as short as 2×10^{-9} Gauss⁻¹ the field variation over the length of the sample $\Delta H/H$ must be less than one part in 10^4 .)

Two slightly different types of coils were constructed for the dHvA effect measurements. In one case it was intended to let the oscillations from one crystal beat against those of a second crystal and study the beat periods as a function of relative orientation of the two crystals. For this purpose a solenoid was required with two homogeneous regions, $\Delta H/H < 10^{-4}$, each about 0.5 cm long and separated by a distance along the coil axis of about 1.5 cm. In order to obtain this variation two turns were omitted at the center of the final layer of windings. Figure 2.4a shows a profile of the field variation along the axis for this type of coil. Figure 2.4b shows a profile for the same coil after addition of compensating turns as described below. For the second type

¹Prestressed mylar was obtained from the Allis Chalmers Manufacturing Company.

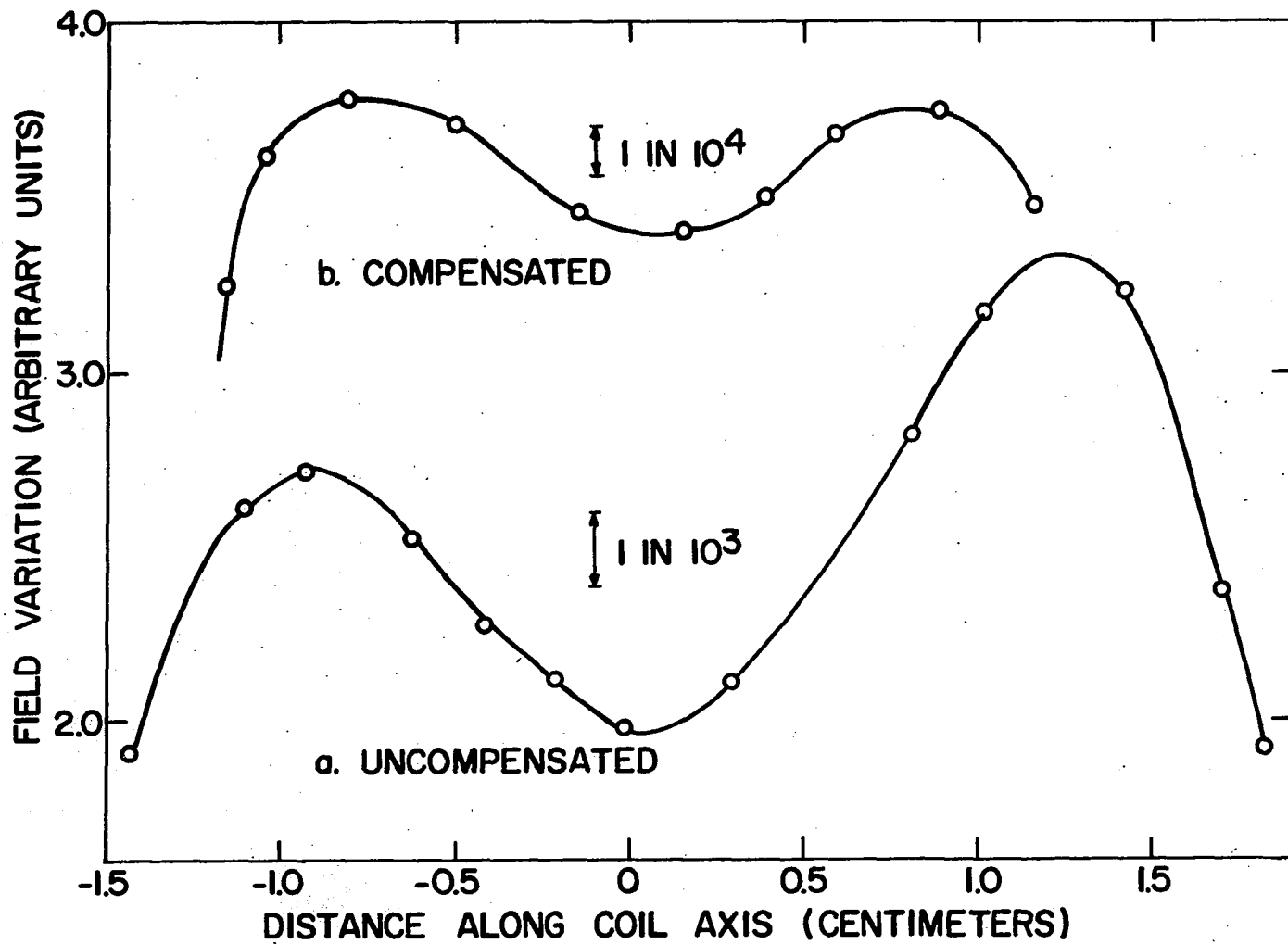


Figure 2.4. Field profiles for a pulse solenoid

of coil no turns were omitted as a region at the center of the coil approximately one centimeter long was required over which $\Delta H/H < 10^{-4}$.

The coils were compensated with the aid of two small nearly identical pickup coils of 100 turns each. Figure 2.5a shows the compensating circuit. A current of 33 c/s was used in the pulse solenoid since the period of our pulsed magnetic field corresponds approximately to this frequency. With the switch in one position, say I, the outputs from the two pickup coils added and a large reading was observed on the scope proportional to twice the magnetic field produced by the solenoid. With the switch in the other position, II, the voltages from the two pickup coils nearly canceled, the degree of cancellation depending upon the relative positions of the two coils. This cancellation allowed the use of considerable amplification to observe the small differences in voltage as one pickup coil was moved relative to the other held fixed as a reference. In this way curves such as those in Figure 2.4 could be made for different positions of the compensating turns.

The brass support rods, that clamped the end cheeks to the coil as shown in Figure 2.3, were also used as conductors. The compensating turns were attached to the support rods by clamps making the adjustment of the turns fairly simple. The number of compensating turns required on each side of the coil

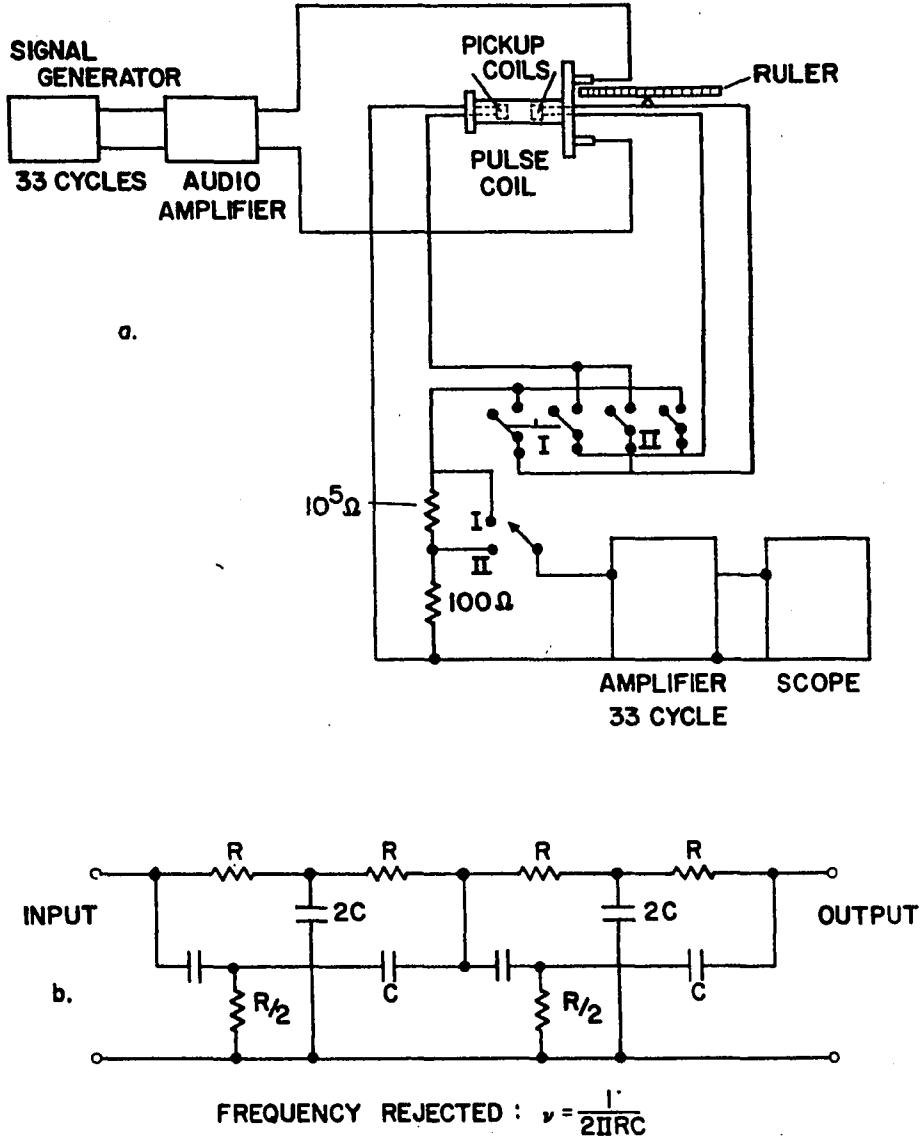


Figure 2.5. a. Pulse coil compensation circuit
b. Twin T filter circuit

was ordinarily less than 12. When satisfactory homogeneity was obtained, the compensating turns were soldered to the clamps and fastened to the coil with Araldite. Then the coil was ready for calibration.

The pulse coils were calibrated in several ways. One method used a mutual inductance bridge circuit comparing the inductance of the pulse coil with the known value for another coil with coil constant of 101.54 Gauss/amp.¹ This method probably gave the coil constant only to about 0.5% as it was difficult to obtain a sharp null. A second method used an InAs Hall effect probe which had been previously calibrated by nuclear magnetic resonance. This method had the disadvantage that the output of the Hall probe varied with temperature by about 0.1% per degree and the current through the solenoid caused an unknown temperature rise in the Hall probe. This temperature rise limited the currents used in the pulse coil to less than four amperes for this measurement. The most satisfactory method was the use of nuclear magnetic resonance with which the field could be measured over a range from 300 to 1100 Gauss. Figure 2.6 shows a schematic of the nuclear magnetic resonance calibration apparatus. The pulse coil was immersed in liquid nitrogen. A small glass dewar, especially constructed to fit inside the pulse coil, was filled with

¹This coil was obtained from Experimental Physics Group X.

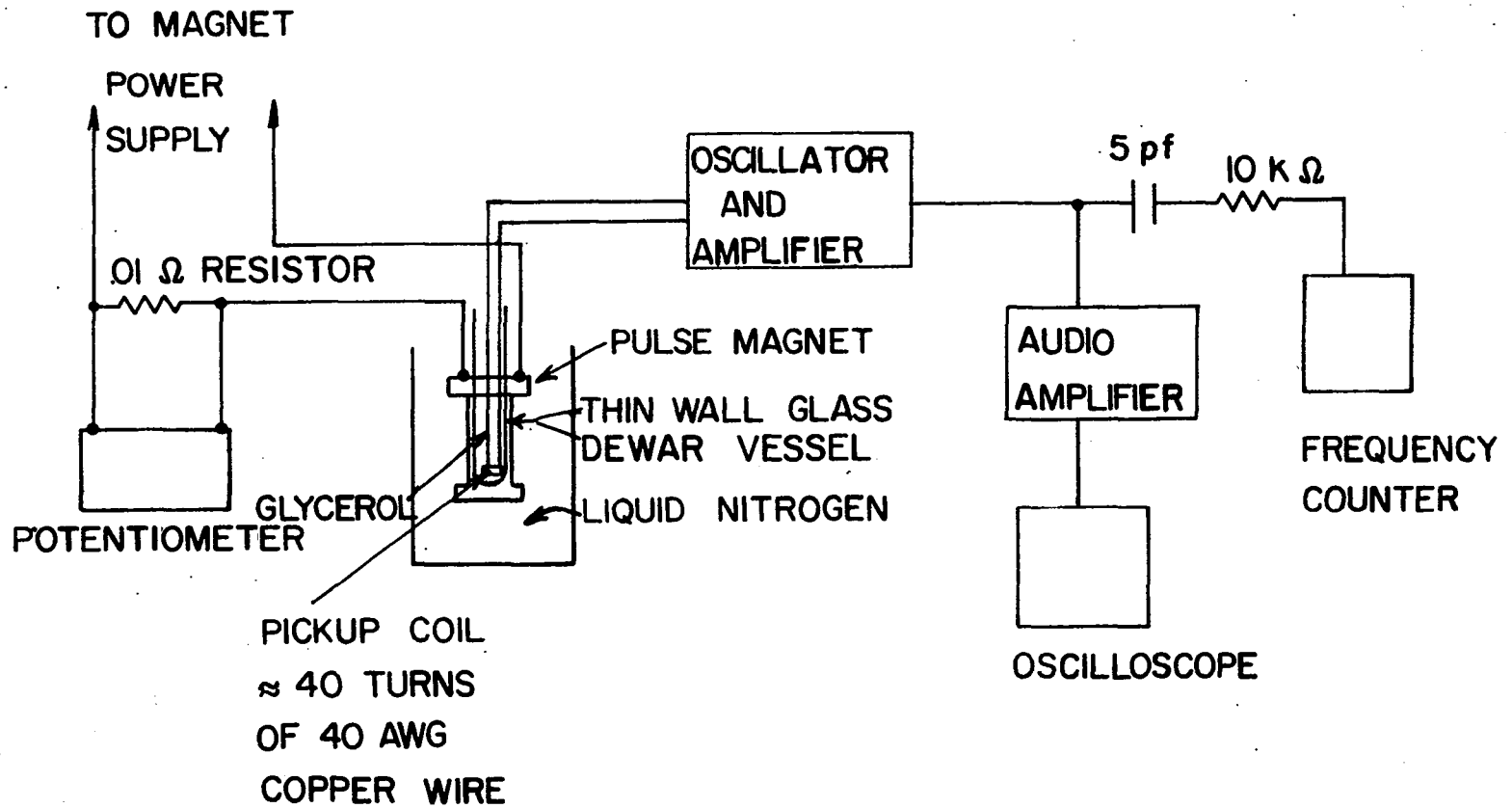


Figure 2.6. Nuclear magnetic resonance circuit for calibration of pulse coils

glycerin and the NMR pickup coil inserted in this dewar. The resonance frequencies were determined as a function of the current through the coil as measured with a potentiometer across a .01 ohm standard resistor. The coil constant was calculated from the standard formula for proton resonance, $f(\text{kc}) = 4.2577 H(\text{Oersteds})$. The current through the pulse coil was regulated by the power supply of a Harvey Wells magnet. With this method the dc coil constant could be determined very accurately.

The coil constants for three similar coils were approximately 114 Gauss/amp and the measured values agreed to about 1/2% with values calculated using the formula:

$$\frac{H}{I_0} \cong l \sum_{k=0}^m (n_k) \left\{ \frac{1}{(r_k^2 + l^2)^{1/2}} - \frac{r_k \Delta R}{2(r_k^2 + l^2)^{3/2}} \right\} \quad (2.1)$$

Here the summation is carried out over the layers of the coil. r_k is the radius of the kth layer, n_k is the number of turns per meter in the kth layer, ΔR is the thickness of the wire, and l is the length of the coil. Corrections were also made for the compensating turns.

The pulse coils used in this experiment had the following coil constants:

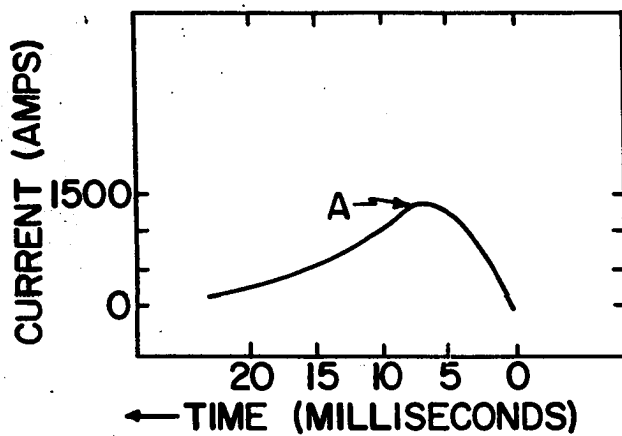
<u>Coil</u>	<u>Gauss/amp</u>	<u>Method of calibration</u>
B	114.4 \pm 0.5	Mutual Inductance Comparison
C	114.2 \pm 0.1	NMR
C	113.8 \pm 0.6	Hall Effect
D	114.0 \pm 0.6	Hall Effect

In liquid nitrogen the pulse coil has a resistance of about 0.25 ohms and an inductance of the order of 6 mh.

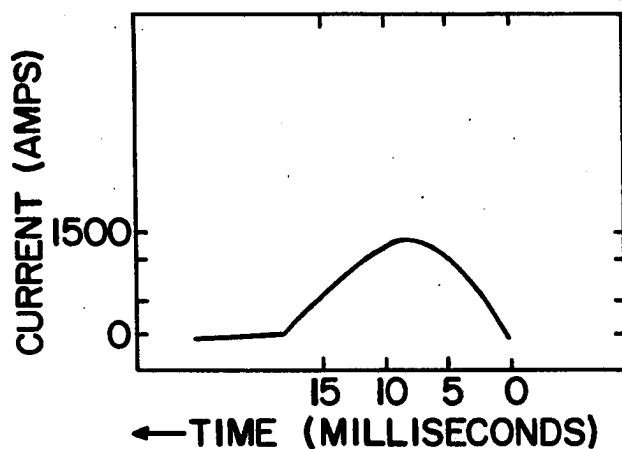
Figure 2.7 shows examples of the current through the coil during a pulse. Because the camera reverses the trace in the actual experiment, we have drawn these pictures in the same manner and time increases from right to left. The second ignitron, or crowbar, fires at A as shown in Figure 2.7a. If the crowbar is removed from the circuit, the trace is more symmetrical as shown in Figure 2.7b, and certain errors in period measurement tend to cancel. This cancellation will be discussed in more detail in Chapter 3.

The exponential decay after the second ignitron fires was used to estimate the temperature rise to be about 25°C during a pulse of 160 kG maximum field.

During a pulse the magnetic field was determined by displaying on one beam of the dual beam oscilloscope the voltage drop across a .01 ohm standard resistor in series with the pulse coil. Calibration lines were also put on the scope to eliminate distortion and variation of sensitivity. Figures 2.8 and 2.9 show a diagram of the calibration circuit which pro-



a.



b

Figure 2.7. Examples of current through the pulse solenoid
a. Second ignitron (crowbar) used
b. Second ignitron removed

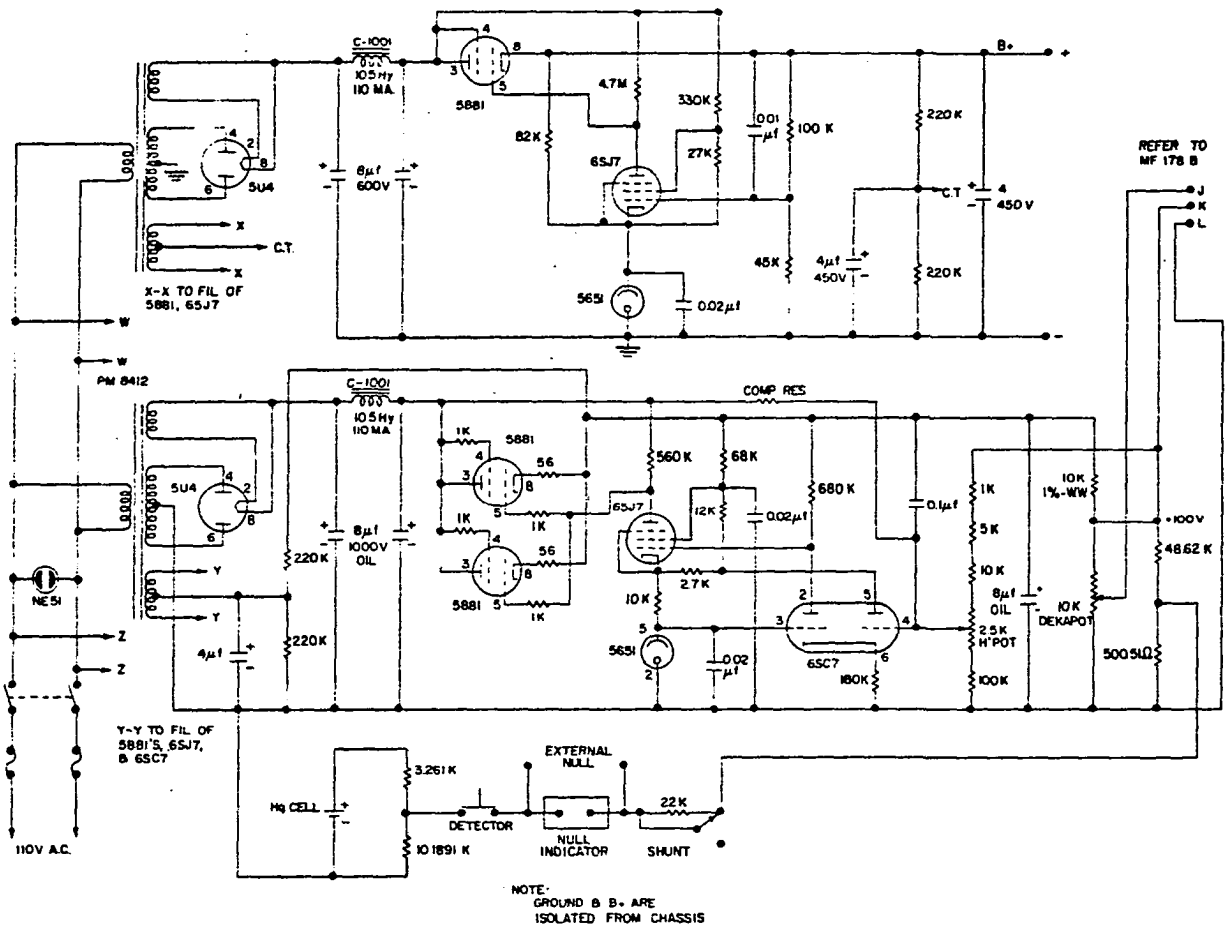


Figure 2.8. Diagram of calibration and bucking circuit: Part I

vided a voltage accurate to better than 0.1%. A switch on the calibration unit allowed use of this accurate voltage to buck out part of the voltage drop across the .01 ohm resistor. The remainder could then be amplified and, in this way, the accuracy of the measurement was greatly increased. The calibration lines were put on the picture after the pulse, either manually or automatically, by means of a stepping relay. Figure 2.9 also shows the trigger circuit for starting the calibration lines. During the actual pulse the scope was triggered from a voltage divider network across the pulse coil as shown in Figure 2.1.

2.3. de Haas-van Alphen Signal

The signal from a pickup coil around the needle-shaped sample was amplified, filtered, and displayed on the second trace of the oscilloscope. Filtering removed most of the steady component of the magnetization leaving only the oscillatory part, and noise, to appear on the oscilloscope.

Originally a Tektronix 555 oscilloscope was used for this experiment, but this was later replaced by a Tektronix 502 which seems to have less drift and distortion. Also, the Tektronix 502 has only a single set of horizontal deflection plates which implies that the two traces should sweep together.

The two traces, the dHvA oscillatory signal and the field trace, were photographed with a Dumont oscillograph camera

(type 302) using Polaroid-Land film, type 44, with a speed rating of 400.

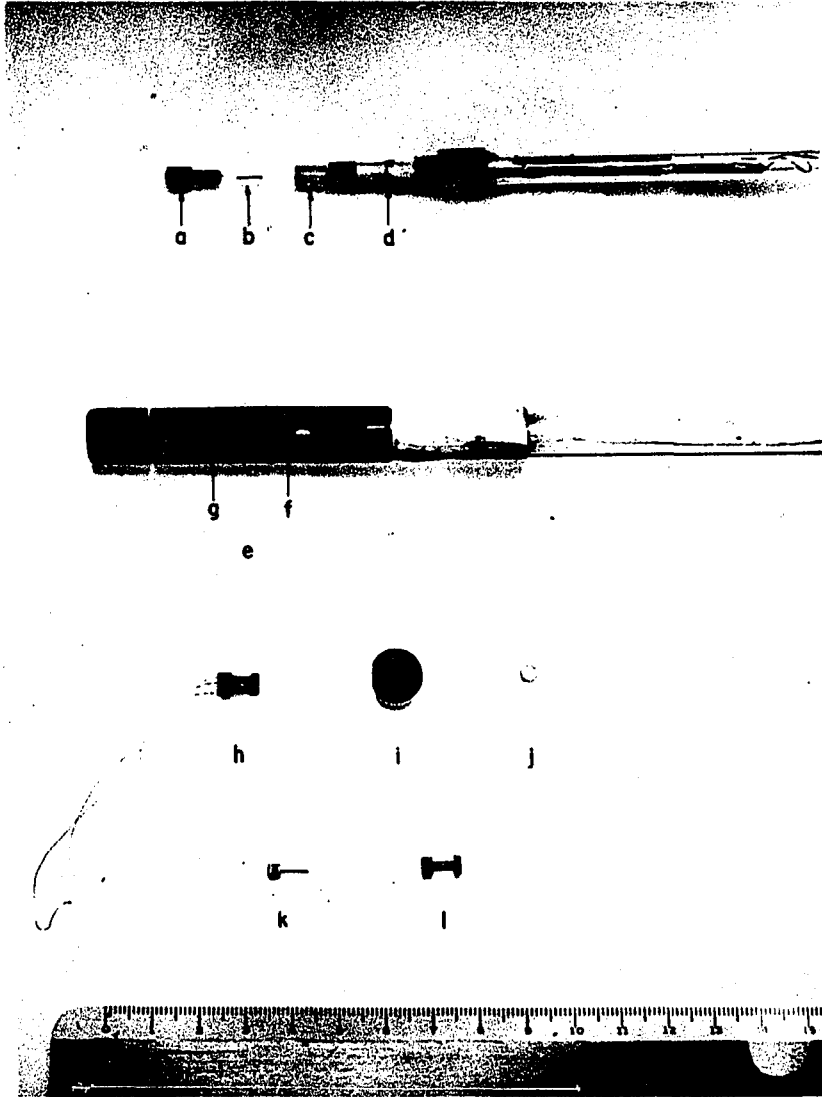
One of the most important tasks was the construction of good pickup coils. In order to eliminate most of the induced signal in the pickup coil not caused by the sample a second coil is wound around the first in series-opposition. It is arranged that the area-turns of the two coils balance; then the opposing coil will have fewer turns than the primary. In practice, an excess of 'opposing' turns is wound and then slowly removed until the minimum induced signal is observed when the pickup coil is placed in a uniform alternating current. Both rotating and stationary pickup coils were constructed. Figure 2.10 shows the two types of coils and the sample holders that fit in the coils. The stationary coils, used to study oscillations for the magnetic field along the specimen axis were wound with 52, 46, and 44 AWG copper wire on red fiber forms with internal hole of diameter 0.035". When 46 AWG wire was used, approximately 1500 turns were wound in one direction and then the winding direction was reversed and about 1000 compensating turns were wound on top of the original 1500; with care this could be done with very little scrambling.¹

The rotating coils and sample holders were made from

¹The coils were wound with a coil winder manufactured by the Willy Aumann Co.

Figure 2.10. Sample holders, pickup coils, and rotating mechanism
(A centimeter scale is shown for comparison)

- a. Stationary sample holder
- b. Crystal inside glass capillary
- c. Stationary sample holder inserted in pickup coil
- d. Pickup coil
- e. Nylatron forks
- f. Wheel containing rotating pickup coil
- g. Position of stationary pickup coil used in beat measurements
- h. Rotating pickup coil
- i. Wheel
- j. Teflon bushing
- k. Sample mounted in rotating sample holder with mirror for orientation
- l. Form for rotating pickup coil



nylatron and were very similar to those used by Gold (1958b). The rotating coils usually had a total of about 1600 turns of No. 46 AWG wire and were designed to fit into the small nylatron wheel shown in Figure 2.10.

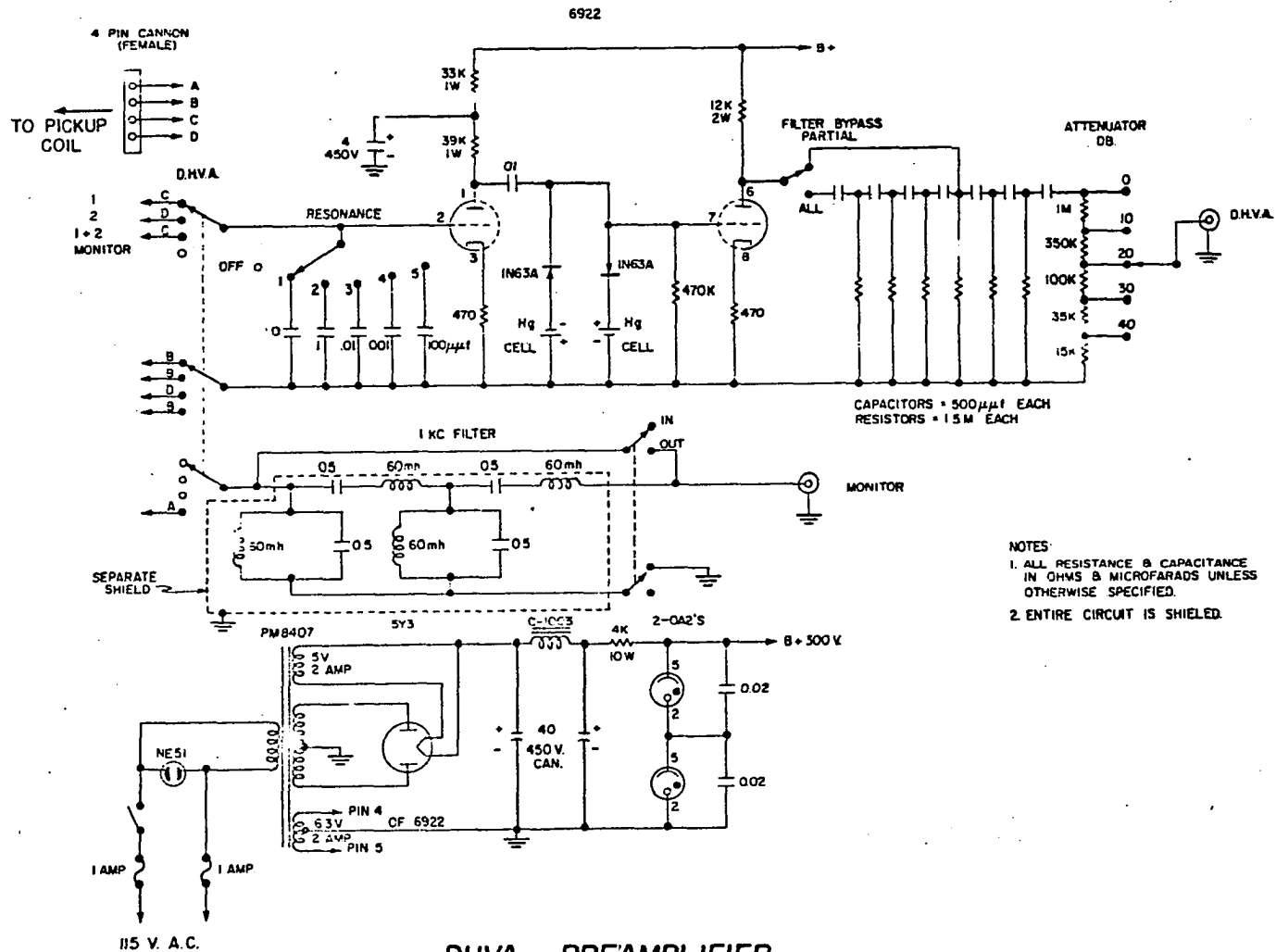
In order to find and separate the de Haas-van Alphen periods, capacitors were added in parallel with the pickup coil to make a resonant circuit. Then the largest amplitude for a particular dHvA period, P, would occur for a magnetic field such that

$$\frac{1}{PH^2} \frac{dH}{dt} = \nu, \quad (2.2)$$

where ν is the resonant frequency of the pickup coil plus capacitors. By changing the value of capacitance, we could vary the resonant frequencies from about 5 kc to 160 kc for the pickup coils normally used. The maximum frequency was limited by the capacitance in the line and pickup coil. A special coil wound with approximately 10,000 turns of 52 AWG copper wire had a maximum resonant frequency of only 32 kc/sec.

Figure 2.11 shows the capacitors, pre-amplifier, and the high pass filter which was used to cut out frequencies below about 1000 cycles. The amplifier had a maximum gain of approximately 100 and was normally used at this setting.

Twin T rejection filters (General Radio 1961) were sometimes used following the amplifier to filter out large ampli-



DHVA PREAMPLIFIER

Figure 2.11. Preamplifier and filter for dHvA signal

tude oscillations of different period (Figure 2.5b). In this way several new dHvA periods were observed.

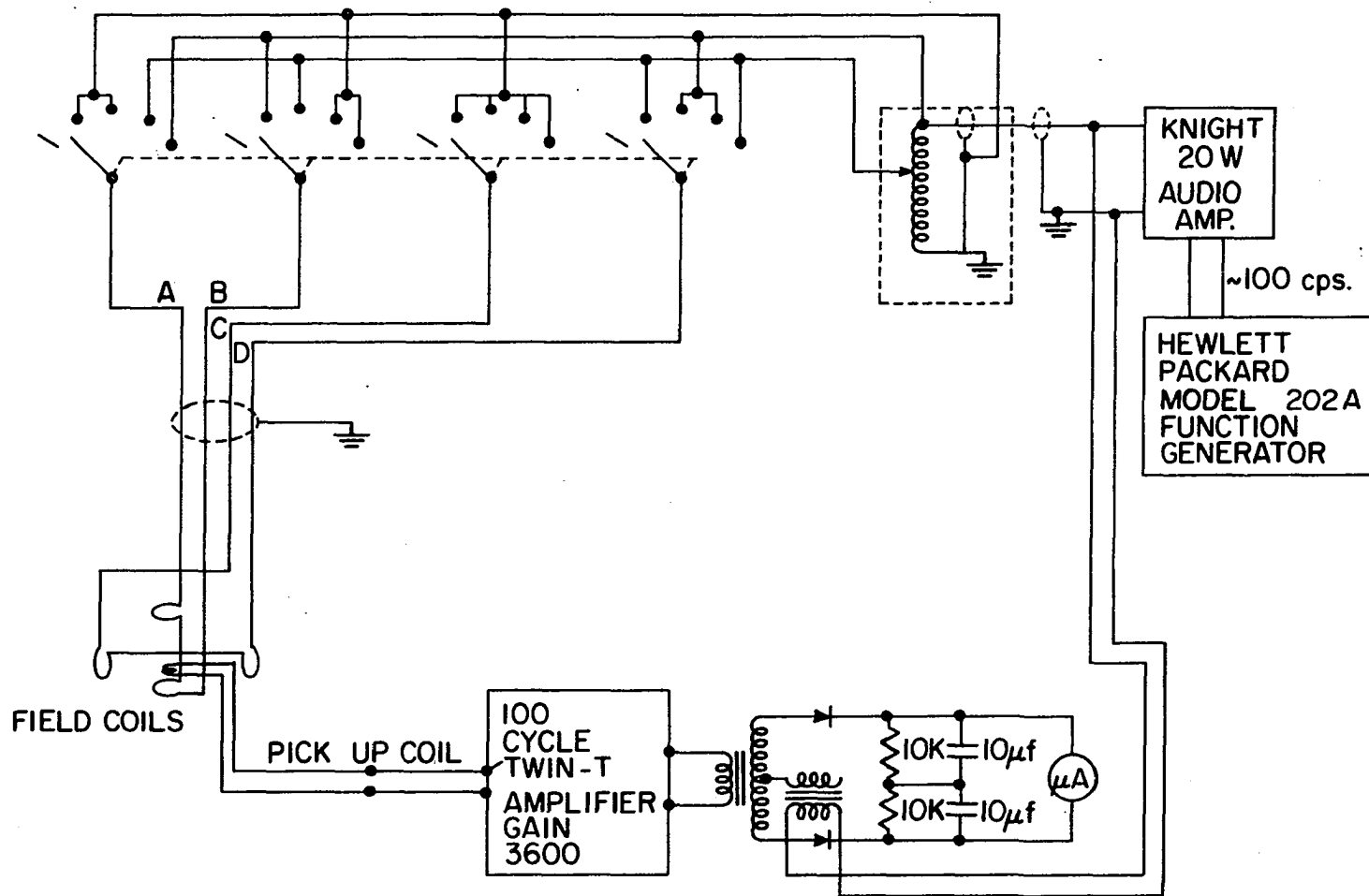
2.4. Rotating System

The system for rotating the sample was similar to that used by Gold (1958b) and will not be described in any detail. Some parts of the rotating mechanism are shown in Figure 2.10. A nylatron wheel containing the sample and pickup coil rotated in nylatron forks. Teflon bushings were used to reduce friction so that the wheel turned quite easily at low temperatures. Built into the forks was a second, stationary, pickup coil for use in comparing two samples by studying beat periods. The outside diameter of the rotating mechanism was 11 mm to fit inside the cryostat which had a 12.2 mm inside diameter. This rotating mechanism was attached to a glass tube about 12" long which extended outside the high field region and was then held by a stainless steel tube supporting a winch case at its top. The total length of this suspension was about 42".

A length of braided nylon fishing line, ten pound test, was wrapped twice about the winch, glued, and then extended in a loop about a groove in the rotating wheel holding the pickup coil, where it was glued again. A spring in the winch case kept tension on this string at all times. It was then possible to turn the handle of the winch at the top of the sample holder and rotate the wheel at the bottom. This device

worked well even when immersed in liquid helium although some backlash was present which made it necessary to have a means for checking the orientation of the sample axis with respect to the solenoid axis.

Figure 2.12 shows a block diagram of the sample orientation circuit. This orientation was determined by means of two pairs of identical Helmholtz coils mounted just outside the liquid nitrogen dewar. One pair was coaxial with the pulse solenoid while the axis of the other pair was at right angles to the solenoid axis and in the plane of rotation of the pickup coil. The Helmholtz coils were energized with 100 c/s current using a variable transformer, "Dekatron" to accurately adjust the current ratio in the two sets of coils without changing the relative phases. (Eddy current effects were negligible at 100 c/s.) The voltage induced in the pickup coil by the Helmholtz coils was amplified and filtered and the output read on an oscilloscope, vacuum tube voltmeter or a center-zero dc microammeter. The current ratio in the two sets of Helmholtz coils was adjusted by means of the "Dekatron" for a minimum. The ratio was equal to the tangent of the angle the pickup coil axis made with the axis of the pulse coil.



CIRCUIT FOR DETERMINATION OF SAMPLE ORIENTATION

Figure 2.12. Block diagram of sample orientation circuit

2.5. Samples and Preparation

The lead used in this experiment was zone-refined lead obtained from Dr. G. F. Bolling of Westinghouse Research Labs and the polycrystalline extruded wire was found to have a resistivity ratio $\rho_{300^\circ}/\rho_{4.2^\circ}$ of about 4000. This lead was extruded into long wires about 0.4 mm in diameter and single crystals were grown on a "Kapitza" furnace using a lead seed crystal to obtain any desired orientation. This procedure is also described in detail by Gold (1958a). The long wire was cut with a razor blade into 5 mm to 6 mm lengths which were then etched for about half an hour in concentrated HCl.

The samples were carefully mounted in glass capillaries (i.d. \approx .022", o.d. \approx .029") by glueing one end with Duco cement. The other end was left open to allow liquid helium access. The glass capillaries were then glued into small nylatron or nylon holders which could be inserted into the pickup coil forms. The samples mounted in the sample holders for both the rotating and stationary coils are shown in Figure 2.10.

The samples were then oriented using standard back reflection x-ray techniques with a single crystal oscillation goniometer.¹ A tiny mirror was attached to each rotating sample holder as a reference for orientation. A small light

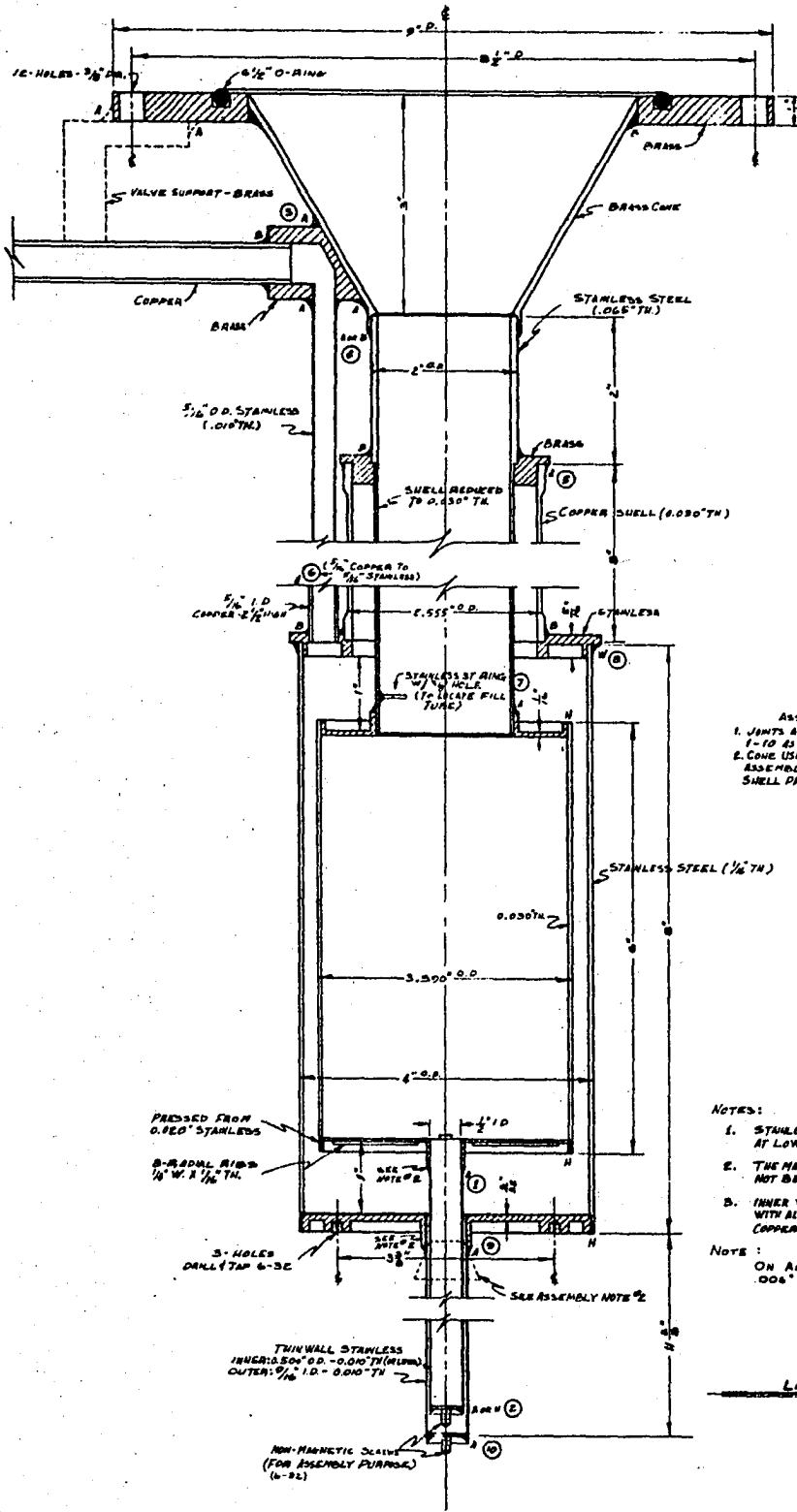
¹Unicam Single Crystal Oscillation Goniometer S.25.

could be fastened to the x-ray collimator and the beam passing through the collimator was reflected by the mirror and observed in the telescope attached to the rotation camera. Since the telescope was at right angles to the light or x-ray beam, the reflection was observed with the mirror normal at an angle of 45° with respect to the beam direction. The axis along the length of the sample and the mirror normal were the reference directions by which the crystal axes could be located. After the determination of orientation the sample holder was ready to be mounted in the pickup coil. The sample holder, coated with N type Apiezon grease, was pushed into the hole in the pickup coil form. A screwdriver slot in the end of the sample holder allowed the sample to be rotated about its axis until the desired crystallographic plane was parallel to the plane of rotation of the wheel. At low temperatures the Apiezon grease hardened and the sample holder was held firmly in the pickup coil. The orientation of the sample axis could be determined to about 1° while the plane of rotation could be located to within about 3° .

2.6. Cryostats and Pumping System

Several liquid helium cryostats were used; the first was made of glass and later ones were made of stainless steel. Figure 2.13 is a schematic diagram of a stainless steel cryostat. In Figure 2.14a this cryostat is shown surrounded by

Figure 2.13. Schematic diagram of stainless steel
helium cryostat



ASSEMBLY
 1. JOINTS A, B, H, W, IN SEQUENCE
 1-TO 45 SHOWN.
 2. CONE USED TO CENTER INNER
 ASSEMBLY IN RESPECT TO OUTER
 SHELL PRIOR TO SOLDERING JOINT #B

LEGEND (WELDS)
 A - SOFT SOLDER
 B - SILVER SOLDER
 H - HELIARC
 W - WOODS METAL
 (PRE-TIN W/SOFT SOLDER)

NOTES:
 1. STAINLESS STEEL MUST BE NON-MAGNETIC
 AT LOW TEMPS. USE ONLY 321 GRADE.
 2. THE MAXIMUM I.D. OF THESE JOINTS MUST
 NOT BE LESS THAN I.D.'S OF THINWALL TUBES.
 3. INNER WALL OF VACUUM INTERSPACE IS WRAPPED
 WITH ALUMINUM FOIL (HELD WITH TWISTED
 COPPER WIRE) NO FOIL IN TREAT.

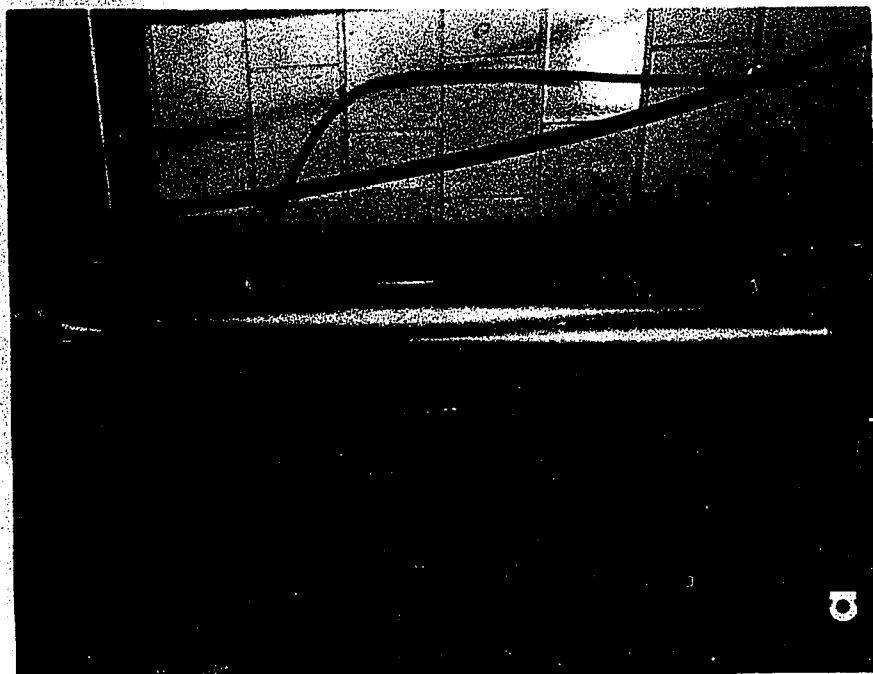
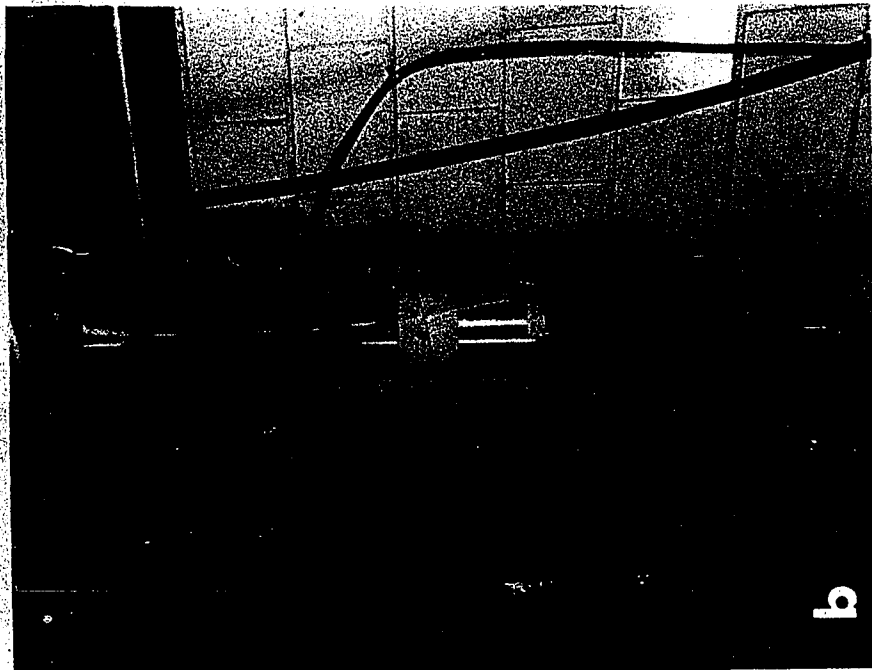
NOTE:
 ON ALL SOFT SOLDER JOINTS ALLOW
 .006"-.010" FOR CLEARANCE

LIQUID HELIUM DEWAR

SECTION

Figure 2.14a. Helium cryostat

Figure 2.14b. Liquid nitrogen
container



the outer liquid nitrogen container. In Figure 2.14b the nitrogen container has been removed and we see the liquid helium cryostat with the pulse coil, which just fits over the narrow tip of the cryostat.

This cryostat was constructed so that it could be assembled and taken apart easily. Hence Wood's metal was used in making one of the solder joints. No spacers were necessary in the vacuum innerspace. The use of stainless steel did not affect the magnetic field homogeneity, and estimates of the magnetic field produced by the eddy currents gave a negligible correction to the field calibration. However, due to eddy current heating and possible magnetic transitions, from 1 to 5 cubic centimeters of liquid helium were lost on each pulse. This helium loss was observed as a rise of about 1 centimeter in the oil manometer. It was necessary to use very thin wall stainless steel tubing for the tip to reduce this loss.

In order to reach temperatures below 4.2°K, it was necessary to pump on the liquid helium. A Heraus Roots type vacuum pump, CVC Model VPRG-1000A, backed by a Kinney forepump, CVC Model E-225, was used to obtain temperatures slightly below 1°K. The Heraus pump had no oil in the pumping chamber but used the rotation of two interlocking dumbbell-shaped pieces to sweep out the helium gas. This pump had a pumping speed of approximately 300 liters/sec at 10^{-2} mm of Hg while the forepump had a speed of about 130 cubic feet/minute. Temperatures

were determined from the vapor pressure of helium as read on ordinary mercury and oil manometers.

3. OSCILLATION PERIODS AND AMPLITUDES: THEIR MEASUREMENT AND THEIR ERRORS

3.1. Examination of Photographs and Period Measurements

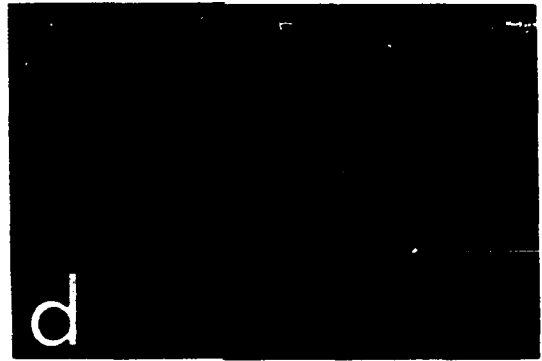
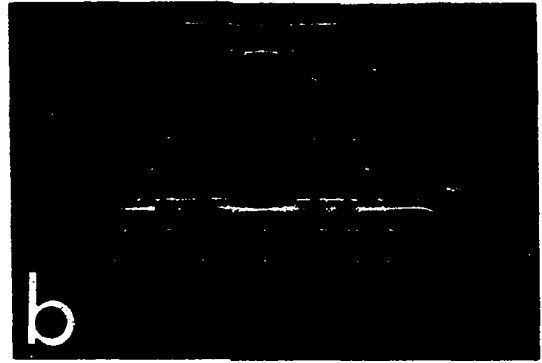
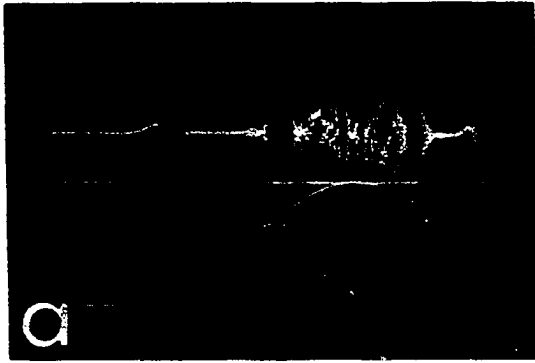
The results from the dHvA experiment appear directly on polaroid film and some information is obtained at once by examination of the envelope of the oscillations. Figure 3.1a shows an overall pulse in which time is increasing from right to left. The magnetic field trace (lower trace) is nearly a half sine wave and the field calibration is represented by the horizontal lines. The upper trace shows the dHvA oscillations and we note that their amplitude goes to zero at the field maximum, since no oscillations take place when the magnetic field is constant. The resonant frequency technique ($\nu = 21 \text{ k c/s}$) was used to separate the different sets of oscillations (Section 2.3). According to Equation 2.2 the maxima in the envelope occur at $\dot{H}/H^2 = P\nu$ and this equation can be used for a rough estimate of P with values of \dot{H}/H^2 measured at the oscillation (blip) maximum.

Figure 3.1a is an example of the intricate patterns that can occur in this experiment. On either side of the field maximum we find narrow spikes corresponding to the α oscillations¹ while the γ oscillations of longer period (and larger

¹We use the notation of Gold (1958b) labeling these oscillations.

Figure 3.1. Examples of dHvA oscillations in lead
(all vertical graticule lines at one centimeter intervals)

- a. Overall picture for H // [110].
Calibration lines 0, 114, and 171 kG.
2.0 ms/cm sweep
- b. Overall picture for H // [100] showing γ and β oscillations well separated. Baseline = 39.9 kG and calibration lines at intervals of 5.71 kG.
1.0 ms/cm sweep
- c. α oscillations for H // [110] showing modulation by the γ oscillations. Baseline = 130.1 kG and calibration lines at intervals of 1.142 kG.
0.1 ms/cm sweep
- d. α oscillations for H // [111] showing modulation by the γ oscillations. Twin T filter used to attenuate γ oscillations. Baseline = 116.4 kG and calibration lines at intervals of 1.142 kG.
0.1 ms/cm sweep
- e. γ oscillations showing beats for H 21° from [001] in a (.99, .14, 0) plane. Baseline = 55.96 kG and calibration lines at intervals of 1.142 kG.
0.1 ms/cm sweep
- f. δ_1 oscillations for H // [111].
Baseline = 113.1 kG and calibration lines at intervals of 1.142 kG.
0.1 ms/cm sweep



amplitude) resonate at lower fields. In between is a complicated mixture where an additional period was discovered upon more detailed study (Chapter 4).

Figure 3.1b shows a simpler overall picture in which the resonance technique was used quite successfully to separate the γ and β oscillations.

In order to obtain accurate period values as well as to study the more complicated details of the oscillations, it was necessary to expand the time scale and observe only a small section of the pulse. (Examples are shown in Figures 3.1 and 3.2.) This expansion was done by means of the various magnifications and sweep speeds available on the oscilloscope. The oscillations were then spread out and could be counted easily. Their period was determined from the number of cycles n between two values of field, H_1 and H_2 , and the relation

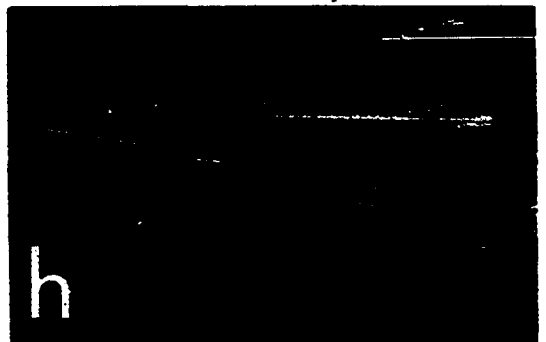
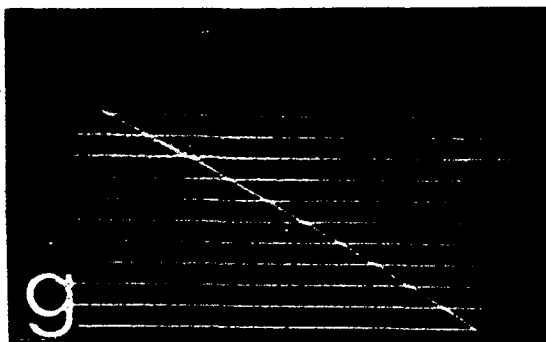
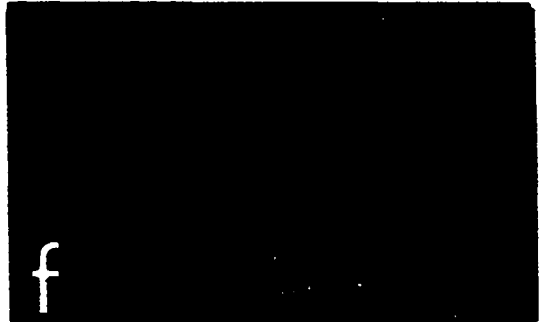
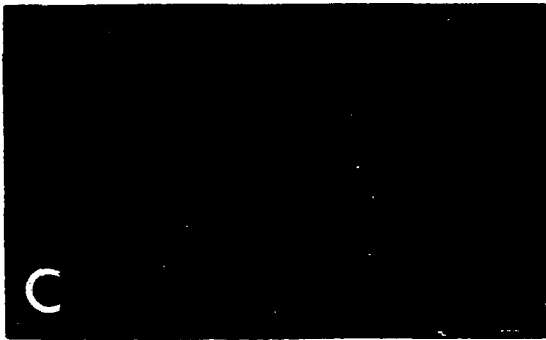
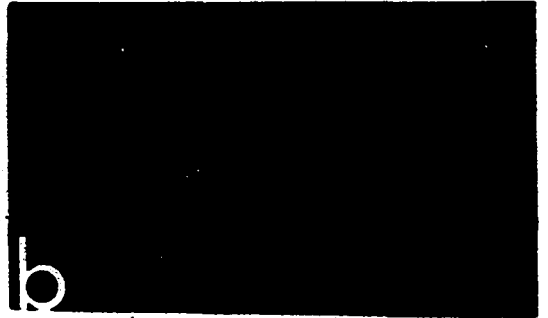
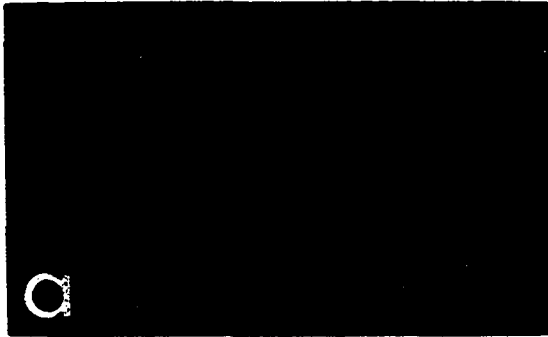
$$P = \frac{(V_1 - V_2)(0.01)}{n G V_1 V_2} . \quad (3.1)$$

V_1 and V_2 are the voltages corresponding to H_1 and H_2 , and G is the coil constant in Gauss/amp (Section 2.2). The current in the pulse coil was determined from the voltage drop across a 0.01 ohm resistor.

The accuracy of the field measurements was increased by applying a known voltage to buck out part of the field trace (Section 2.2), so that the change observed on the oscilloscope

Figure 3.2. Examples of dHVA oscillations in lead

- a. μ oscillations for $H // [110]$. Twin T filter used to attenuate β oscillations. Baseline = 164.4 kG and calibration lines at intervals of 1.142 kG. 0.05 ms/cm sweep
- b. Field pulse under same conditions as (a) to show reproducibility of oscillations
- c. β oscillations for $H // [110]$. No twin T filter was used and the μ oscillations are barely observable. Baseline = 148.5 kG and calibration lines at intervals of 11.42 kG. 0.1 ms/cm sweep
- d. γ oscillations for $H // [111]$. Baseline = 5.71 kG and calibration lines at intervals of 11.42 kG. 0.1 ms/cm sweep
- e. α oscillations for $H // [110]$. Twin T filter used. Baseline = 124 kG and calibration lines at intervals of 1.14 kG. 0.05 ms/cm sweep
- f. Second harmonic of β oscillations for $H // [100]$. Twin T filter used. Baseline = 137 kG and calibration lines at intervals of 1.14 kG. 0.05 ms/cm sweep
- g. γ oscillations for $H // [110]$. Baseline = 45.7 kG and calibration lines at intervals of 11.42 kG. 0.1 ms/cm sweep
- h. β oscillations for $H // [100]$. Baseline = 94.6 kG and calibration lines at 11.4 kG. 0.2 ms/cm sweep



represented only a small portion of the total field. By means of the scale on the traveling microscope it was possible to interpolate between field calibration lines.

Normally at least two measurements were made on each picture, one counting maxima and the other minima. Usually at least 30 or 40 cycles could be counted, but sometimes there were as few as ten to fifteen cycles.

In some cases strong oscillations were apparently masking additional sets of oscillations. For example, in Figure 3.2c we see, in addition to the strong β oscillations, the possibility of some low amplitude oscillations of shorter period. In Figure 3.2a and 3.2b twin T rejection filtering has attenuated the β oscillations and the shorter period is plainly visible.

Often when the amplitudes were small, and especially when filtering was required, it was difficult to separate periods or to decide if the oscillations were genuine. Normally, pictures were repeated several times (3.2b is a repeat of 3.2a) and this repetition usually allowed real oscillations to be separated from noise. Also, the fact that the oscillations disappeared at higher temperatures indicated that they were not merely noise. A third and more decisive check was to plot values of $1/H$ at the oscillation maxima or minima versus integers and this plot would result in a straight line for true dHvA oscillations, the period being given by the slope of the line. Figure 3.3 shows such a plot for the

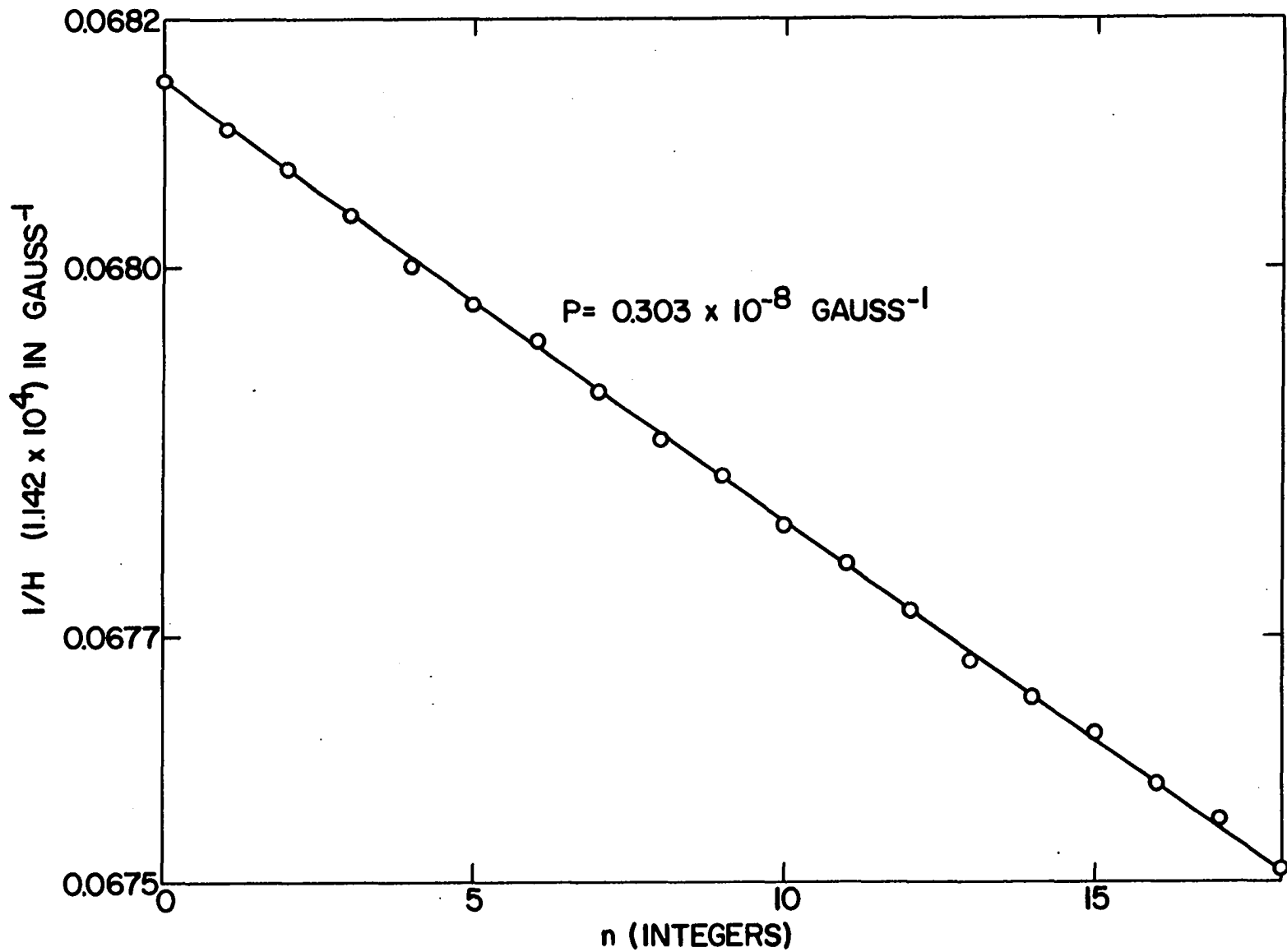


Figure 3.3. Plot of $1/H$ at oscillation maxima versus integers ($H \parallel [110]$)

oscillations of Figure 3.2a. Sometimes, two distinct slopes were observed which indicated two separate periods, as shown in Figure 3.4. This plotting technique proved very useful in the separation and accurate determination of periods.

In more complicated dHVA patterns, two or more periods often occurred together in beating patterns. Figure 3.1e shows an expanded picture of simple beats due to two periods which differ by about 8%. Gold (1958a) has given a fairly complete discussion of the determination of periods when simple beats occur and his results will be summarized here.

If two periods with the same amplitude are beating, the waists will be zero and measurement over a large number of cycles (i.e. over several beats) gives the average period. If the waists are not zero, similar measurement gives the period of the dominant term P_d (except in a few special cases unlikely in this experiment (Manley 1945)) while the period of the subordinate term P_s is obtained from the relation

$$\Delta P = P_d - P_s = \pm \frac{P_d}{N \pm 1} . \quad (3.2)$$

N is the number of oscillations per beat. The plus or minus sign depends upon the effective period at the waists P_{\min} and at the maxima P_{\max} . If $P_{\min} > P_{\max}$, then $P_d > P_s$ and the plus sign should be used while for $P_{\max} > P_{\min}$ the minus sign is taken. For more than 15-20 cycles per beat it is difficult to

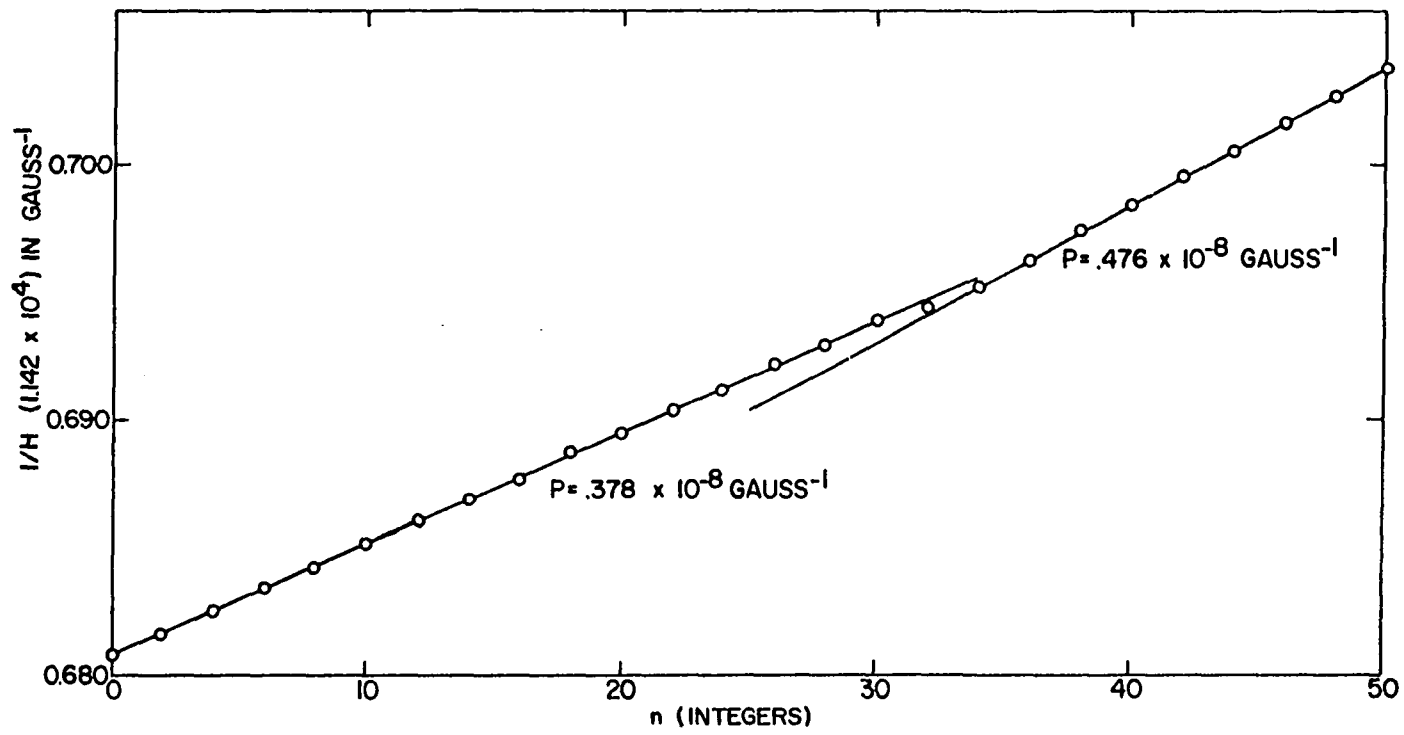


Figure 3.4. Plot of $1/H$ at oscillation maxima versus integers
 ($H // [100]$)

detect any difference between P_{\max} and P_{\min} and this criterion can not be applied.

The interpretation of beats is not always straightforward as in Figure 3.1e. Some of the remaining photographs in Figures 3.1 and 3.2 point out possible effects that must be considered.

Figures 3.2d and 3.2g show expanded pictures of the γ oscillations where the resonance technique was used. We see a sharp drop and apparent beats just after the resonance maximum occurs. These beats appearing only after the maximum are probably due to the 'gliding tone effect' which is the response of a resonant system to a signal of slowly increasing or decreasing frequency. This effect has been studied by Barber and Ursell (1948) and Shoenberg (ca. 1962). Physically, if the pickup coil has rather high Q and is driven with a slowly varying frequency ($\nu(t) = \dot{H}/PH^2$ for dHvA oscillations with period P), the amplitude of the oscillations will increase smoothly to a maximum near the resonant frequency. After the resonant frequency has been passed, the coil will continue to ring at its resonant frequency, and this resonant frequency beats with the time-varying dHvA frequency.

The equivalent circuit for our pickup coil and capacitor system is of the form:



This circuit satisfies the differential equation:

$$L \frac{d^2 q}{dt^2} + R \frac{dq}{dt} + \frac{q}{C} = F \quad (3.3)$$

where

$$F = F_0 \sin\left(\frac{2\pi}{PH} t + \psi\right) \quad (3.4)$$

$$= F_0 \sin\left\{ \frac{2\pi}{PH_0} \left[1 - \frac{\dot{H}_0 t}{H_0} - \frac{t^2}{2} \left(\frac{\ddot{H}_0}{H_0} - \frac{2\dot{H}_0^2}{H_0^2} \right) \right] + \psi \right\}$$

and H_0 is the field magnitude at $t = 0$. Barber and Ursell (1948) give the solutions of Equation 3.3 in terms of a parameter

$$k = \frac{4L^2 \omega^2}{R^2} \left(\frac{b}{\omega} \right)$$

where $\omega = 1/LC$ and

$$b = -\left(\frac{\ddot{H}_0}{H_0} - \frac{2\dot{H}_0^2}{H_0^2} \right)$$

for our experiment. A large value of k implies little damping. For representative values for our system ($R \approx 5$ ohms, $L \approx 10^{-3}$ h, $\omega \approx 2 \times 10^5$ sec $^{-1}$, and $b \approx 100$ sec $^{-1}$) $k \approx 0.4$ and $\sqrt{b\omega/2} \approx 3 \times 10^3$.

Figure 3.5 shows the envelope of this transient resonance for several values of k and we see that the results for $k = 0.5$ are similar to Figures 3.2d and 3.2g. Figure 3.2h

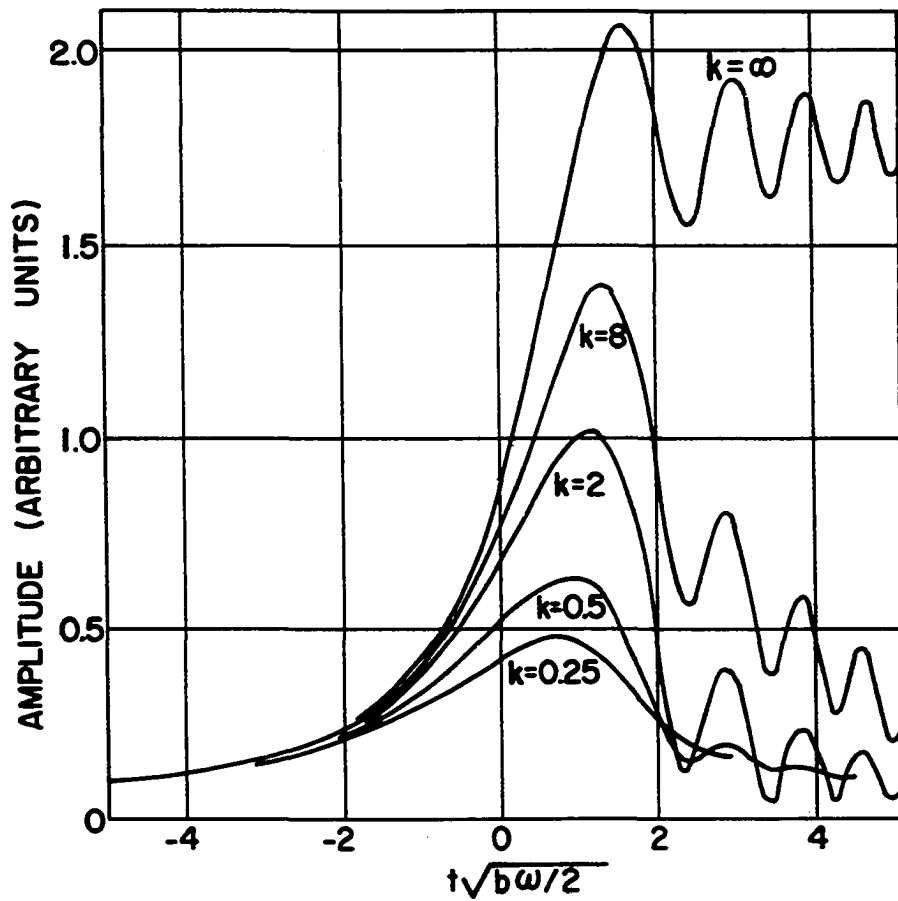


Figure 3.5. Envelope of transient resonance, gliding tone effect (after Barber and Ursell 1948)

shows the β oscillations in which an unusually sharp cutoff is observed after the resonance buildup. This cutoff is probably also related to the 'gliding tone effect', but the exact shape has not been explained.

When the resonance technique is used, it is important to choose the region of measurement carefully to avoid small errors in the period values. For $t\sqrt{b\omega}/2$ less than 0 or greater than 4, the measured frequency is the dHvA frequency to a good approximation; while near the amplitude maximum, the measured frequency is the natural frequency of the resonant system. Plots of $1/H$ at the maximum or minimum of each cycle versus integers have usually shown a small change of frequency after the resonance maximum. Part of this change, however, is due to the phase shift effect (Section 3.2g).

Figure 3.1c shows another complicated modulation effect occurring in the α oscillations, in this case for the magnetic field along the $[110]$ crystal axis. The amplitude exhibits beats exactly in phase with the slower γ oscillations and it is thought that these beats are caused by some interaction between the α and γ oscillations rather than by an additional set of oscillations. We see from the picture that the minimum in the α 's occurs when the amplitude of the γ 's is passing through zero with positive slope. (Time is measured from right to left.) This result implies that the minima in the α oscillations occur at the minima in the magnetization due

to the γ oscillations M_γ , since in pulsed field measurements dM/dH is observed rather than M . Pippard¹ has suggested that this effect is caused by a fluctuation in the eddy currents produced when the strong amplitude γ oscillations change the effective magnetic field seen by the conduction electrons and hence change the sample resistance by the magnetoresistance effect. The increased eddy currents for M_γ a minimum would tend to wash out the oscillations as shown in Figure 3.1c. Furthermore, the transverse magnetoresistance saturates for all current directions for H parallel to $[110]$ (Alekseevskii and Gaidukov 1962) and gives additional weight to Pippard's suggestion.

On the other hand, although dM/dH can be fairly large, M/H is small and it does not appear possible that the γ oscillations can affect the resistance appreciably. In addition, Figure 3.1d shows the α oscillations for H parallel to $[111]$ where a twin T filter has been used to reject the γ oscillations. Although the fact can not be determined from this picture, these beats turn out to be in phase with the γ oscillations. However, the magnetoresistance does not saturate for this direction of H (Alekseevskii and Gaidukov 1962).

It thus seems unlikely that Pippard's suggestion is correct, but this requires further study. (See also Section

¹Pippard, A. B., Cavendish Laboratory, Cambridge, England. Modulation of α oscillations. Private communication (1962).

3.2.) From consideration of Figure 3.1d alone we might associate the beats with a new set of oscillations, but it is more likely that they are connected with the γ oscillations with which they are exactly in phase. Thus, to sum up, considerable caution must be used in interpretation of beats. Also, since the oscillations are, strictly speaking, periodic in B^{-1} , intermodulation effects may occur and give rise to extraneous beat patterns (Section 3.2).

3.2. Errors

Priestley (1961) and Shoenberg (ca. 1962) have both given comprehensive discussions of the errors in period measurements and their outline will be followed here.

The dHvA periods showed no measurable field or temperature dependence. Since even the longest periods in lead are so short that they are only barely observable by the torque method (Dhillon and Shoenberg 1955), it is impossible to check consistency by a comparison of pulsed-field measurements with steady-field torque results.

The periods from pulsed-field measurements are thought to be quite accurate if one takes the average of periods determined from rising and falling field at the same H (Section 3.2g). The results from different pulses agree closely and, in fact, the standard deviation, taken for at least ten measurements, was less than 1% for the periods of the stronger

oscillations. For some of the weaker oscillations, this deviation was 5%-6%. (See Table 4.1.)

There are several possible systematic errors that can occur in this experiment:

a. Standard Resistor. The 0.01 ohm Leeds and Northrup non-inductive standard resistor used in determining the current through the pulse coil, was compared with a 0.01 ohm Rubicon standard resistor from the Instrument Shop. A Leeds and Northrup Wenner potentiometer was used to make the comparison. The resistance was found to be $(1.0001 \pm 0.00005) \times 10^{-2}$ ohms. This resistor was calibrated three times during the period of a year and no measurable variation was found.

The temperature rise in the standard resistor during a pulse is certainly less than 10°C , which would imply a change in resistance of less than 0.02%, which is negligible. The magnetoresistance has not been measured for this standard resistor, but Priestley (1961) has checked the values for a similar resistor in a 2000 Gauss field and found the effect to be negligible. (See also part f.)

b. Pulse Magnet. The important periods in symmetry directions were measured with pulse coil C which was calibrated using NMR (Nuclear Magnetic Resonance) at low fields and found to give 114.2 ± 0.1 Gauss/amp (77°K). We also calculated the constant for coil C by summing over the layers and correcting for compensating turns. The calculated value

was 113.8 ± 0.05 Gauss/amp, where room temperature dimensions were used. Calibrations using other methods were good only to about 0.5%.

The coil was calibrated with direct current; but, since the dominant frequency component of the high-field pulse was only about 30 c/s, one would expect negligible difference from the calibrated value. The coil may change shape slightly during the field pulse, and thus cause an error in the measured value of the field. There are no direct high field measurements of sufficient accuracy to check this effect, and not even a good estimate of its magnitude seems possible. The epoxy resin which bonds the coil is rather inflexible at liquid nitrogen temperatures and cracking has been observed in the outer layers of resin that were too thick. Most of this cracking, however, was probably due to thermal shock on cooling. Therefore, since no better information is available at this time, it is assumed that changes in coil shape can be neglected.

c. Calibration Voltages. A Leeds and Northrup type K-3 potentiometer was used to check the output voltage of the calibrator unit, which was found to be accurate to 0.1% on all settings of the 'Decapot' voltage divider. A mercury cell provided a reference voltage and the balance was checked with the null indicator in the calibrator unit before each run.

d. Ground Loops. Ground loops were not a problem as the

voltage drop across the standard resistor was read differentially on the oscilloscope.

e. Oscilloscope Errors. Initially a Tektronix 555 oscilloscope was used. This instrument had a dual set of horizontal deflection plates and separate time-bases and it was therefore necessary to align the two traces before each run. In the center of the cathode-ray tube the traces were aligned to better than 0.3 mm, but within about 1 centimeter of either edge the traces were often separated by as much as 1 mm so that the edges of the pictures could not be used to determine periods. The error in the field measurement due to this effect is estimated to be less than 0.3%.

The more recent measurements were made with a Tektronix 502 oscilloscope which had only one set of horizontal deflection plates. With this scope no measurable difference in trace alignment or sweep velocity was found. A Tektronix time mark generator which had been calibrated against WWV was used for this check.

Drift of the vertical deflection amplifiers in the Tektronix 555 oscilloscope was another source of error, but this drift was not as serious as might be expected, since the bucking technique was always used (Section 2.2). The error in the calibration lines due to this drift could have been 0.2 of the spacing between lines which could cause an error of the order of 0.4% in the field measurement.

The drift of the vertical deflection amplifiers in the Tektronix 502 seemed to be much less. Repetition of calibration lines on the same photograph, after approximately 15 seconds delay, showed no appreciable displacement of the calibration lines. The error, when the 502 was used, is estimated to be less than 0.05%.

f. Period Differences for Rising and Falling Fields. When the de Haas-van Alphen period was measured for rising and falling fields by means of the resonant frequency technique, there was generally a difference of from 3%-8% with the higher period measured for falling field. (See columns 6 and 7, Table 4.1.) There are several contributions to this difference. Eddy currents in the thin-wall appendix of the stainless steel dewar are estimated to produce a magnetic field of less than 25 Gauss, a negligible contribution in this experiment. The self-inductance of the 0.01 ohm manganin standard resistor is estimated to be less than 10^{-7} h. For $dI/dt = 10^5$ amps/sec the induced voltage across the standard resistor would be 0.01 volt, causing an error in the field measurement of the order of 0.5%. This effect would increase the reading for a rising field and decrease it for a falling field. Taking the average period for both rising and falling fields should correct for this effect, if the field pulse is symmetrical about the maximum, which is very nearly true (Figure 3.1a).

Kosevich (1958) has studied the effects of eddy currents produced in a sample by a time-varying field. He obtained a rather complicated solution for an infinite cylinder with axis parallel to the magnetic field axis. Gold (1958a) has considered the effects of eddy currents assuming that the skin depth is much greater than the radius of the sample. With this simpler model he showed for his experiment ($H_{\max} \sim 80$ kG) that eddy currents had some effect on the amplitude, but negligible effect on the period.

The period is changed by a factor $(1 - \delta)$, where $\delta = \pi a^2 \dot{H} / H \rho$, a is the radius of the sample in centimeters, and ρ is the sample resistivity in a magnetic field in e.m.u. Thus, the measured period is less than the actual period for rising field and vice versa.

The eddy-current effect cannot be calculated accurately for the present experiment ($H_{\max} \sim 200$ kG), since there are no magnetoresistance measurements on lead single crystals at such high fields. However, the magnetoresistance has been measured on polycrystalline lead at fields up to 220 kG (Cotti et al. 1962, p. 523; Luthi 1960) and we shall use these data to make an order of magnitude estimate. Their material had a resistivity ratio $\rho_{293^\circ} / \rho_{0^\circ} \approx 4000$, which is roughly the same as the lead used in this experiment (Section 2.4). Their results fit an expression of the form:

$$\frac{\Delta\rho(H)}{\rho_T} = 2.18 \times 10^{-10} \left(H \cdot \frac{\rho_\Theta}{\rho_T} \right)^{1.5} \quad (3.5)$$

for $H\rho_\Theta/\rho_T > 10^7$ Gauss. ρ_Θ is the resistivity at the Debye temperature (90°K), and ρ_T is the resistivity at temperature T.

For the samples used in this experiment we estimate $\rho_\Theta/\rho_0 \sim 1200$ and therefore from Equation 3.5 $\Delta\rho/\rho_T \sim 100$ for $H = 50,000$ Gauss and $\Delta\rho/\rho_T \sim 800$ for $H = 200,000$ Gauss. Since at room temperature lead has a resistivity of the order of 2×10^{-7} ohm-meters, the pulsed field resistivities for $T = 1^\circ\text{K}$ become approximately:

$$\begin{aligned} \rho(50,000) &= 3 \times 10^{-9} \text{ ohm-meters} = 300 \text{ emu} \\ \rho(200,000) &= 2.4 \times 10^{-8} \text{ ohm-meters} = 2400 \text{ emu.} \end{aligned}$$

For $\dot{H}/H \sim 100$, $\delta \sim 4 \times 10^{-4}$ at 50,000 Gauss, which is negligible.

For H parallel to $[110]$ the magnetoresistance saturates for all current directions (Alekseevskii and Gaidukov 1962) and the value of δ might be larger, possibly of the order of 0.02. This contribution is important, but averaging the periods for increasing and decreasing fields will correct for this error. Also, the magnetoresistance minimum is very sharp, and it would be necessary to be very close to the $[110]$ to see any effect of eddy currents on periods. The effect on

amplitudes could be much more important and will be considered in the next section.

The most important contribution to the period difference for rising and falling fields is due to the phase change of π occurring when the time frequency of the dHvA oscillations passes through the resonant frequency of the pickup circuit. In Figure 3.2f, the phase change of the second harmonic passing through resonance can be observed against the constant phase of the fundamental. This effect again causes the measured period to be longer for rising fields and shorter for falling fields. Since normally from 25-50 cycles are measured, this effect would cause a difference of from 2% to 4% in the periods, which is at least half of the observed difference. Averaging the values for rising and falling fields also corrects for this effect.

g. Errors in Measuring Pictures. The magnetic field corresponding to a particular cycle on the dHvA trace is determined by using a traveling microscope to interpolate between calibration lines. The calibration unit (Section 3.2c) furnishes a bucking voltage accurate to 0.1%, so that only a small part of the actual voltage is measured on the film. Bucking voltages up to 15 volts have been used in this experiment and a value of 5 volts has been chosen for the following error estimates.

A small error is introduced if the horizontal direction

of travel of the microscope is not parallel to the calibration lines. This error is negligible for the conditions of this experiment; since, for example, a 5° mistake in alignment would cause an error in the field measurement of only 0.01%.

Another cause of reading error is the width of the field trace. Normally, this width is the source of a random error which is less than 0.05 of the separation of calibration lines. Since, for most accurate field measurements, the calibration lines have 0.1 volt separation, the reading error should be of the order of 0.1%. When the field trace crosses a calibration line, it is very difficult to obtain an accurate measurement and these crossing points should be avoided in period determinations. The most reliable results are obtained by plotting the reciprocal magnetic field at the maximum or minimum of each cycle versus integers, as explained in Section 3.1.

h. Summary. Period values can be trusted only if they are averaged at the same value of H for rising and falling fields. If this averaging is done, the stronger oscillations, for which from 30 to 70 cycles can be measured, should be accurate to about 1% while the weaker oscillations may be in error by up to 5%. The major unknown effect is the change in pulse coil constant at large magnetic fields, but this effect is expected to be small.

3.3. Amplitude Measurements

The cyclotron mass and collision broadening term in Equation 1.15 are determined from the variation of the amplitude with temperature and magnetic field, respectively. When pulsed magnetic fields are used, $dM/dt = dM/dH dH/dt$ is the quantity measured. From Equation 1.15 we find

$$\frac{dM}{dH} = \frac{4\pi kT}{(2\pi)^{1/2}} \left(\frac{e}{\hbar c}\right)^{3/2} \left(\frac{1}{P^2 H^{5/2}}\right) \left(\frac{\partial A}{\partial k_z}\right)^{-1/2} x \quad (3.6)$$

$$\sum_{r=1}^{\infty} \frac{r^{1/2} \cos\left(\frac{2\pi r}{PH} + \frac{\pi}{4} - 2\pi r\gamma\right) e^{\frac{-2\pi^2 r m^* c k x}{e \hbar H}} \cos \frac{\pi r m^*}{m}}{2 \sinh \frac{2\pi^2 r m^* k T c}{e \hbar H}}$$

Here only the sine term was differentiated as its argument is large for the magnetic fields and periods of this experiment.

The collision broadening term, $e^{\frac{-2\pi^2 r m^* c k x}{e \hbar H}}$, has been included in this expression. Normally the argument of the sinh term is large enough even for the fundamental that the sinh can be replaced by an exponential whereas the higher harmonics are not easily observed.

The pickup voltage, V , should be approximately given by:

$$V = -4\pi N(\pi a^2) \frac{dM}{dH} \frac{dH}{dt} \quad (3.7)$$

where N is the number of effective turns in the pickup coil (approximately 1000 for the coils used here).

From Equation 3.6 we find for the fundamental term:

$$\begin{aligned}
 V &= -4\pi N(\pi a^2) \frac{\partial H}{\partial t} \left\{ \frac{8\pi k T}{(2\pi)^{1/2}} \left(\frac{e}{\hbar c}\right)^{3/2} \left(\frac{1}{P^2 H^{5/2}}\right) \left(\frac{\partial^2 A}{\partial k_z^2}\right)^{-1/2} \right. \\
 &\quad \left. e^{\frac{-2\pi^2 m^* c k (T + x)}{e \hbar H}} \cos \frac{\pi m^*}{m} \cos \left(\frac{2\pi}{PH} + \frac{\pi}{4} - 2\pi\gamma\right) \right\} \quad (3.8) \\
 &= A(H, T) \cos \left(\frac{2\pi}{PH} + \frac{\pi}{4} - 2\pi\gamma\right)
 \end{aligned}$$

Since the only part of Equation 3.8 that depends on the tem-

perature is $T e^{\frac{-2\pi^2 m^* c k (T)}{e \hbar H}}$, a plot of $\ln A/T$ versus T should be a straight line with slope $\frac{-2\pi^2 m^* c k}{e \hbar H}$, from which the effective mass m^* can be determined. Similarly, a plot of $\ln (AH^{5/2})$ versus H^{-1} should have a slope $\frac{-2\pi^2 m^* c k (T + x)}{e \hbar}$. Then if m^* is known, the collision broadening temperature x can be found.

In this study only the temperature variation of amplitude was studied and no attempt was made to investigate the field dependence. The resonance technique is necessary for the separation of most periods found in lead and the relationship for the amplitude as a function of field has not been completed worked out for these conditions. (See Shoenberg (ca.

1962) for a calculation in which damping was omitted.)

For a study of the temperature dependence, the amplitude $A(H,T)$ was taken as the size of the resonant blip. Unlike period measurements, these determinations of amplitude as a function of temperature are not very accurate; in fact, effective masses determined in this manner may be in error by more than 10%.

There are many possible factors that can affect the amplitudes. Variations may be caused by changes in the peak field H_{\max} and the shape of the field pulse. If the interval between pulses is not sufficiently long to dissipate the heat in the coil, both H_{\max} and \dot{H} will be altered and as a consequence the dHvA amplitude will change. In practice approximately 5 minutes were allowed between pulses. This interval was about twice the length of time that noticeable boiling occurred in the liquid nitrogen. In addition, as the helium level falls, the resistance of the pickup coil leads increases and the Q of the circuit is decreased. Mechanical vibrations and changes in the orientation of the rotating pickup coil can also affect mass measurements. (In this experiment only stationary pickup coils were used for mass determinations.)

Heating effects due to eddy currents in the sample and the magnetocaloric effect in the glass capillary are also important. Shoenberg (ca. 1962) has considered these effects for the noble metals and concluded that during a pulse the

temperature increase below the λ point is negligible, but there may be a temperature rise of the order of 0.1°K above the λ point. Although the radius of lead samples used in this experiment is from two to four times the radius of one of Shoenberg's copper whiskers, the magnetoresistance in lead is also larger, and his conclusions are probably reasonable for lead as well. For magnetic fields in directions where saturation occurs, $[110]$, the heating problem might be expected to be more critical, but we have found no evidence for any serious effect. Unfortunately, many of the parameters necessary for a detailed calculation are uncertain.

Eddy currents can also affect the amplitudes more directly. As Gold (1958a) has shown, the amplitude is reduced by a factor

$$A/A_0 = \frac{\sin \frac{\pi \delta}{PH}}{\frac{\pi \delta}{PH}} = \frac{\sin \frac{\pi^2 a^2 \dot{H}}{PH\rho H^2}}{\frac{\pi^2 a^2 \dot{H}}{PH\rho H^2}} \quad (3.9)$$

and for most orientations of the magnetic field, this reduction of amplitude is negligible for $H > 60,000$ Gauss.

However, if a magnetic field in the $[110]$ direction is considered, where saturation should occur, this might not be the case. Long beats might appear with period in $1/H$ of $P' = HY/H_0$, where $\gamma = 2P\rho_s/\omega\pi a^2$, ρ_s is the saturation value for the resistivity, and the pulsed magnetic field is assumed to

vary according to $H = H_0 \sin \omega t$. A very crude estimate of ρ_s is 6 emu for H in the $[110]$ direction. This value is estimated from the data of Alekseevskii and Gaidukov (1962) and Luthi (1960). Then $\gamma \sim 3 \times 10^{-6}$ and $P' \sim 3 \times 10^{-6} H/H_0$. This result does not account for the long beats in the γ oscillations (Chapter 4) since they extend over an angular region of at least 25° whereas the magnetoresistance minimum is very sharp ($< 5^\circ$). Also, due to eddy currents these beats would not be periodic in $1/H$, as the long beats are found to be. It would be interesting to study carefully the oscillations for a $[110]$ orientation in order to look for these beats.

Another factor affecting the amplitude is a frequency modulation effect which may be important when the dHVA amplitudes are large. The actual field seen by the electrons in the sample is the B field rather than the externally applied magnetic field.¹ Therefore, in the expression for the magnetization M (Equation 1.15) the external field H should be replaced by $H + 4\pi M$. As H varies, the effective field oscillates with M; and, since dM/dH can be appreciable even for M small, the effect is important. Shoenberg (ca. 1962) has considered this problem in connection with the large amplitude of some of his harmonics and has made a preliminary calcula-

¹Shoenberg, D., Dept. of Physics, University of Cambridge, Cambridge, England, and Holstein, T., Dept. of Physics, University of Pittsburgh, Pittsburgh, Pennsylvania. Magnetic fields in lead. Private communication (1962).

tion valid for small amplitudes. This calculation indicates that the frequency modulation effect could increase the amplitudes of the higher harmonics at the expense of the fundamental. This effect should be important at the lowest temperatures where the oscillations are strongest, and will be considered in Chapter 4 in connection with effective mass measurements. Frequency modulation can also cause mixing to produce "combination tones", but no definite evidence for this effect has been found in lead.

4. EXPERIMENTAL RESULTS

4.1. The Empty Lattice or Single OPW

Model for Lead

As we have mentioned before, the dHVA periods can be fitted quite successfully into a nearly free electron model in which only the connectivity of the free electron Fermi sphere is altered at intersections with Bragg planes (Chapter 1). We shall label this model by the more impressive title of the single OPW model. In order to classify the periods observed it is helpful to relate them to this model. Therefore, before proceeding to the experimental results, we shall digress somewhat and describe the single OPW Fermi surface for lead.

Lead is a face-centered-cubic metal with a lattice constant $a_0 = 4.94 \times 10^{-8}$ cm at room temperature (Kittel 1956, p. 40). At 0°K this value is approximately 4.90×10^{-8} cm.¹ The reciprocal lattice points form a body-centered-cubic structure and Figure 4.1 shows the fundamental Brillouin Zone. The notation of Bouckaert et al. (1936) is used to label symmetry points and lines.

¹The difference between the lattice constant at room temperature and that at 0°K has been estimated from the thermal expansion data of White (1962).

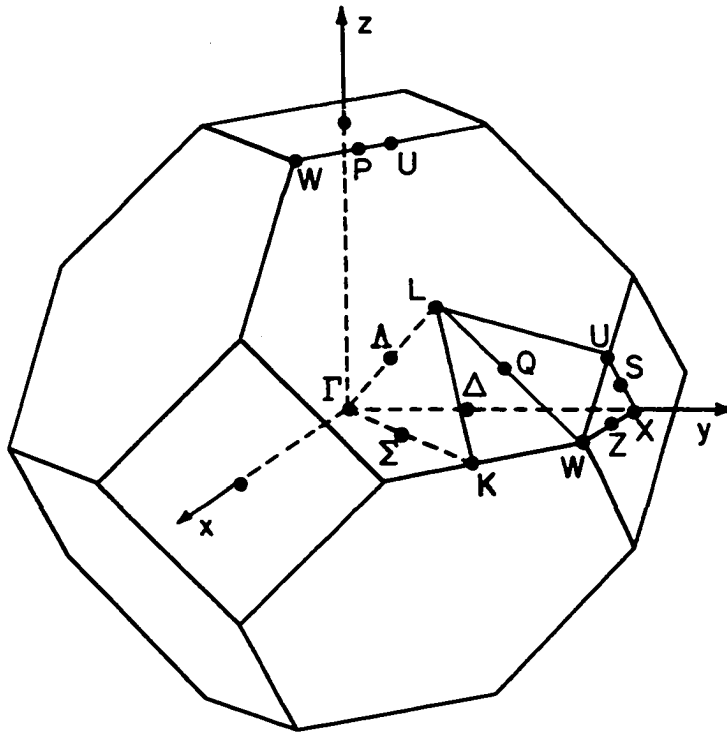


Figure 4.1. Fundamental Brillouin zone for the fcc lattice
(The letters label symmetry points and lines.)

If four valence electrons are assumed for lead, Harrison's method (See Sec. 1.1.) can be used to determine the single OPW Fermi surface which is shown in Figure 4.2. The first band is full, in the second band the Fermi surface contains a large hole region, the Fermi surface in the third band encloses a multiply-connected structure containing electrons, and small pockets of electrons are shown in the fourth band. Note that in this figure, although the first and second bands are centered about Γ , the third and fourth are centered about X and L, respectively.

Lead often appears to have only two valence electrons when it combines chemically with other elements. For this reason Hume-Rothery¹ has argued that only two electrons per atom should be considered in drawing the Fermi sphere for lead. However, positron annihilation studies in polycrystalline lead (Wallace 1960, p. 30) point toward four conduction electrons per atom. In addition, if a two valence sphere is assumed, there will be no portion of the Fermi surface (Figure 4.2) producing short period oscillations with period nearly independent of orientation corresponding to the α oscillations described later in this chapter. It will be shown that the Fermi sphere for four valence electrons per atom fits the dHVA results qualitatively and this will be the starting point for

¹Hume-Rothery, William, Dept. of Metallurgy, University of Oxford, Oxford, England. Fermi surface of lead. Private communication (1961).

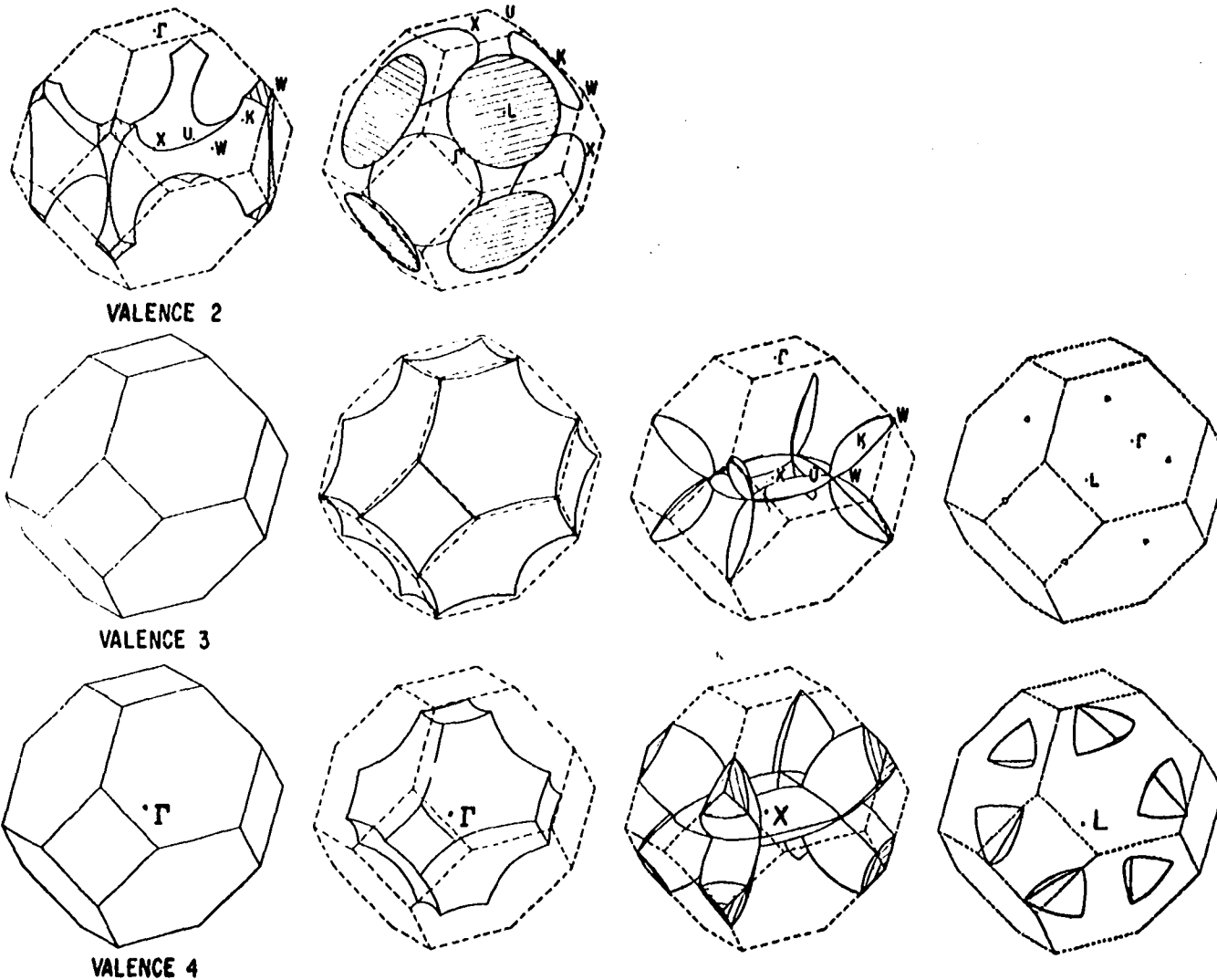


Figure 4.2. Fermi surfaces of fcc metals according to the single OPW approximation (after Harrison 1960b)

the Fermi surface model considered.

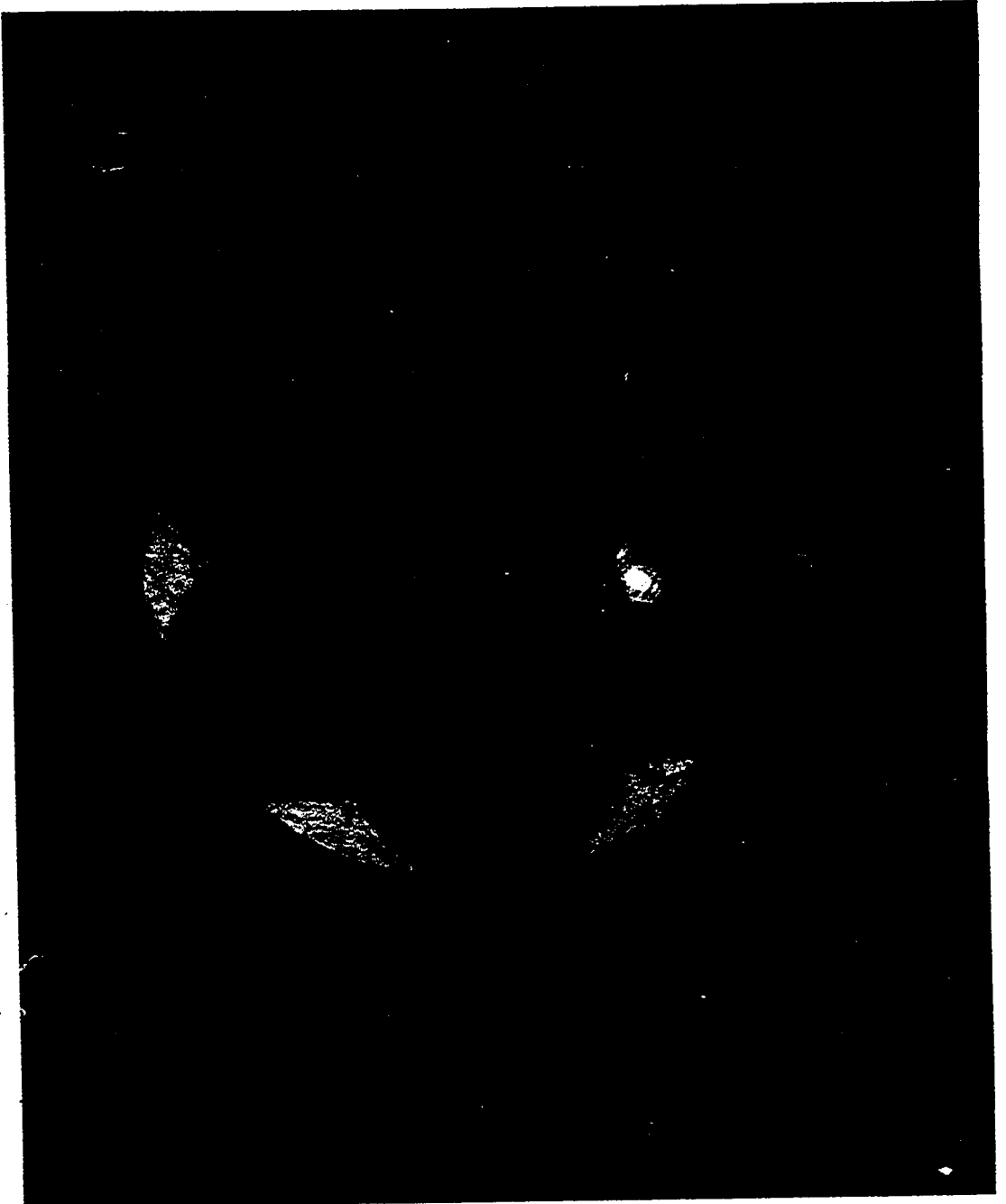
In his original paper Gold (1958b) suggested that the γ oscillations were due to pockets of electrons in the fourth band as well as the third band electron surface. Later he noted that better agreement with other experiments would be obtained if the fourth band were assumed empty (Gold 1960). We have followed this suggestion and consider only the second and third bands in our description of the Fermi surface.

The α oscillations to be described in the next section will be associated with the second band. The complexity in the description is introduced by the third band surface which may be considered as a 'thickening-up' of the $[110]$ lines forming the boundary of the primitive Brillouin zone. The remaining oscillations can be related to this surface as will be shown in Section 4.2. Figure 4.3 shows a model of the single OPW third band Fermi surface made from 36 identical pieces or arms with axes in $[110]$ directions. In Figure 4.4 we show the same surface where, for simplicity, we have replaced the single OPW arms by pipes in order to illustrate the possible orbits.

4.2. Period Measurements for Symmetry Orientations

The construction of a Fermi surface model requires good period values particularly at symmetry directions. Therefore, the first sample holders were constructed with stationary

Figure 4.3. Single OPW model of third band Fermi surface of lead



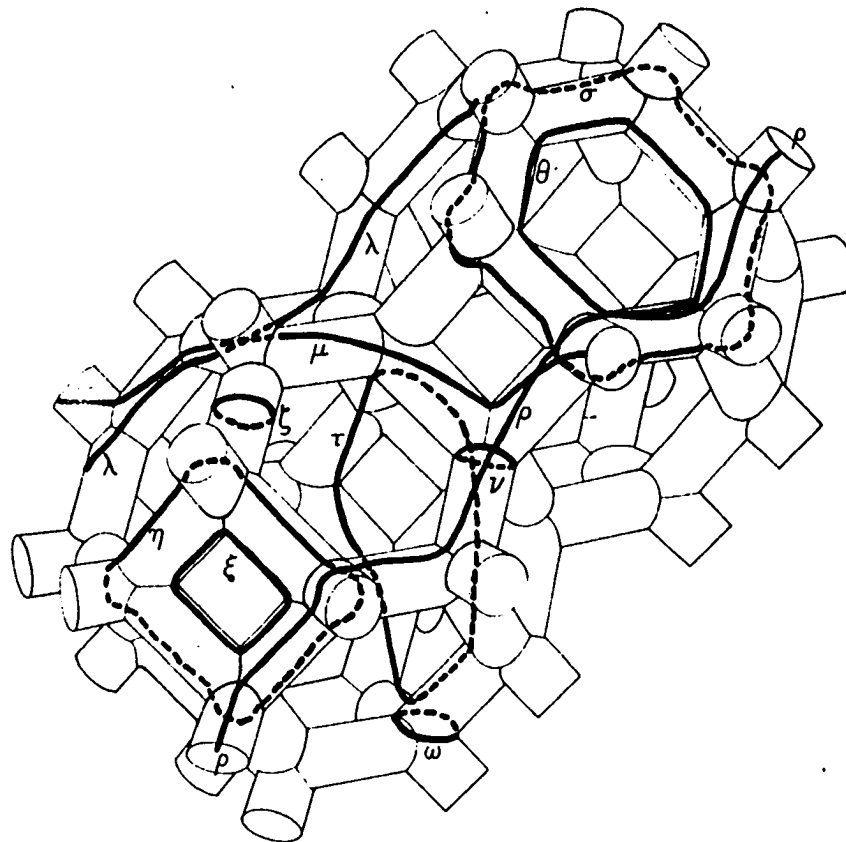


Figure 4.4. Pipe model of third band Fermi surface of lead

pickup coils and measurements were made with the magnetic field along the symmetry axes of the crystal, $[100]$, $[110]$, and $[111]$. Table 4.1 shows the periods found for symmetry orientations of the crystal. In his investigation of lead, Gold (1958b) classified his oscillations α , β , and γ . This notation is retained and noted in the first column of the table where other Greek letters, μ , ϵ , and δ , have been used for the new sets of oscillations.

The period values are given for both rising and falling fields, and for most oscillations differ by from 3% to 8%. The main part of this difference can be attributed to the phase change when the dHvA time frequency passes through the resonant frequency of the pickup circuit as discussed in Chapter 3. The average periods in Gauss⁻¹ have been converted into areas using $A_0 = 5.80 \times 10^{-9}/P$ where A_0 is given in units of $(2\pi/a)^2$ and a , the lattice constant of lead at $T = 0^\circ\text{K}$, has been taken as 4.90×10^{-8} cm (Section 4.1). This result is shown as the observed A_0 in the ninth column of Table 4.1. For observation of most of these periods the resonance technique was used and the third column indicates the approximate magnetic field at which the resonance occurred. In many cases the same oscillations were observed at several field values by a change of resonant frequency or capacitor charging voltage and the value given in the table is the one primarily used.

The fourth column refers to Figure 4.4 where for convenience the orbits in the third band have been labeled on the pipe model. The areas enclosed by these orbits have been calculated according to the single OPW model and these results are shown in the last column of Table 4.1. The association of a period with an orbit in this table is based primarily upon a one to one correspondence between the observed areas and those of the single OPW model. The remaining columns in the table will be discussed in Chapter 6.

The periods observed for symmetry orientations will now be described in some detail:

[110]

For the magnetic field along a [110] crystal axis, three separate periods were observed. The α and γ oscillations had previously been investigated by Gold and are thought to refer to the second-band hole surface and the third-band multiply-connected surface of arms along [110] directions, respectively. Long beats in the γ oscillations were studied and approximately 40 cycles/beat were found; this implies the existence of two periods differing by approximately 2.5%. The third set of oscillations labeled μ had a period between the values for the γ and the α oscillations. In order to see these oscillations it was necessary to filter out the stronger γ oscillations. Because only from ten to fifteen cycles were observed, this period is not accurately determined. These μ

Table 4.1. dHVA periods and extremal areas for lead

Oscillation	Orientation	Band	Orbit	$\sim H$ (kG)	Period $\times 10^8$ (Gauss $^{-1}$)			A_0 (units of $(2\pi/a)^2$)			
					$\dot{H} > 0$	$\dot{H} < 0$	Average	Observed	Calculated		
									Two parameter OPW models ^a		Single OPW model
				A	B						
γ'	$[110]^b$	3	ζ	60	5.16 ± 0.03	5.44 ± 0.03	5.30 ± 0.03	0.109 ± 0.001	0.110	0.113	0.158
α	$[110]$	2	α	130	0.570 ± 0.006	0.618 ± 0.006	0.594 ± 0.006	0.976 ± 0.01	1.1	1.05	1.16
μ	$[110]^c$	3	ω	166	1.62 ± 0.08	1.90 ± 0.08	1.76 ± 0.08	0.33 ± 0.02	0.25	0.36	0.37
γ	$[110]^{cd}$	3		155	2.60 ± 0.07	2.80 ± 0.07	2.70 ± 0.07				
γ''	$[100]^e$	3	ξ	90	4.0 ± 0.2	4.59 ± 0.2	4.3 ± 0.2	0.135 ± 0.006	0.156	0.126	0.133
θ	$[100]$	3	ν	60	1.81 ± 0.01	1.94 ± 0.01	1.88 ± 0.01	0.309 ± 0.002	0.311	0.311	0.300
β	$[100]^f$	3		140	0.87 ± 0.03	0.98 ± 0.03	0.93 ± 0.03				

^aModel A: $V_{111} = -0.069$ ry, $V_{200} = -0.039$ ry; Model B: $V_{111} = -0.045$ ry, $V_{200} = +0.052$ ry.

^bLong beats are observed indicating a second period differing by about 2.5%. Because of the uncertainty in which of the two periods relates to the central section of an arm (orbit ζ), we regard this number as the possible error for purposes of calculation in Chapter 5.

^cFiltering techniques were required.

^dSecond harmonic of $[110] \zeta$.

^eBecause of the complicated beating effects in the γ oscillations for the field near $[100]$ this period may be too large by as much as 10%.

^fSecond harmonic of $[100] \nu$.

Table 4.1 (Continued).

Oscillation	Orientation	Band	Orbit	$\sim H$ (kG)	Period $\times 10^3$ (Gauss $^{-1}$)			χ^2/ν (units of $(2\pi/a)^2$)				
					$H > 0$	$H < 0$	Average	Observed	Calculated Two parameter OPN models ^a		Single OPN model	
								A	B			
ϵ_1	[100] ^c	3	η	165	0.30 \pm 0.02	0.34 \pm 0.02	0.32 \pm 0.02	1.8 \pm 1	1.48	1.63	1.66	
ϵ_2	[100] ^c	2	α	160	0.33 \pm 0.02	0.41 \pm 0.02	0.39 \pm 0.02	1.5 \pm 1	1.63	1.53	1.83	
ϵ_3	[100] ^{cg}	3		162	0.48 \pm 0.03	0.49 \pm 0.03	0.49 \pm 0.03					
γ	[111] ^h	3	ξ	90	4.6 \pm 1	4.9 \pm 1	4.75 \pm 1	0.122 \pm 0.003	0.126	0.126	0.187	
α	[111]	2	α	125	0.604 \pm 0.006	0.643 \pm 0.006	0.626 \pm 0.006	0.93 \pm 0.01	0.94	0.93	1.05	
α	[111] ^{cl}	3		168	2.9 \pm 1	3.3 \pm 1	3.1 \pm 1					
δ_1	[111]	3	θ	115	0.87 \pm 0.01	0.89 \pm 0.01	0.88 \pm 0.01	0.66 \pm 0.007	0.66	0.65	0.72	
δ_2	[111] ^j	3	σ	145		0.27 \pm 0.02	\sim 0.26 \pm 0.03	\sim 2.2 \pm 3	2.2	2.45	2.5	
	[100]	4							0.020		0.077	
	[100]	4							0.028	Empty	0.11	
	[100]	4							\sim 0.025			
	[100]	4							\sim 0.025			0.03

^cPossibly fourth harmonic of [100] v.

^hThis crystal may have been 4° from [111].

ⁱSecond harmonic of [111] α .

^jThis period was only measured on falling field.

oscillations are associated with the orbit ω on the third band surface.¹

[100]

For the magnetic field along a [100] crystal axis Gold's γ and β oscillations were observed as well as several new sets of oscillations. The β oscillations have very large amplitude; in fact, both the second and third harmonics have been seen. These β oscillations were originally associated with the orbit ξ (Gold 1958b), but here they have been reinterpreted to be associated with the orbit ν , in better agreement with the OPW model. This correspondence is used in the fitting procedure described in Chapter 5 and will be discussed in Chapter 6.

The two additional periods observed for this orientation have been associated with the second band hole surface and a large electron orbit in the third band. As no orientation studies have yet been made of these periods because of their low amplitudes, their assignments are uncertain. If the single OPW model is a reasonable approximation, as we rotate the magnetic field away from the [100] direction toward [110], one set of oscillations should eventually die out corresponding to orbit γ while the other should merge smoothly into the α oscillations.

¹The orbit ω was first suggested by Young (ca. 1962) on the basis of rf polarization effects in his cyclotron resonance studies of lead.

[111]

For the magnetic field in the [111] direction two sets of oscillations were observed in addition to Gold's α and γ oscillations. These new oscillations are labeled δ_1 and δ_2 and are assumed to be produced by electrons in the third band. Figure 3.1f is a photograph of the longer period oscillations δ_1 which are assumed to be related to the orbit θ . The shorter period oscillations δ_2 were observed only with very large pulsed fields, approximately 200 kG maximum. These oscillations were studied only for falling fields ($\dot{H} < 0$).

Returning to Table 4.1, we see that the observed areas are very close to the single OPW areas. This correspondence suggests the possibility of modifying the single OPW surface slightly to obtain an accurate description of the Fermi surface (Chapter 5).

4.3. Orientation Dependence of dHvA Periods

Rotation studies were made only in a (100) plane. These studies were carried out in an attempt to verify the association of periods with the orbits given in Figure 4.4. Gold associated the β oscillations with an orbit inside the square face of the Brillouin zone (ξ in Figure 4.4). Better agreement with the single OPW model is obtained if these oscillations are associated with the ν orbit; and, since beats are observed in the γ oscillations for the field in the vicinity

of the $[100]$ crystal axis, the extra term giving rise to the beats might well be the orbit ξ .

Figure 4.5 shows the periods found for rotation in the (100) plane. For the β oscillations periods were measured for both $\dot{H} > 0$ and $\dot{H} < 0$, and the average is given in the diagram. These oscillations disappear for the field approximately 29° from the $[001]$ direction. We can make some qualitative judgements as to the nature of the surface responsible for the β oscillations from the following considerations. For a cylinder with axis along the $[001]$ direction the period would vary as $P(\theta) = P(0) \cos \theta$ where θ is the angle between the $[001]$ direction and the field direction; for a hyperboloid of revolution about the $[001]$ $P < P(0) \cos \theta$ and for an ellipsoid of revolution $P > P(0) \cos \theta$. The period of the β oscillations varies more rapidly with angle than $P(0) \cos \theta$ suggesting that the surface is formally of the hyperboloid type. The orientation dependence of the period due to the single OPW orbit ν has been calculated and is plotted in Figure 4.5 as a smooth curve nearly fitting the experimental points for the β oscillations.

The γ periods measured only for $\dot{H} > 0$ are shown in the upper part of Figure 4.5. The region near $[001]$ was investigated rather thoroughly, but only a few field directions near $[011]$ were studied. The oscillations have been divided into two groups: the γ' oscillations which were dominant

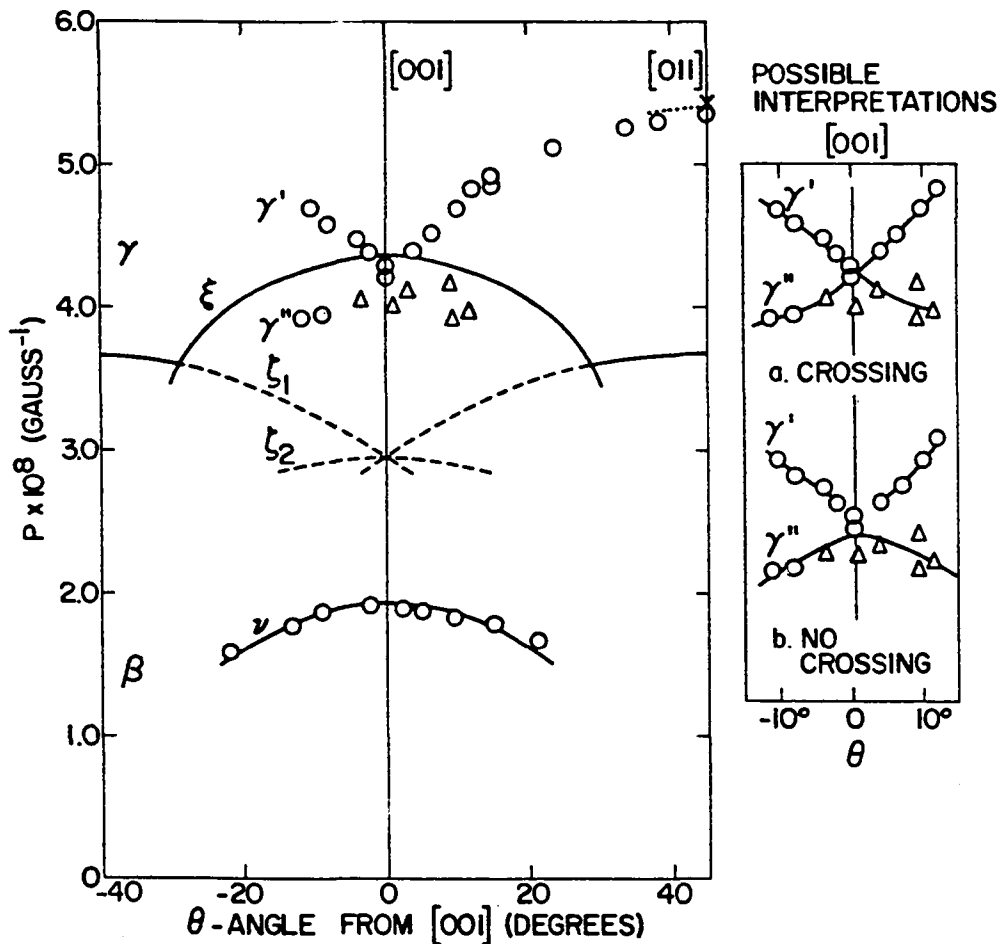


Figure 4.5. Orientation dependence of dHvA periods in a (100) plane

- (o) Experimental points for specimens with $[100]$ axis along the wire
- Δ Calculated from beat periods
- ... Calculated from long beats in the γ oscillations which were studied only for H near $[110]$

The lines are obtained from the single OPW Fermi surface where periods corresponding to non-extremal cross-sections are shown schematically as dashed lines.)

allowing accurate period measurements, and the shorter period γ'' oscillations determined primarily from beats. In addition, the long beats, mentioned in Section 4.2, occurred in the γ' oscillations; but these were studied only for H near $[011]$, and therefore are not shown in detail in Figure 4.5. (The orientation dependence of the long-beat periods has been discussed by Gold (1958b).)

For field directions near $[001]$ the pattern of the γ oscillations is somewhat complicated and more than two sets of oscillations may be present. The γ'' periods have been determined from the γ oscillations under the assumption that only two sets of oscillations occur; and these values may, therefore, not be reliable. In addition, it is not possible to decide from these data whether crossing curves occur for $H // [001]$.

As an aid in interpreting these measurements we have included in Figure 4.5 the orientation dependence of the single OPW orbits: ξ , corresponding to an orbit centered at X in the Brillouin zone, and ζ corresponding to an arm cross-section (Figure 4.4). Symmetry does not require this latter orbit to be extremal for H in a (100) plane except for H parallel to $[110]$. Consequently, there is no a priori reason to observe a period due to orbit ζ_1 away from $[110]$ and dashes have been used to stress this fact. As an illustration we show in Figure 4.6 a plot of single OPW areas normal to $[001]$ for

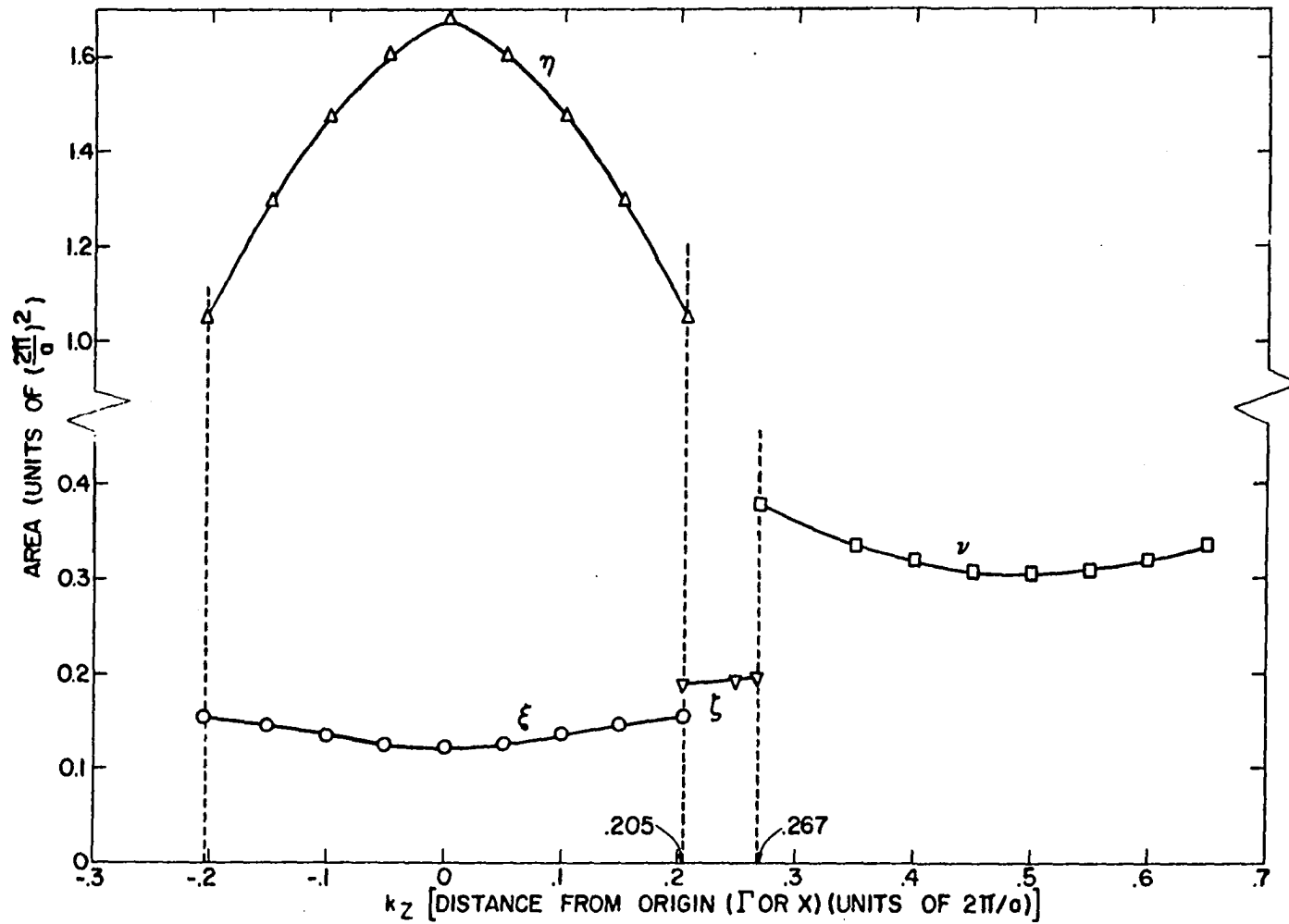


Figure 4.6. Single OPW areas normal to the [001] direction

sections taken at varying distances k_z from Γ . We note that the orbit ζ exists only over a short range of k_z and is not extremal although in reality dA/dk_z may be small enough to give rise to dHvA oscillations.

According to the single OPW model ζ_1 can continue as a non-extremal orbit approximately 4° beyond $[001]$ and an additional orbit ζ_2 will exist as well. Possible periods corresponding to areas enclosed by these orbits have been included somewhat schematically in Figure 4.5 as dashed lines.

This single OPW model points out two possibilities for the γ oscillations that can occur for H near $[001]$:

a. The curves can cross at $[001]$ and continue for a few degrees (Insert a Figure 4.5). In this case several sets of periods could be observed due to the ζ orbits as suggested by the dashed curves. Khaikin and Mina (1962) have observed several cyclotron masses for this orientation and their results would seem to favor this possibility (Chapter 6). However, because of the lower phase, it is possible to observe masses for non-extremal orbits using cyclotron resonance while the corresponding dHvA periods would probably not be detected. A drawback to this interpretation is that it would lead us to expect yet a further set of oscillations due to the orbit ξ . This orbit is extremal, but no distinct oscillations with period appropriate to ξ have been found.

b. No crossing occurs and the γ' oscillations die out a

few degrees before reaching $[001]$ (Insert b Figure 4.5). Only one set of γ -oscillations (γ'') would be observable at $[001]$ and these should arise from orbit ξ . While with this interpretation the drawback of possibility a does not exist, it is surprising that the oscillations due to the favorable orbit ξ should be of relatively low amplitude.

From the qualitative considerations just given we conclude that the observed results near $[001]$ may be better accounted for by possibility b. However, further study using new experimental techniques with greater resolution is required to decide quite unambiguously between the two possibilities.

4.4. Cyclotron Mass Measurements

As another approach to classifying the β oscillations, we measured cyclotron masses for the magnetic field along the $[001]$ crystal axis using the temperature dependence of amplitude (Section 1.3). The resonance technique was used; a resonant frequency of 47 kc separated the β and γ oscillations satisfactorily. The amplitudes for a set of oscillations were measured at approximately the same value of field and from three to five minutes were allowed between pulses for the pulse coil to cool. In spite of these precautions, there was considerable variation in amplitude resulting in an estimated uncertainty of 15% in the experimental mass values. Figure

4.7 shows a plot of $\ln A/T$ versus T for both the β and γ oscillations. From the graph, allowing for the uncertainty in measurement, the plot appears to deviate from a straight line below the λ point (2.19°K) for both the β and γ oscillations. Shoenberg (ca. 1962) has found a similar effect in some copper whiskers and suggests two reasons for this: Above the λ point, heating effects may become important and cause the measurement to give too large a value for the mass. If this effect is important, a change in slope might be expected at the λ point. A second reason for the change of slope is the frequency modulation effect discussed in Section 3.2. As the temperature decreases, the amplitudes become larger; but, because the B field rather than the applied magnetic field is the one seen by the electron, the amplitudes of the higher harmonics may be increased at the expense of the fundamental. The amplitudes measured at the lowest temperatures are too small and consequently the measured mass is too small. This effect would not necessarily cause a break at the λ point, but a gradual change in slope should take place. In our plot the variation appears gradual and suggests this latter effect as its primary cause. We therefore determine our masses from the slope at higher temperature. The resulting values are:

$$(m^*/m)_\beta = 1.30 \pm 0.15 \text{ and } (m^*/m)_\gamma = 0.85 \pm 0.1.$$

The value for the β oscillations is in good agreement with the results of Khaikin and Mina (1962) who associate this

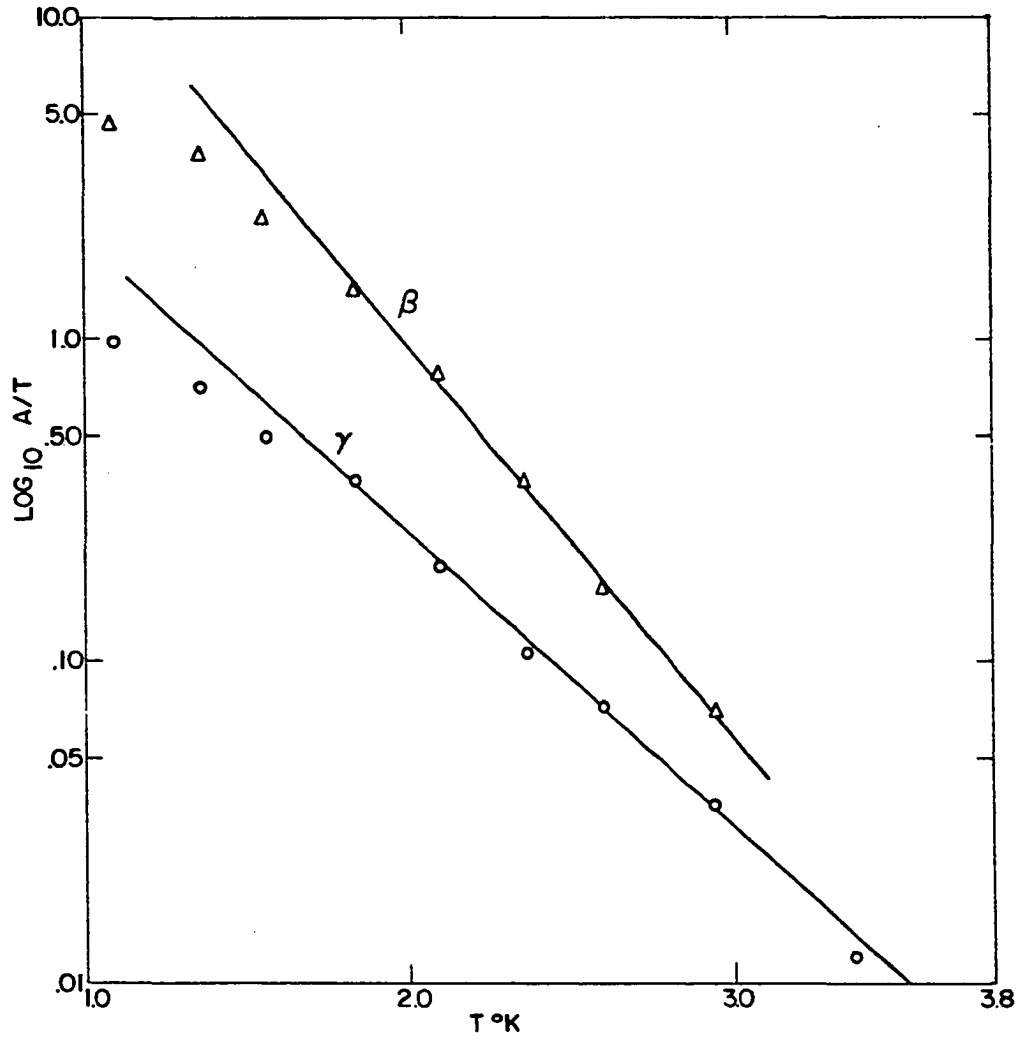


Figure 4.7. Plot of $\log_{10} A/T$ versus T for β and γ oscillations

mass with the ν orbit and may have used rf polarization to infer this (Chapter 6). However, the mass value for the γ oscillations lies between two masses observed by Khaikin and Mina, $(m^*/m)_\zeta \sim 0.75$ and $(m^*/m)_\xi \sim 0.93$. Because of the uncertainty in this measurement, the mass of the γ oscillations could be either of these two masses or might be a resultant of masses due to more than one orbit.

Since a second period in the γ oscillations has been found only from beats for orientations near $[001]$, it has not been possible to resolve two masses in the γ oscillations. Again, more careful measurements should be made to study details of the oscillations near the $[001]$ direction.

4.5. Comparison of Experimental and Calculated Amplitudes

Although areas may be accurately determined from period measurements using Equation 1.14, the absolute values of amplitudes may depend upon factors not included in Equation 3.8 such as crystal perfection. Gold (1958b) has noted that lead has a filamentary structure which could cause a reduction in amplitude, especially for the shortest period oscillations, but this should not be important for symmetry directions where the periods take maximum or minimum values.

The amplitudes to be expected for the α and γ oscillations for $H // [110]$ and the β oscillations for $H // [100]$ can be

estimated from Equation 3.8. If we assume a temperature of 1°K , the pickup voltage becomes approximately:

$$V = \frac{7.8 \times 10^{-9} \cot \omega t}{P_H^{3/2} \left(\frac{\partial^2 A}{\partial k_z^2} \right)^{1/2}} e^{\frac{-2\pi^2 m^* c k (1^\circ + x)}{e \hbar H}} \cos \pi \frac{m}{m^*},$$

where we have assumed $\dot{H}/H = \omega \cot \omega t$ and $\omega \sim 220 \text{ sec}^{-1}$ for our pulse coil.

The curvature factors for the γ and β oscillations have been estimated from the single OPW ζ and ν orbits, respectively, while for the α oscillations the value for a sphere is assumed. From the field dependence of the amplitude Gold (1958b) has estimated the values of x for the γ and β oscillations to be 2.0 and 13, respectively. Since x is not known for the α oscillations, a range of values is assumed. Table 4.2 shows these amplitude estimates compared with experimental values.

The agreement is satisfactory for the β and γ oscillations, but a large value of x is required in order that the calculated amplitude of the α oscillations agree with experiment. Some additional factors must contribute to the reduced amplitude of the short period α oscillations. One of these could be a reduction due to eddy currents (Chapter 3). The dHvA amplitudes are not very well understood.

Table 4.2. Comparison of calculated and experimental pickup voltages

Oscillations	H	P	$\frac{\partial^2 A}{\partial k_z^2}$	x	$\frac{m^*}{m}$	$\frac{+2\pi^2 m^* ck(T+x)}{e \hbar H}$	V_{cal}	V_{exp}
	kGauss	Gauss ⁻¹		°K			mv	mv
α at [110] (second band)	90	6 x 10 ⁻⁹	2 π	3-6	1.0 ^a	6.2-11	8.5-0.4	0.5-0.1
β at [100] (orbit v)	80	5.3 x 10 ⁻⁸	1.3	1-2	1.30	4 - 6	16 -2	10 -5
γ at [110] (orbit ζ)	70	1.9 x 10 ⁻⁸	2.3	1-3	0.56 ^a	1.7- 3.5	3-0.54	5 -1

^aGold (1958b).

5. DESCRIPTION OF THE FERMI SURFACE

5.1. Introduction

Two approaches were tried out to find a suitable representation of the lead Fermi surface. The first was an expansion of $E(k)$ at the Fermi surface in a symmetrized triple Fourier expansion. The second method was based on an orthogonalized-plane-wave (OPW) approach using the procedure described by Harrison (1960a). This latter method was more successful in describing the free electron-like lead Fermi surface and it was also easier to attach physical significance to the expansion coefficients.

5.2. Fourier Expansion Method

This method will be described only briefly as it was not used in the final description of the Fermi surface. Garcia-Moliner (1958) first suggested that the Fermi surface of copper as determined by Pippard (1957) could be fitted to 1% by an analytic function which is the first two terms of a symmetrized triple Fourier expansion. This achievement suggested the possibility of fitting the surface of lead to a similar expansion. The expansion fits the surface from only one zone at a time. Since we had the most information about the third-zone multiply-connected surface, we decided this surface would

be a good test of the method.

The general form for the expansion of $E(\mathbf{k})$ for a fcc structure is:

$$\begin{aligned}
 E(\mathbf{k}) = & \sum_{l,m,n} A_{lmn} \left\{ \cos \frac{a}{2}(l+m)k_x \cos \frac{a}{2}(n+1)k_y \cos \frac{a}{2}(m+n)k_z \right. \\
 & + \cos \frac{a}{2}(l+m)k_x \cos \frac{a}{2}(m+n)k_y \cos \frac{a}{2}(n+1)k_z \\
 & + \cos \frac{a}{2}(n+1)k_x \cos \frac{a}{2}(l+m)k_y \cos \frac{a}{2}(m+n)k_z \\
 & + \cos \frac{a}{2}(n+1)k_x \cos \frac{a}{2}(m+n)k_y \cos \frac{a}{2}(l+m)k_z \\
 & + \cos \frac{a}{2}(m+n)k_x \cos \frac{a}{2}(l+m)k_y \cos \frac{a}{2}(l+n)k_z \\
 & \left. + \cos \frac{a}{2}(m+n)k_x \cos \frac{a}{2}(n+1)k_y \cos \frac{a}{2}(l+m)k_z \right\} \quad (5.1)
 \end{aligned}$$

While the above is a purely formal expression which satisfies the crystal symmetry requirements, we may remark that the coefficients of this expression are matrix elements of the total Hamiltonian between Wannier functions (Slater 1956) centered on different atoms and these coefficients depend only on the vector difference $\underline{R}_i - \underline{R}_j$ between the two atoms. Since Wannier functions are fairly localized, it was thought that the expansion might converge rapidly, and therefore only a few coefficients would be needed to fit the Fermi surface. Thus two cross-sectional areas, which were used to select E/A_{100} and E/A_{111} , were chosen as follows:

1. The first area was the cross-section of an arm in the third band normal to the $[110]$ direction and passing through

the point U. (See Figures 4.1 and 4.2.) This area was obtained from the period of the γ oscillations for H parallel to $[110]$. Because of the long beats this area is uncertain by at least 1%-2% (Section 4.1).

2. The second area was the cross-section inside a square face of the Brillouin zone, i.e. normal to the $[100]$ direction and centered around the point X. This area was originally assumed to give rise to the β oscillations but was later associated with the γ'' oscillations (Section 4.3).

When parameters chosen in the above fashion were used, it was possible to predict the areas of certain other orbits, but these did not agree well with experiment. For this reason two additional parameters were added in the hope of obtaining a better fit. However, as more data were obtained, it soon became apparent that the lead Fermi surface was much closer to the free-electron surface than originally thought. The Fourier expansion would require many more terms to satisfactorily describe the sharp corners possible in the nearly-free-electron Fermi surface for a polyvalent metal, and for this reason we have not pursued this approach any further. We may remark, however, that the Fourier expansion method has been used quite successfully by Roaf (ca. 1962) to fit the dHVA results of Shoenberg (ca. 1962) on the noble metals. Here the departure from a free electron surface is somewhat greater than in lead, but there are no sharp corners, and one "sphere"

merges smoothly into the next (Figure 5.1). Even for this simpler surface Roaf used 6 terms in his expansion.

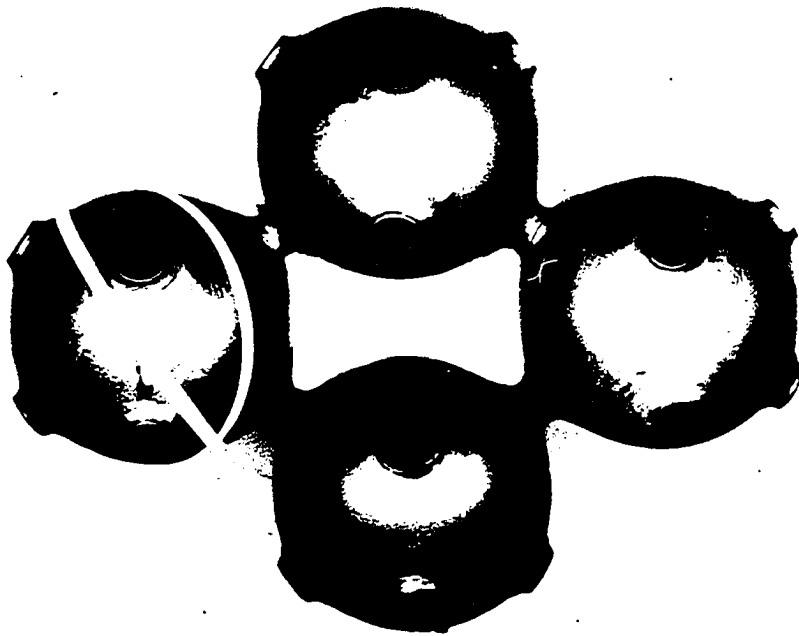
5.3. Orthogonalized-Plane-Wave Method

Cohen¹ suggested that it might be more reasonable to start from a free electron approach and use energy gaps as parameters to fit the Fermi surface. We adopted this suggestion in using the method of Harrison (1960a) which is essentially an interpolation scheme based on the orthogonalized-plane-wave (OPW) approach.

In the OPW method as suggested by Herring (1940) and extended by Phillips and Kleinman (1959, 1960a, 1960b) valence wave functions, i.e. of the conduction electrons, are assumed to resemble symmetrized combinations of plane waves orthogonalized to the ion-core wave functions. Basis functions $\phi_{\mathbf{k}}$ are introduced as the smoothed parts of the orthogonalized plane waves. Due to the orthogonalization procedure the wave equation for the $\phi_{\mathbf{k}}$ contains in addition to the attractive lattice potential, a term with the form of a repulsive potential. Several authors (Phillips and Kleinman 1959, 1960b; Heine 1957b; Harrison 1962) have made calculations showing that there is approximate cancellation between the attractive

¹Cohen, M. H., Institute for the study of Metals, University of Chicago, Chicago 37, Illinois. Fermi surface of lead. Private communication (1961).

Figure 5.1. Fermi surface of copper
(after Shoenberg 1960)



and repulsive potentials in the core region, leaving a small effective pseudopotential. The pseudopotential is actually an integral operator. This repulsive operator is not very sensitive to $\phi_{\mathbf{k}}$ (Phillips and Kleinman 1959) and in many calculations is replaced by a simple analytic function of coordinates $V^D(\mathbf{r})$. Then if $V^D(\mathbf{r})$ is assumed to be small, ordinary perturbation theory can be used to find the basis functions $\phi_{\mathbf{k}}$ (Bassani and Celli 1961). This approach gives a justification for the success which the free-electron model has had in describing the energy bands in metals (Mott and Jones 1958); the actual (uncancelled) atomic potentials are large and if plane waves were chosen from the start, convergence would be extremely slow.

The OPW equations can be written formally in a simple manner following Phillips and Kleinman. We consider a one-electron Hamiltonian

$$H = T + V \quad (5.2)$$

where

$$H \chi_{\underline{\mathbf{k}}} = E_{\underline{\mathbf{k}}} \chi_{\underline{\mathbf{k}}} \quad (5.3)$$

T is the kinetic energy term and V is the potential. (If exchange is included, V will not be a simple function of coordinates.) We assume that core wave functions ψ_c are known and that these wave functions are eigenfunctions of the same

Hamiltonian as the valence wave functions $\chi_{\underline{k}}$. This condition is important in order to obtain the best convergence (Phillips and Kleinman 1959).

The solutions of Equation 5.3 are assumed to take the form

$$\chi_{\underline{k}} = \theta_{\underline{k}} - \sum_c (\psi_c | \theta_{\underline{k}}) \psi_c . \quad (5.4)$$

Here the $\chi_{\underline{k}}$ are constructed to be orthogonal to the core states and the $\theta_{\underline{k}}$ are assumed to be the remaining smooth part of $\chi_{\underline{k}}$. The core wave functions satisfy the equation

$$H \psi_c = E_c \psi_c . \quad (5.5)$$

Substituting Equation 5.4 into Equation 5.3, we obtain:

$$T \theta_{\underline{k}} + (V + V^r) \theta_{\underline{k}} = E_{\underline{k}} \theta_{\underline{k}} \quad (5.6)$$

where

$$V^r \theta_{\underline{k}} = - \sum_c (E_c - E_{\underline{k}}) (\psi_c | \theta_{\underline{k}}) \psi_c . \quad (5.7)$$

V^r is an operator corresponding to the repulsive term in the pseudopotential, $V^D = V + V^r$. Now we assume $\chi_{\underline{k}}$ can be expanded in a complete set of functions orthogonalized to the core functions. That is, let

$$\chi_{\underline{k}} = \sum_{\underline{K}} C_{\underline{k}}^{\underline{K}} \psi_{\underline{k}}^{\underline{K}}$$

and

$$(5.8)$$

$$\theta_{\underline{k}} = \sum_{\underline{K}} c_{\underline{k}}^{\underline{K}} \phi_{\underline{k}}^{\underline{K}},$$

where

$$\psi_{\underline{k}}^{\underline{K}} = \phi_{\underline{k}}^{\underline{K}} - \sum_c (\psi_c | \phi_{\underline{k}}^{\underline{K}}) \psi_c, \quad (5.9)$$

and we assume that the $\phi_{\underline{k}}^{\underline{K}}$ are smooth functions.¹

If we multiply Equation 5.6 by $\psi_{\underline{k}}^{\underline{K}'}$ and integrate, we obtain:

$$(\psi_{\underline{k}}^{\underline{K}'} | T + V^p | \theta_{\underline{k}}) = E_{\underline{k}} (\psi_{\underline{k}}^{\underline{K}'} | \phi_{\underline{k}}^{\underline{K}'}). \quad (5.10)$$

Substituting Equation 5.8 into Equation 5.10, we find

$$\sum_{\underline{K}} c_{\underline{k}}^{\underline{K}} (T_{\underline{k}}^{\underline{K}} + V_{\underline{k}}^{p\underline{K}}) = E_{\underline{k}} c_{\underline{k}}^{\underline{K}'}, \quad (5.11)$$

where

$$T_{\underline{k}}^{\underline{K}} + V_{\underline{k}}^{p\underline{K}} = (\phi_{\underline{k}}^{\underline{K}'} | T + V^p | \phi_{\underline{k}}^{\underline{K}}). \quad (5.12)$$

We now assume that the $\phi_{\underline{k}}^{\underline{K}}$ are plane waves $\frac{1}{\sqrt{V}} e^{i(\underline{k} + \underline{K}) \cdot \underline{r}}$

(that is, the $\psi_{\underline{k}}^{\underline{K}}$ are OPW's) and that $T_{\underline{k}}^{\underline{K}}$ is the free electron kinetic energy, proportional to $|\underline{k} + \underline{K}|^2$ for $\underline{K} = \underline{K}'$ and 0 for $\underline{K} \neq \underline{K}'$. We also assume V^p is small and can be replaced by a

¹We note that if the $\phi_{\underline{k}}^{\underline{K}}$ are chosen as plane waves, the $\psi_{\underline{k}}^{\underline{K}}$ will not be orthogonal.

simple function of coordinates (Phillips and Kleinman 1959).

If we expand V^D in a Fourier series

$$V^D = \sum_{\underline{K}} V_{\underline{K}} e^{i\underline{K} \cdot \underline{r}} , \quad (5.13)$$

Equation 5.11 becomes

$$T[\underline{k} + \underline{K}'] C_{\underline{k}}^{\underline{K}'} + \sum_{\underline{K}} C_{\underline{k}}^{\underline{K}} V_{\underline{K} - \underline{K}'} = E_{\underline{k}} C_{\underline{k}}^{\underline{K}'} . \quad (5.14)$$

For the interpolation scheme used here we assume that the higher Fourier components of the repulsive and attractive potentials cancel exactly and that only a few low Fourier components need be used to fit the experimental results. Then the eigenvalues of Equation 5.14 are found by solving determinants of low order. $V_{\underline{K}'\underline{K}}^{D\underline{k}}$ is assumed to depend only on the wave number difference $\underline{K} - \underline{K}'$, whereas, in fact, these Fourier coefficients also depend upon the individual state wave-vectors \underline{k} , since the potential is a non-local operator. That is, the matrix elements $V_{\underline{K}'\underline{K}}^{D\underline{k}}$ vary somewhat over the Brillouin zone face. Harrison (1962) and Ham (1960, p.23) have noted variations of a few hundredths of a Rydberg in aluminum, magnesium, and the alkali metals. Harrison¹ has calculated matrix elements for zinc for \underline{K} parallel to \underline{k} , \underline{K} parallel to $-\underline{k}$, and \underline{K}

¹Harrison, W. A., General Electric Research Laboratory, Schenectady, New York. Matrix elements in zinc. Private communication (1962).

perpendicular to \underline{k} using the OPW method. The results are shown in Figure 5.2. We see that the curves do not coincide and the matrix elements for any particular \underline{k} may differ by as much as 0.1 ry. However, in our calculation \underline{k} does not vary greatly over the region of interpolation. For example, in the expansion about U (Section 5.3) the vector \underline{k} rotates thru an angle of only about 20° and has about a 30% change in magnitude. Therefore, for the purpose of describing the Fermi surface we assume the matrix elements $V_{\underline{K}'\underline{K}}^{p\underline{k}}$ are constants, $V_{\underline{K}'-\underline{K}}$. With these approximations, Equation 5.14 becomes a system of equations of the same form as for the nearly-free-electron approximation.

The $V_{\underline{K}'-\underline{K}}$ are adjustable parameters determined from the experimental results in the following manner. A symmetry point on the Brillouin zone such as U or W (Figure 4.1) is chosen. An OPW with wave vector \underline{k} at this symmetry point is degenerate with n other OPW's (at W there are a total of 4 and at K a total of 3) with wave vectors related to \underline{k} by reciprocal lattice vectors \underline{K}_i ($i = 1, 2, \dots, n$). This number determines the rank of the Hamiltonian matrix considered in finding the energy levels and mixing with all other states is neglected. An OPW with wave vector \underline{k} in the vicinity of the symmetry point has approximately the same energy as OPW's related by the same \underline{K}_i as above. Therefore, a secular determinant can be written for an OPW with wave vector \underline{k} and the n OPW's with

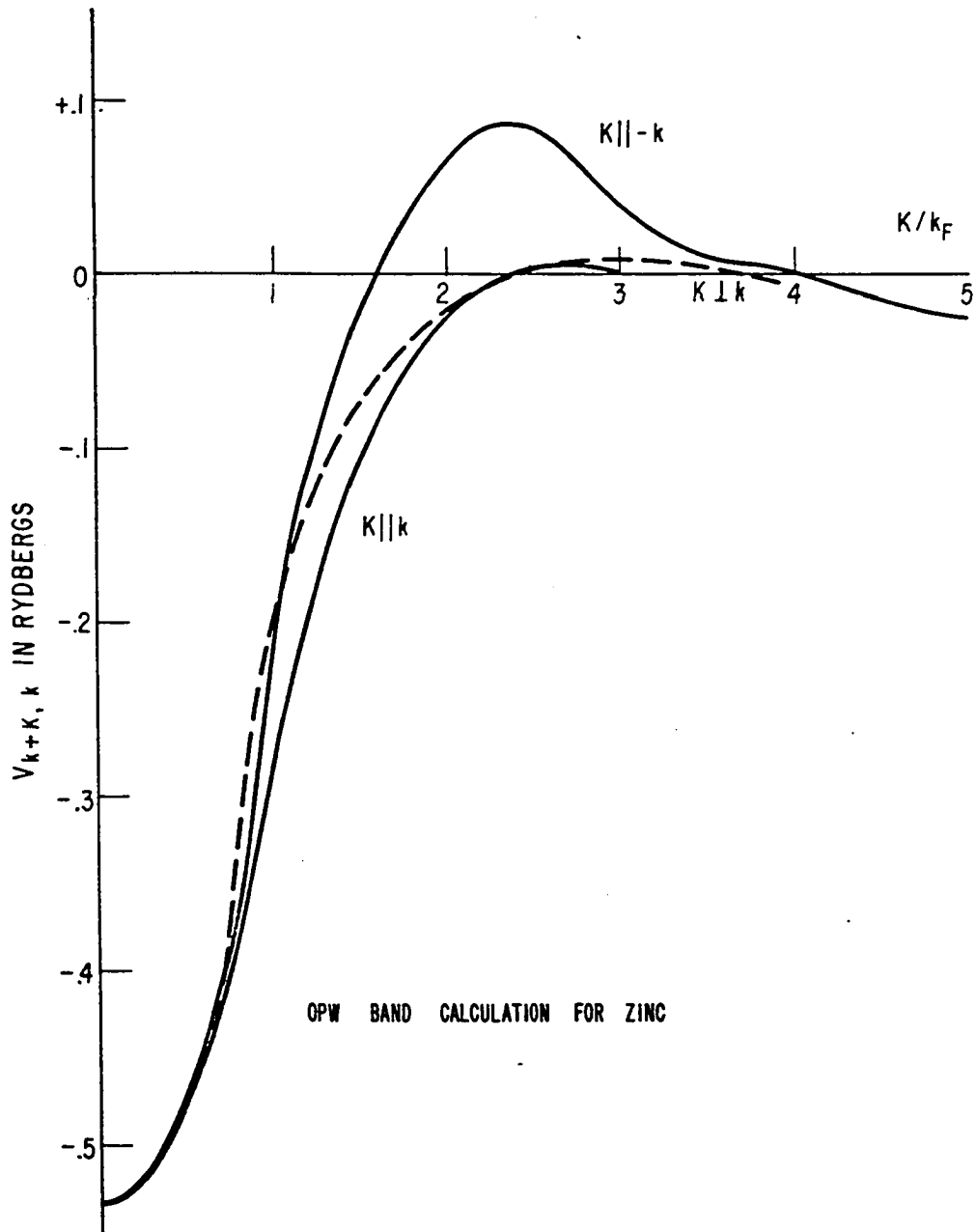


Figure 5.2. OPW matrix elements in zinc

wave vectors $\underline{k}-\underline{K}_i$ ($i = 1, \dots, n$). For fixed energy E the resulting secular equation can be solved for the values of \underline{k} giving the constant energy surfaces about the symmetry point. The $V_{\underline{K}'-\underline{K}}$ are chosen by adjusting calculated cross-sectional areas of the Fermi surface to agree with dHvA data. The details of this procedure will be discussed more completely in the next section.

5.4. Determination of the Fermi Surface

Harrison (1960a) has used the OPW interpolation scheme with the energy levels from Heine's band calculation (1957c) to describe the Fermi surface of aluminum. Heine's values for the energy levels at symmetry points of the Brillouin zone were used to determine two Fourier components of the pseudopotential. With these Fourier coefficients, Harrison determined the constant energy curves in the neighborhood of the Fermi surface.

For lead we are not as fortunate, since no band calculation has yet been made although such a calculation should be possible since self-consistent atomic wave functions are now available (Herman and Skillman 1962). Instead we use the experimental areas to determine the Fourier components; the areas were selected as follows:

- a. The areas were required to be small areas about symmetry points in order to use analytic expansions and thus

avoid graphical interpolation. This requirement restricts us to considering small orbits on the third-zone surface since the extremal orbits in the second zone are very large.

b. Two areas are required since two matrix elements, V_{111} and V_{200} , are needed in order to remove the free-electron degeneracy along the line U - W; the third-zone surface is 'centered' on such a line.

c. The areas should be associated with accurately known dHvA periods.

The above requirements restricted us to the use of the orbit about U (ζ) and the orbit about W (ν) with the enclosed areas given in Table 4.1. The orbit about X (ξ) might have been chosen, but the accuracy would have been poorer and graphical methods would probably have been required in order to find the area enclosed.

We begin by considering the expansion related to the $[110]$ area A_{ζ} around the point U. An OPW of wave number $\underline{k}_1 = (1/4 + k_x, 1/4 + k_y, 1 + k_z)$ in the vicinity of U has matrix elements connecting it with two other OPW's with wave numbers $\underline{k}_2 = \underline{k}_1 - (0, 0, 2)$ and $\underline{k}_3 = \underline{k}_1 - (1, 1, 1)$.¹ All three OPW's have nearly the same energy (for $k_x = k_y = k_z = 0$ the energies would be the same) so that if mixing with other states is neglected the Hamiltonian matrix corresponding to

¹All wave vectors will be given in units of $2\pi/a$ measured from Γ , where a is the lattice constant.

Equation 5.14 can be written

$$H = \begin{pmatrix} T(\underline{k}_1) & V_{200} & V_{111} \\ V_{200} & T(\underline{k}_2) & V_{111} \\ V_{111} & V_{111} & T(\underline{k}_3) \end{pmatrix} \quad (5.15)$$

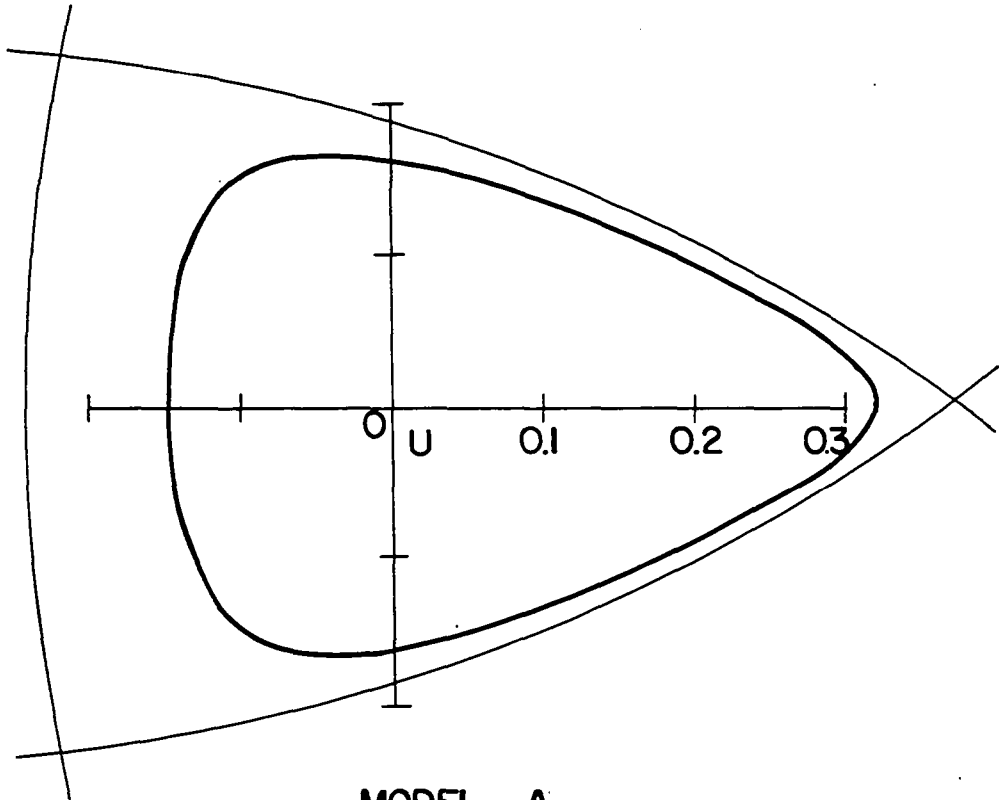
From symmetry V_{111} and V_{200} are real. $T(\underline{k})$ is the kinetic energy term which we write as $T(\underline{k}) = \hbar^2 k^2 / 2m^*$ where $\hbar^2 / 2m^*$ may be regarded as an energy scaling factor which can be divided out of all the matrix elements. Then the fitting is independent of this quantity. We stress this point because of the discrepancies of a factor of 2 to 3 between the observed cyclotron masses and the masses predicted by the single OPW model.

Thus following Harrison (1960c, p. 33), we assume that effects such as electron-electron interactions and electron-phonon interactions do not modify the geometrical properties of the Fermi surface, but only change the velocities and relaxation times of an electron near this surface. In what follows we use the free-electron mass m for the scaling factor and assume the mass discrepancies can be accounted for by inclusion of electron interactions. Cyclotron masses will be discussed in Chapter 6.

In order to find the constant energy surfaces, the energy E is fixed as an eigenvalue in Equation 5.15 and the values of

k_x , k_y , and k_z are found that satisfy the secular equation for assumed values of the parameters V_{111} and V_{200} . The resulting function of k_x , k_y , k_z and E describes the constant energy surfaces around the symmetry point U. In particular, E is set equal to the free electron Fermi energy, $E_F = 0.70$ ry, in order to determine the equation of the Fermi surface near U. Introduction of the matrix elements produces a small change in E_F , but this change should have negligible effect upon the shapes of the constant energy curves and is therefore neglected (Appendix A).

The intersections of the Fermi surface with symmetry planes are found by eliminating one of the coordinates. When we set $k_x = -k_y = k$, i.e. for the $\{110\}$ sections, the secular equation obtained from the Hamiltonian (5.15) reduces to a cubic equation for k_z^2 as a function of k and the solution of this equation is discussed in Appendix A. One set of solutions (k, k_z) describes the (110) cross-section through the center of an arm in the third band (orbit ζ) and another set determines part of the second band hole surface. The area of the ζ cross-section was compared with the observed area and the parameters V_{111} and V_{200} were varied until agreement was found. Figure 5.3 shows this extremal cross-section for one set of the parameters, V_{111} and V_{200} , along with the simple OPW surface for comparison. Figure 5.4 and Figure 5.5 show this area as a function of the parameters V_{111} and V_{200} . It



MODEL A
ZONE 3 [110] ORBIT ζ
(γ -OSCILLATIONS)

Figure 5.3. Orbit ζ

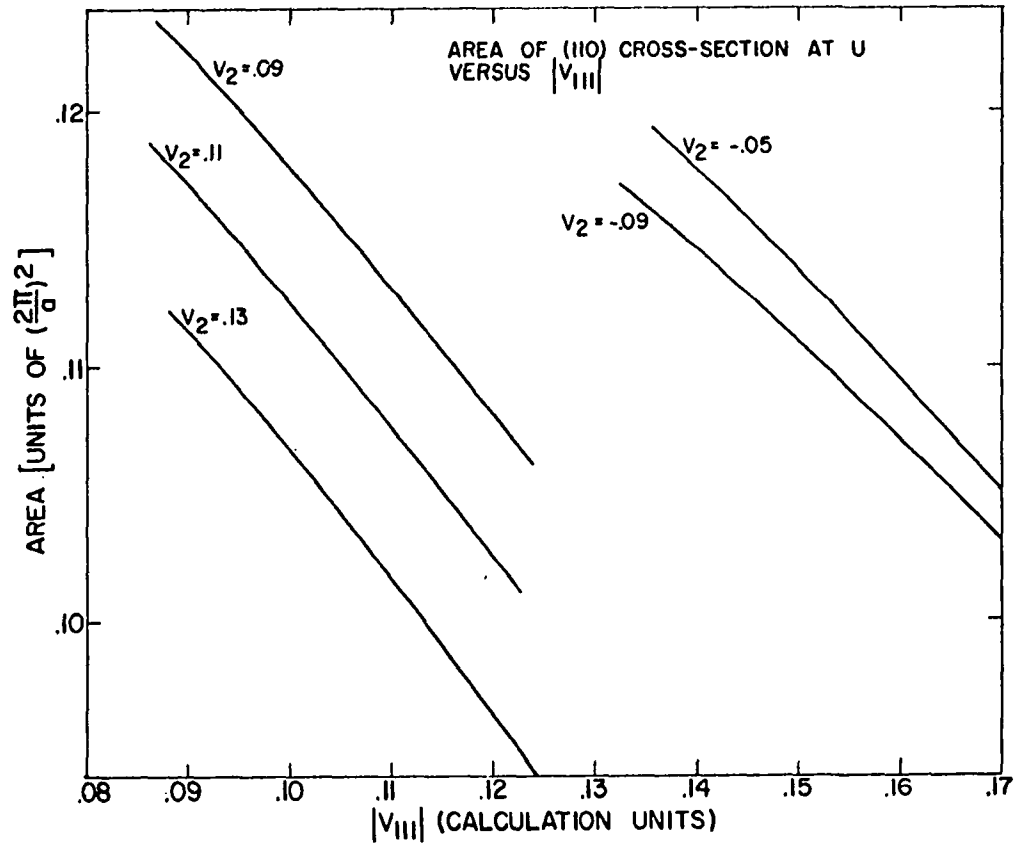


Figure 5.4. \star_c versus v_{111} ($v_2 = v_{200}$)

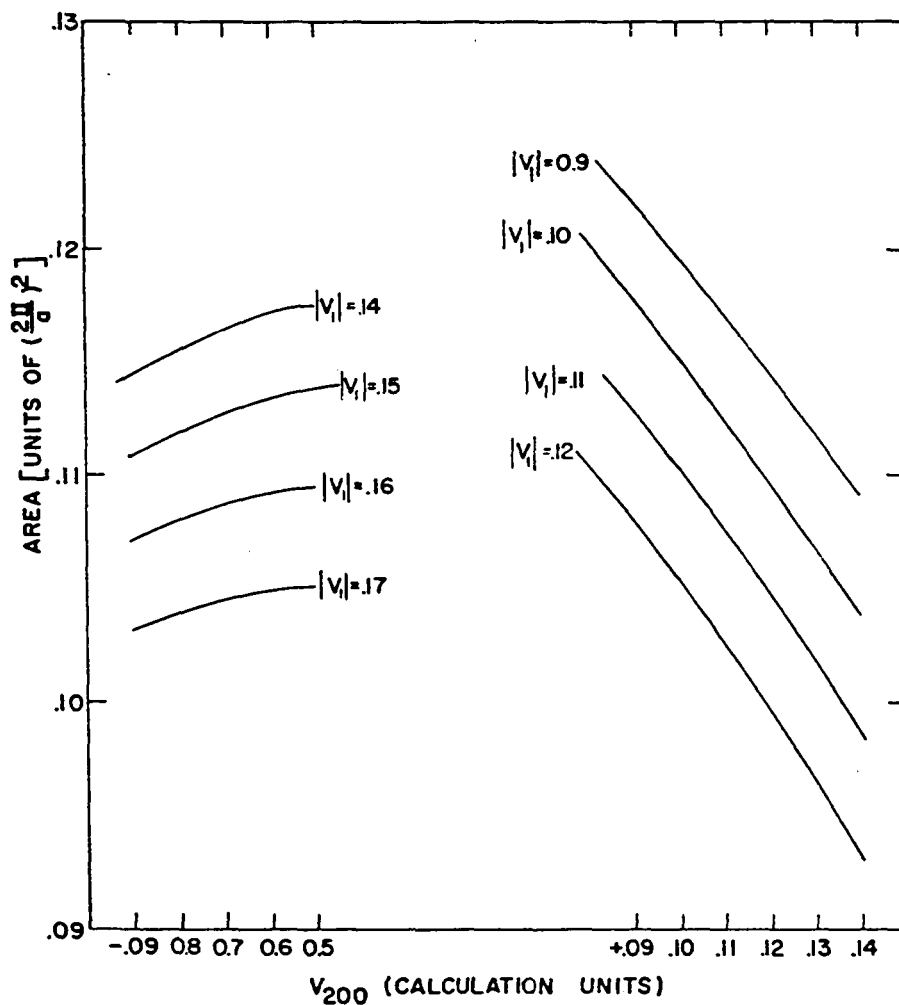


Figure 5.5. A_c versus V_{200} ($V_1 = V_{111}$)

turns out that the results depend only on the magnitude of V_{111} . The values of V_{111} and V_{200} are given in calculation units (CU) where 1 CU = 0.454 ry.

A similar expansion in (110) planes can be made about any point P on the line U - W (Figure 4.1) by replacing E by $E' = E - 2\gamma^2$ in the secular equation obtained from Equation 5.15. Here $\sqrt{2}\gamma$ is the distance along the line U - W measured from U. $\gamma = 0$ at U and $\gamma = 0.25$ at W. In this manner the shape of the entire arm can be determined within the limitation that only three OPW's are used. As γ approaches 0.25 the addition of a fourth OPW becomes necessary. In order to take this into account in an approximate manner $E(\underline{k})$ has been calculated for the symmetry line U - W for four OPW's (Appendix A). These results have then been used to correct the values chosen for E' based upon three OPW's. (Each band is corrected separately as described in the appendix.)

Around W a similar expansion was made using four OPW's with wave vectors $\underline{k}_1 = (1/2 + k_x, k_y, 1 + k_z)$, $\underline{k}_2 = \underline{k}_1 - (2, 0, 0)$, $\underline{k}_3 = \underline{k}_1 - (1, 1, 1)$, and $\underline{k}_4 = \underline{k}_1 - (1, 1, 1)$. These four states have nearly equal energies (for $k_x = k_y = k_z$ the energies are equal) and the Hamiltonian in this case becomes

$$H = \begin{pmatrix} T(k_1) & V_{200} & V_{111} & V_{111} \\ V_{200} & T(k_2) & V_{111} & V_{111} \\ V_{111} & V_{111} & T(k_3) & V_{200} \\ V_{111} & V_{111} & V_{200} & T(k_4) \end{pmatrix} \quad (5.16)$$

if mixing with other states is neglected.

In accordance with the discussion in Section 5.3, we assume V_{111} and V_{200} have the same values as in the Hamiltonian (5.15). The solutions of the secular equation resulting from Equation 5.16 are discussed in Appendix B.

The windmill orbit ν in a plane normal to $[100]$ (Figure 4.4) was obtained by setting $k_x = 0$ and solving the resulting quartic equation for k_z as a function of k_y for different values of V_{111} and V_{200} . One set of solutions determines the windmill orbit and the area enclosed is compared with A_ν . Figure 5.6 shows this windmill orbit ν calculated for two sets of the parameters, V_{111} and V_{200} . Figures 5.7 and 5.8 show the area of orbit ν as a function of V_{111} and V_{200} .

Values of the parameters were selected so that the calculated cross-sectional area enclosed by orbit ζ normal to $[110]$ equaled the area A_ζ and the area of the windmill orbit ν about W normal to $[100]$ equaled the area A_ν . The parameters V_{111} and V_{200} are not fixed uniquely in this manner since two sets can be found to fit the experimental areas, a

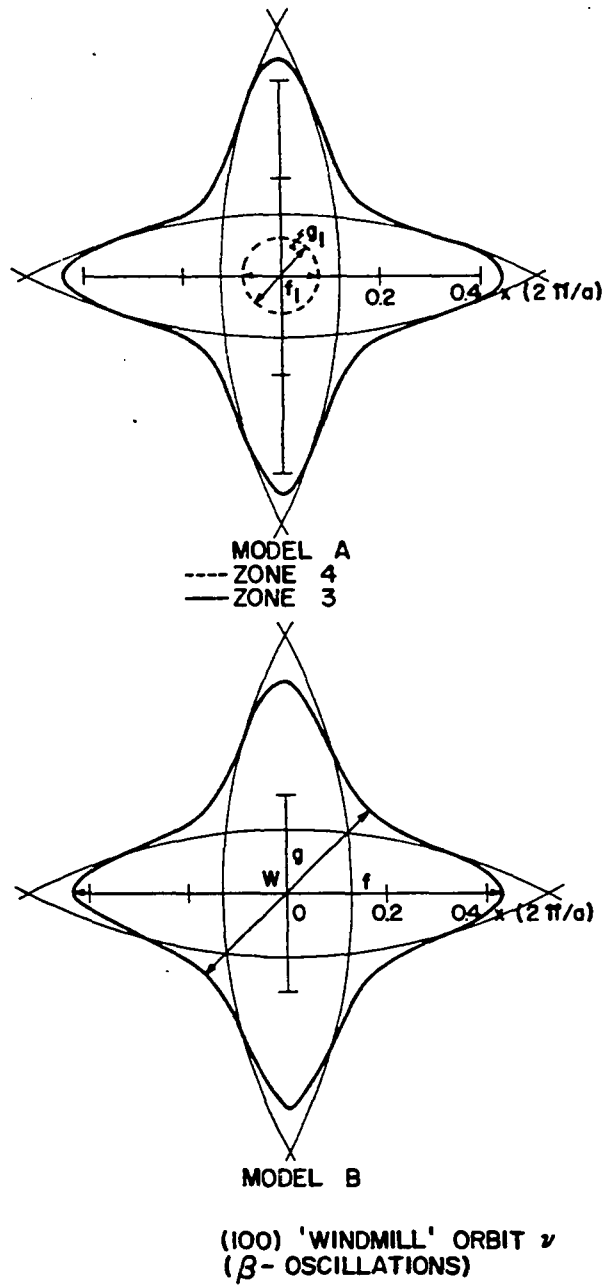


Figure 5.6. 'Windmill' orbit ν

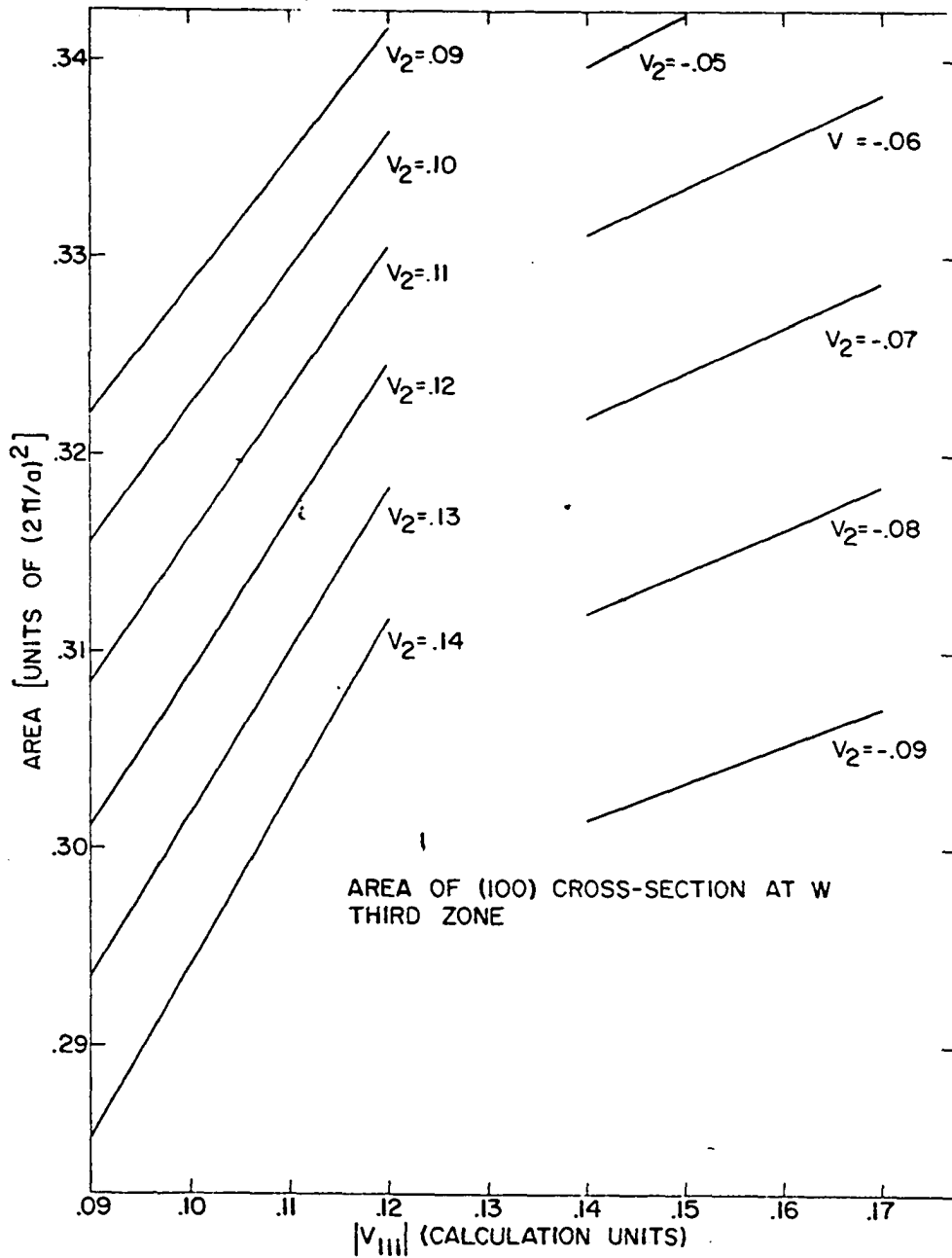


Figure 5.7. A_v versus V_{111} ($V_2 = V_{200}$)

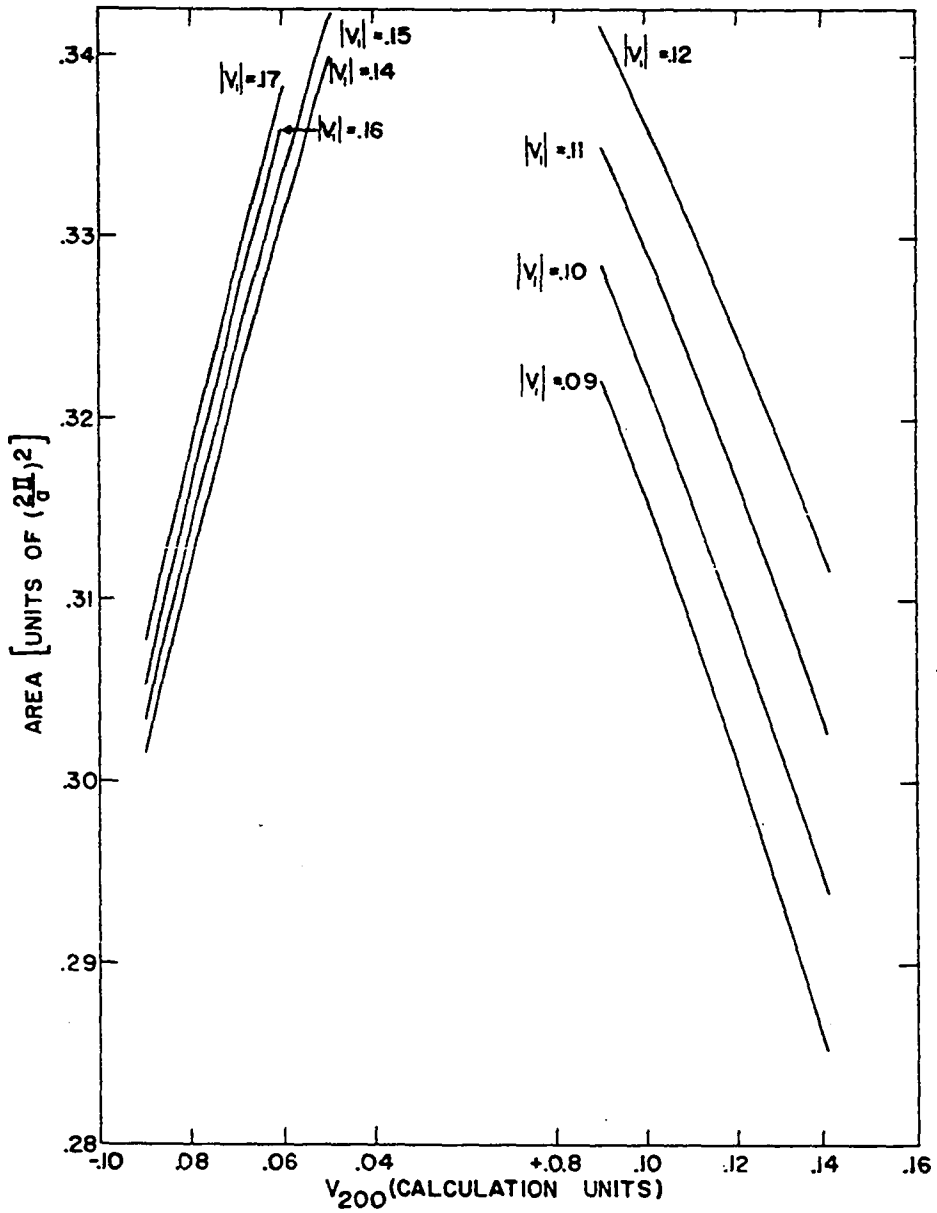


Figure 5.8. $\star v$ versus V_{200} ($v_1 = v_{111}$)

set with $V_{200} > 0$ and a set with $V_{200} < 0$. Since V_{111} enters the equations only as V_{111}^2 , its sign is undetermined, but its magnitude depends on which of the two values of V_{200} is chosen.

The values of the parameters were found to be:

$$\text{Model A} - |V_{111}| = 0.069 \text{ ry}, \quad V_{200} = -0.039 \text{ ry}$$

$$\text{Model B} - |V_{111}| = 0.045 \text{ ry}, \quad V_{200} = 0.052 \text{ ry}.$$

At this point it is impossible to choose one model over the other.

Within the framework of our particular OPW model the parameters V_{111} and V_{200} are determined to about 6%. This estimate incorporates the uncertainties in the dHvA periods; in general a 1% change in an experimental area would result in a change of between 2% and 4% in the matrix elements. The 6% uncertainty also allows for small errors in calculating the areas (usually less than 1%) as well as the possibility of relaxing the fitting conditions slightly to obtain better agreement with other dHvA areas (Chapter 6). For model B above the values were given for relaxed fitting conditions, and the values for more exact fitting of A_{ζ} and A_{ν} are $|V_{111}| = 0.046 \text{ ry}$ and $V_{200} = 0.054 \text{ ry}$.

An estimate of the errors involved in the model itself is much more difficult. The decrease in the Fermi energy due to the introduction of the lattice potential might require a

change in the parameters of possibly 20%, but, as we noted before, this has little effect upon the shape of the Fermi surface. In addition the use of different numbers of OPW's at different points in the Brillouin zone might cause an error of roughly 10% in the matrix elements. (This estimate is suggested from the comparison of the 3 OPW results with the 4 OPW results at point U in the Brillouin zone (Appendix A).) No attempt will be made here to estimate errors caused by neglect of the variation of the matrix elements throughout the Brillouin zone (Section 5.3) and the omission of any higher Fourier components of the pseudopotential.

Harrison¹ has plotted the matrix elements from band calculations for several different elements on one graph shown in Figure 5.9. Some preliminary results from a band calculation for tin have been included² and the two sets of values for lead have been added using the minus sign for V_{111} . Either set appears consistent with the general trend of the results for other elements if the minus sign is chosen. (A detailed band calculation would be necessary to determine the sign of V_{111} .)

¹Harrison, W. A., General Electric Research Laboratory, Schenectady, New York. Matrix elements from band calculations. Private communication (1962).

²Miasek, M., Department of Physics and Astronomy, University of Rochester, Rochester 20, New York. Band structure of tin. Private communication (1962).

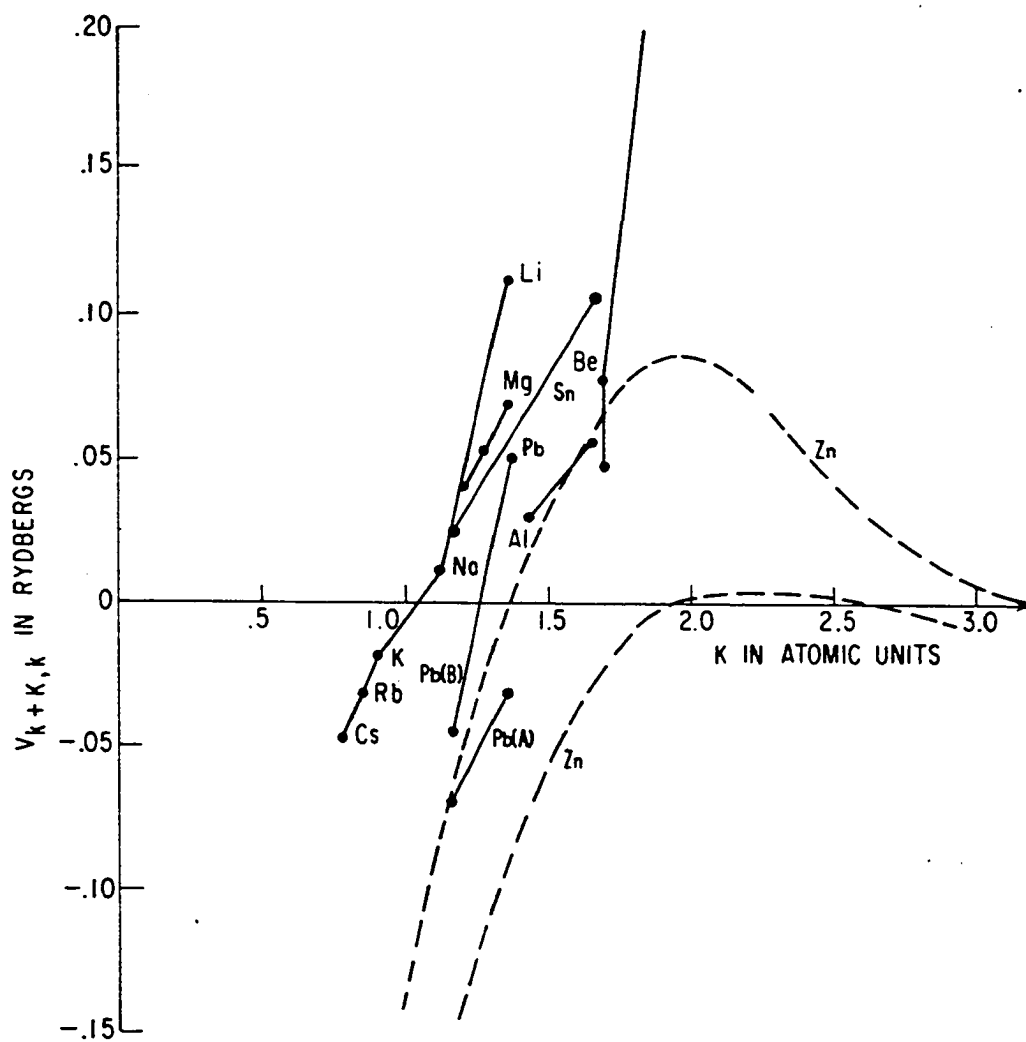


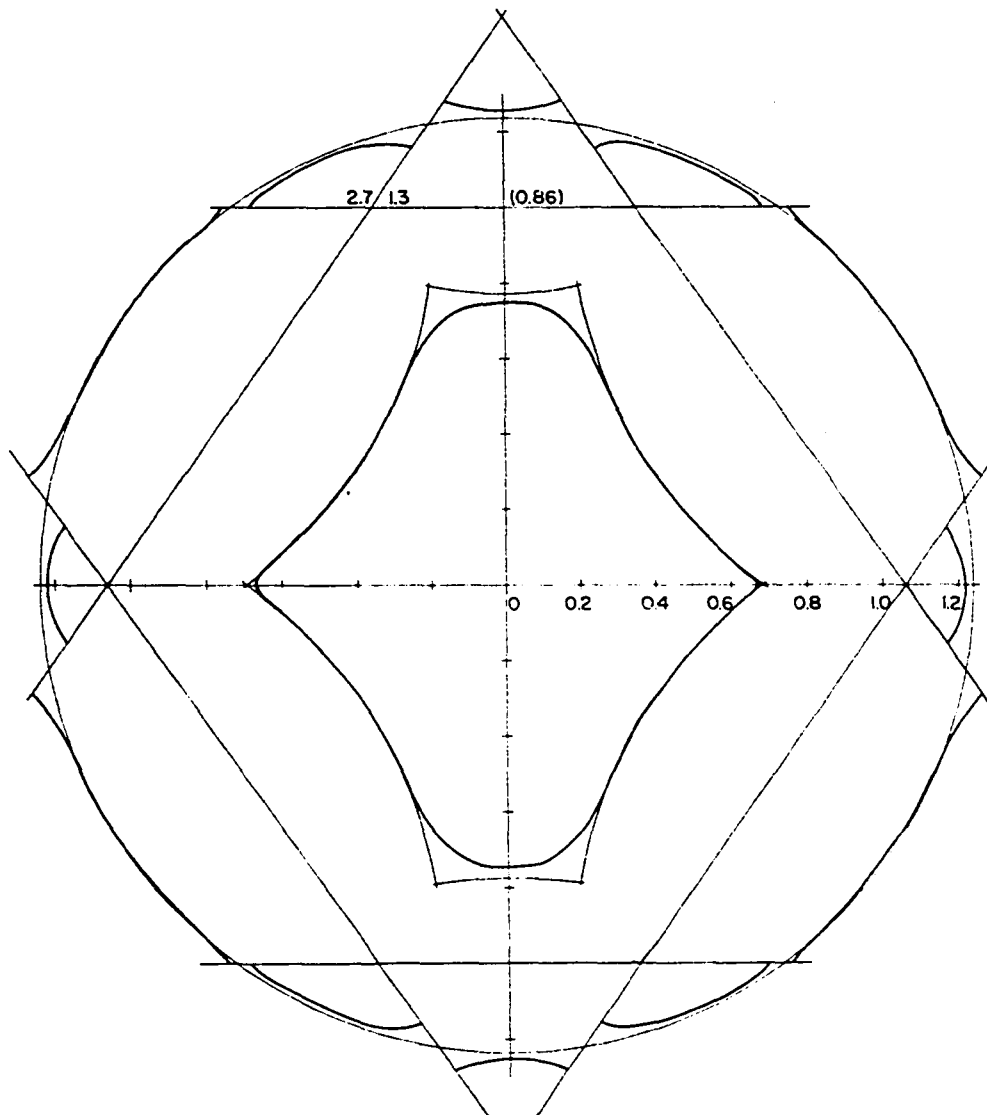
Figure 5.9. Matrix elements versus K for different metals

After V_{111} and V_{200} had been selected, the results from the computer calculations described in Appendices A and B were used to determine parts of both the second-band and third-band Fermi surface near the line U - W. These results were graphically extended and connected smoothly in order to describe the entire Fermi surface.

Figure 5.10 shows the modification of the free-electron sphere by the lattice potential for a (110) cross-section through Γ . The main changes occur near intersections of the sphere with Bragg planes. (The second-band hole surface has been remapped and is drawn inside the fundamental zone. This surface is changed from the single OPW surface by only a slight rounding at the corners.)

Although the values chosen for the Fourier components may have little significance away from the Fermi surface, a few $E(\underline{k})$ curves (Figures 5.11 and 5.12) have been drawn along symmetry directions for models A and B. First we point out that for calculations along $\Gamma - X$ (Δ) and $\Gamma - L$ (Λ) only two OPW's and consequently one matrix element were used. The curves were adjusted to fit at X and L, respectively, and slight discrepancies resulting from the use of only two OPW's may be noted at Γ . Similarly along $\Gamma - U$ only three OPW's were used and again a discrepancy (in this case rather small) is seen at Γ .

We may also remark that the shapes of the $E(\underline{k})$ curves in



CENTRAL 110 SECTION SHOWING MODIFICATION OF FREE-ELECTRON
 SPHERE BY LATTICE POTENTIAL (EXTENDED ZONE SCHEME)
 $[V_{111}] = 0.070 \text{ ry}$, $V_{200} = -0.032 \text{ ry}$

INSERT: 2nd ZONE HOLE SURFACE (REDUCED ZONE SCHEME)

Figure 5.10. Modification of the free-electron sphere by the lattice potential for a (110) cross-section through Γ

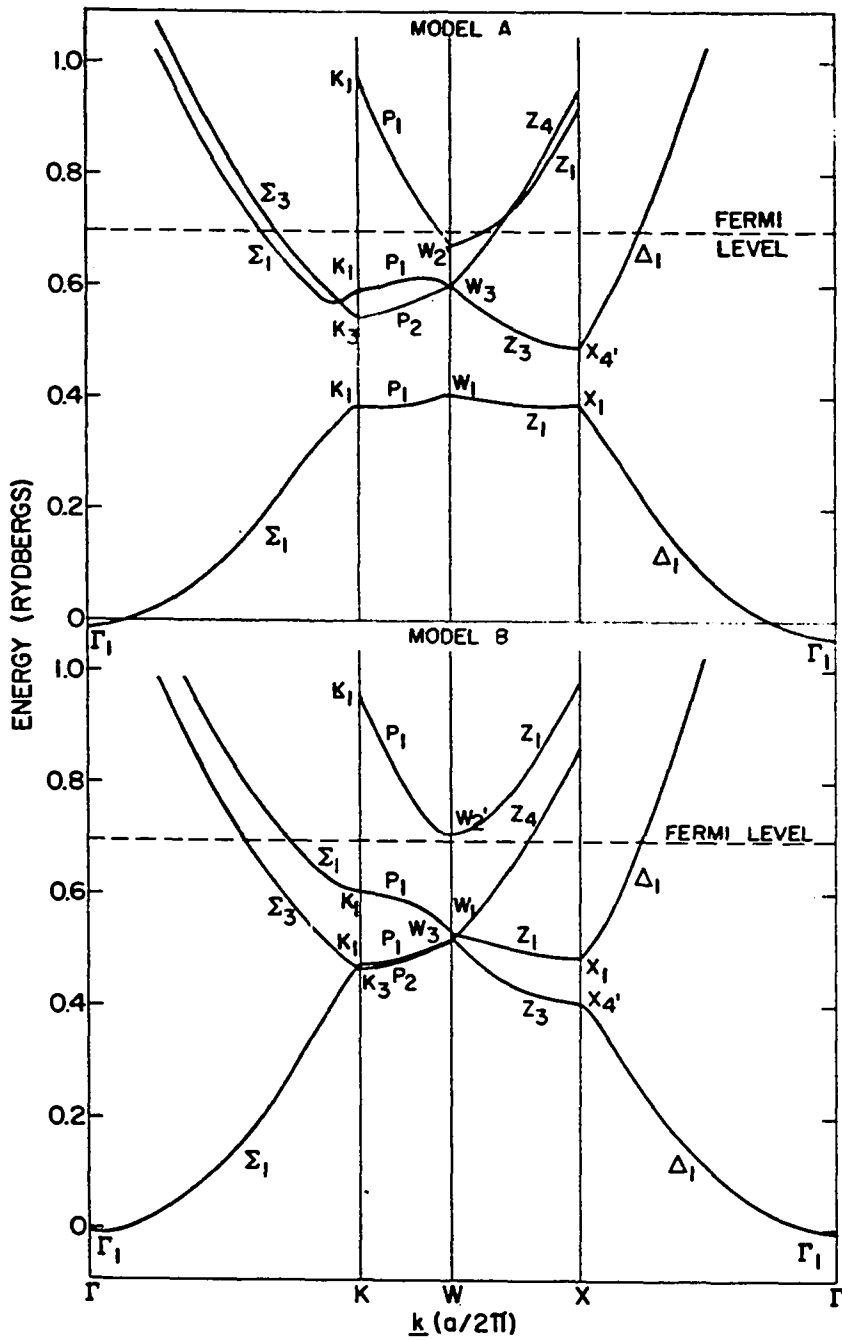


Figure 5.11. $E(\underline{k})$ along symmetry lines

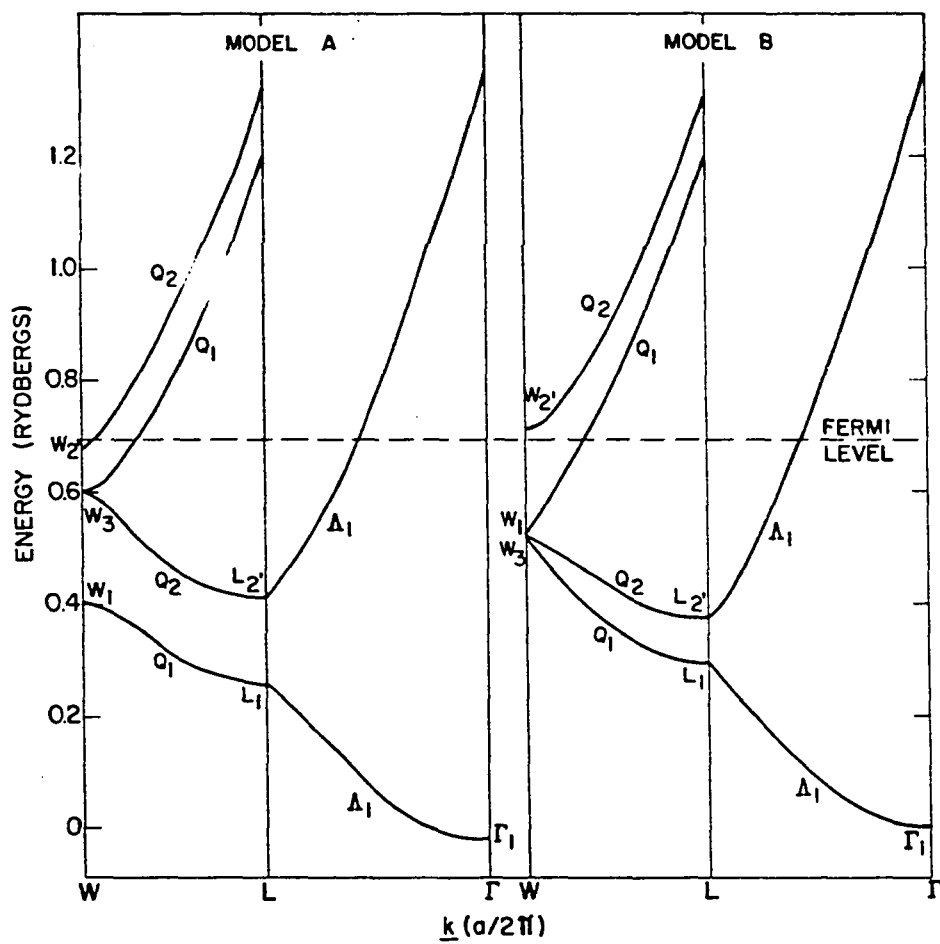


Figure 5.12. $E(\underline{k})$ along symmetry lines

Figures 5.11 and 5.12 are independent of the sign of V_{111} . However, we have assumed that V_{111} is negative in labeling the energy levels. (The notation of Bouckaert et al. (1936) has been followed as far as possible; the subscript 1 always refers to the state transforming according to the identity representation.) As a result W'_2 is higher in energy than W_1 . (The symmetry of W'_2 is fundamentally p-type while that of W_1 is s-type.) If V_{111} were positive, W_1 and W'_2 would be interchanged with corresponding changes in labeling for the remainder of the energy-level diagram.

Figures 5.11 and 5.12 point out some differences between model A and model B:

For model A a band with predominately s-type symmetry is lowest with a gap between this and the next band of roughly 0.1 ry. This next highest band is mainly p-type and crosses a third band along the line $\Gamma - U$. These two bands are degenerate at W. The Fermi level is also higher than a fourth band which has p-type symmetry at W. Thus model A suggests the existence of small pockets of electrons in the fourth band near W.

For model B the lowest band is essentially p-type and the first and second bands are nearly degenerate, especially along W - U. The highest level at W is again p-type and non-degenerate. We note that the fourth band is empty for model B.

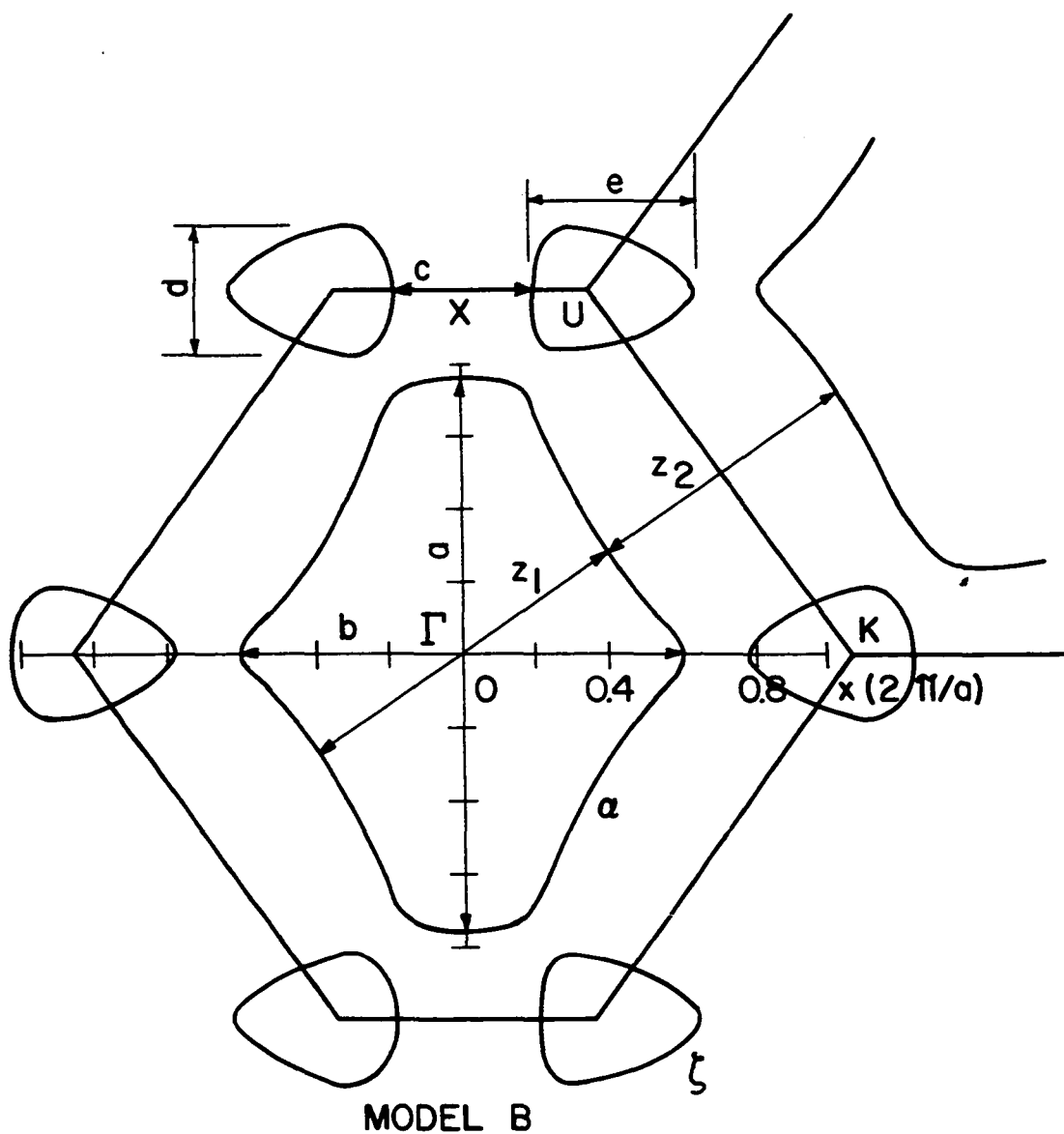
6. COMPARISON OF EXPERIMENTAL AND CALCULATED RESULTS

6.1. dHvA Effect

6.1.1. Extremal areas at symmetry directions

In Chapter 5 we determined two sets of Fourier coefficients of the pseudopotential arising in the two OPW models, A and B. With these coefficients it was possible to determine the intersections of the Fermi surface with various symmetry planes. Figures 6.1 - 6.5 show such extremal sections for the remapped second- and third-zone surfaces. In some cases the results for both models are so similar that only one is shown. Figure 6.1 shows both the second-band and third-band surfaces for a (110) section through Γ . This figure is a remapping of the modified free-electron surface shown in Figure 5.10. Figure 6.2 shows the dogbone-shaped orbit μ for a (110) section through W. The orbit bounding the hole surface for a (100) section (Figure 6.3) runs along sharp ridges in the single OPW model. The addition of lattice potentials rounds off these sharp corners, and thus produces a considerable reduction in the enclosed area.

From drawings such as those in Figures 6.1 - 6.5 it was possible to use a planimeter to determine the cross-sectional areas enclosed by the orbits. The planimeter was used for all areas except those enclosed by the $[110]$ orbits ζ and ω and

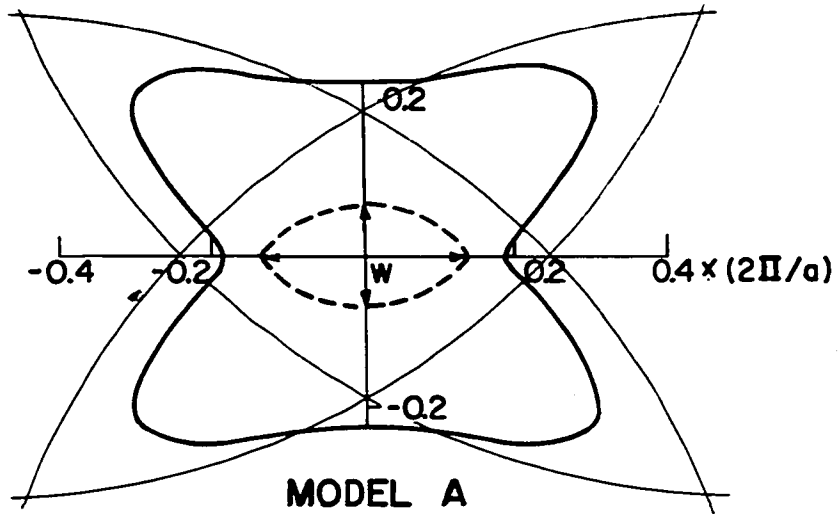


MODEL B

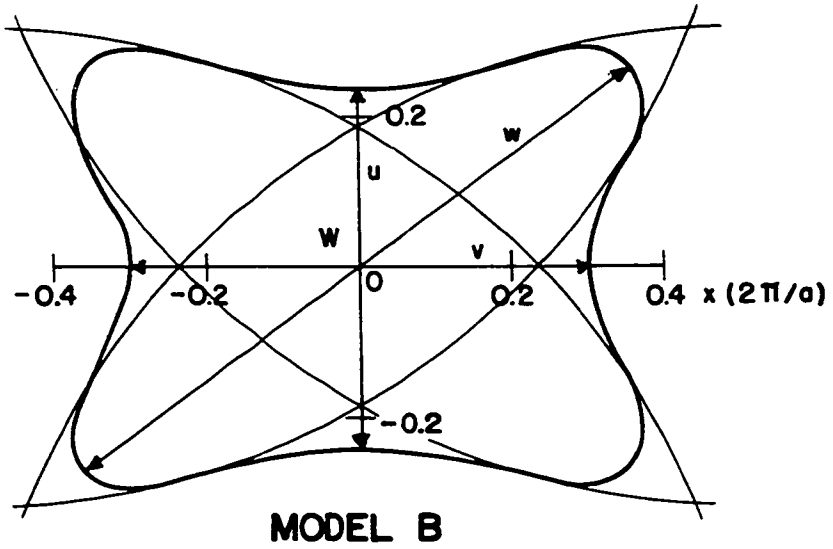
ZONE 2 $[\text{110}]$ α ORBIT (α -OSCILLATION)

ZONE 3 $[\text{110}]$ ζ ORBIT (γ -OSCILLATION)

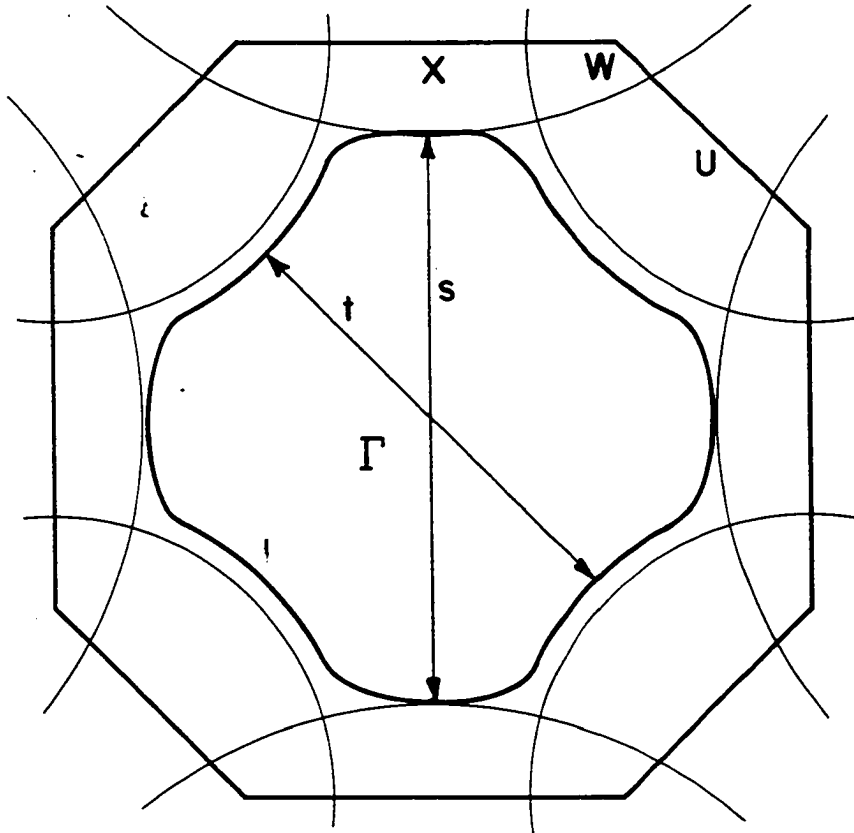
Figure 6.1. Second-band and third-band Fermi surfaces for a (110) section through Γ



--- ZONE 4
 — ZONE 3

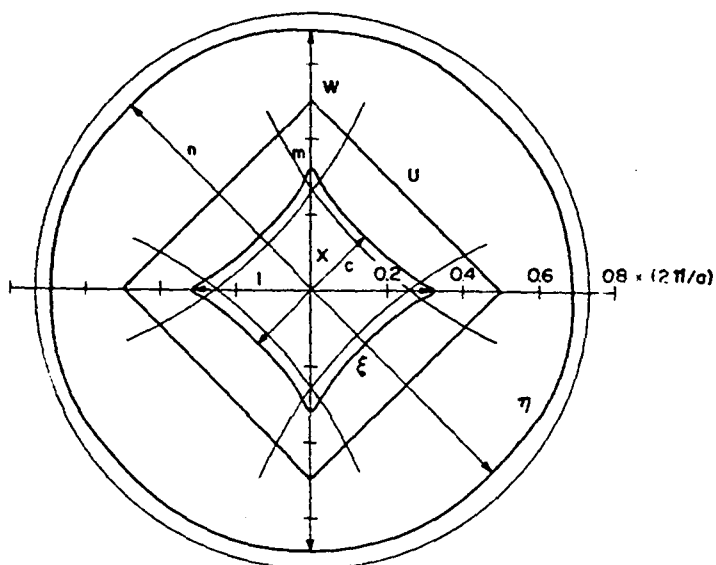


[110] 'DOG BONE' ORBIT ω
 (μ OSCILLATIONS)
 Figure 6.2. Third-band orbit ω

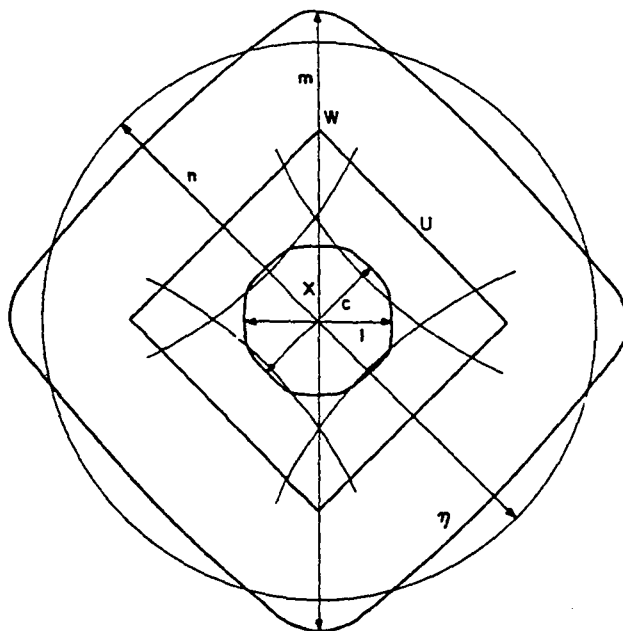


MODEL B
ZONE 2
[100] HOLE SURFACE
(α OSCILLATIONS)

Figure 6.3. Hole surface for a (100) section through Γ

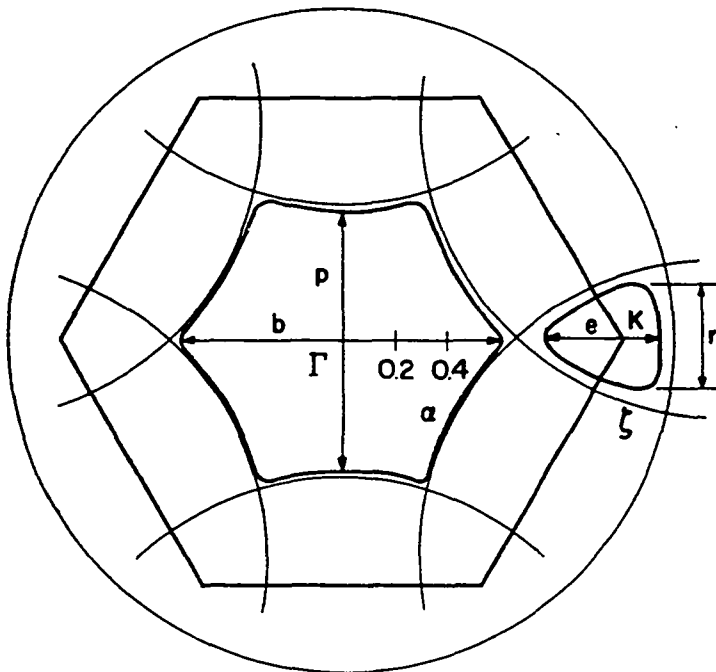


MODEL A
ZONE 3
[100] ORBITS ξ AND η
(γ OSCILLATIONS)

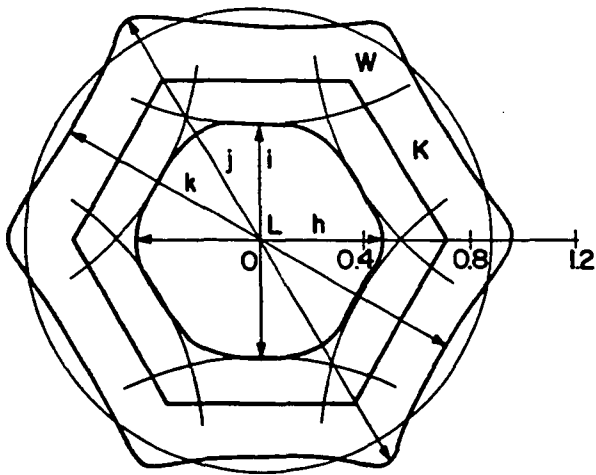


MODEL B
ZONE 3
[100] ORBITS ξ AND η
(γ OSCILLATIONS)

Figure 6.4. Third-band orbits ξ and η



MODEL B
 ZONE 2 [111] ORBIT α (α -OSCILLATIONS)
 ZONE 3 [111] ORBIT ζ (γ -OSCILLATIONS)



MODEL A
 ZONE 3 [111] ORBITS θ AND σ (δ -OSCILLATIONS)
 Figure 6.5. [111] orbits: α , ζ , θ , and σ

the $[100]$ orbit v , since these last three areas were obtained directly from the computer calculation. The resulting areas from models A and B are shown in Table 4.1. The areas measured with the planimeter are probably accurate to only 3%.

As can be seen from Table 4.1 both models give fairly good agreement with the dHvA results. Although the parameters were taken from the third-band surface alone, the models are quite successful in accounting for the second-band surface as well. In order to improve the fit for orbits such as ξ and w additional Fourier coefficients (for example V_{220}) might be necessary. Also, the addition of a spin-orbit coupling term might affect the results. In Appendix C we have noted that the inclusion of spin-orbit coupling should not make an appreciable change in the shape of the third-band Fermi surface (since we are fitting to this surface), but the shape of the second band surface might be modified. Figure 11.5 shows $E(\underline{k})$ curves corresponding approximately to model A with and without the spin-orbit term. We note that the second-band energy may be lowered slightly with respect to that of the third band, when spin-orbit coupling is included. This lowering suggests a smaller second-band (110) area, which is in better agreement with the dHvA results. Figure 11.6 shows $E(\underline{k})$ curves corresponding to model B; here, however, the spin-orbit term has the opposite effect.

All the long dHvA periods observed can be accounted for

by the multiply-connected third-band surface. In agreement with this fact model B predicts that the fourth-band is empty with a small energy gap at W of $\sim .01$ ry from the Fermi level (Figure 5.11). On the other hand, model A does not require the fourth-band to be empty (Figure 5.11) and would predict the occurrence of oscillations of very long period ($\sim 2 \times 10^{-7}$ Gauss⁻¹) from small electron 'pockets' centered on W . Such oscillations have not been observed in lead. Figure 11.7 shows the effect of the addition of the spin-orbit interaction term on the energy levels at W . The energy of the fourth band for model A might rise above the Fermi level for the correct value of the spin-orbit parameter and, in that case the fourth band should be empty for model A.

6.1.2. Orientation dependence

The results of the OPW interpolation method are not in a form suitable for describing the orientation dependence, unlike the results from the Fourier expansion method. However, we have been able to estimate graphically the orientation dependence of the areas enclosed by ζ , ν , and ξ for rotation in a (100) plane. These results are shown in Figure 6.6, where the experimental points have been repeated from Figure 4.5.

The orientation dependence of the γ' oscillations predicts a tapering of the arms (period varies less rapidly than

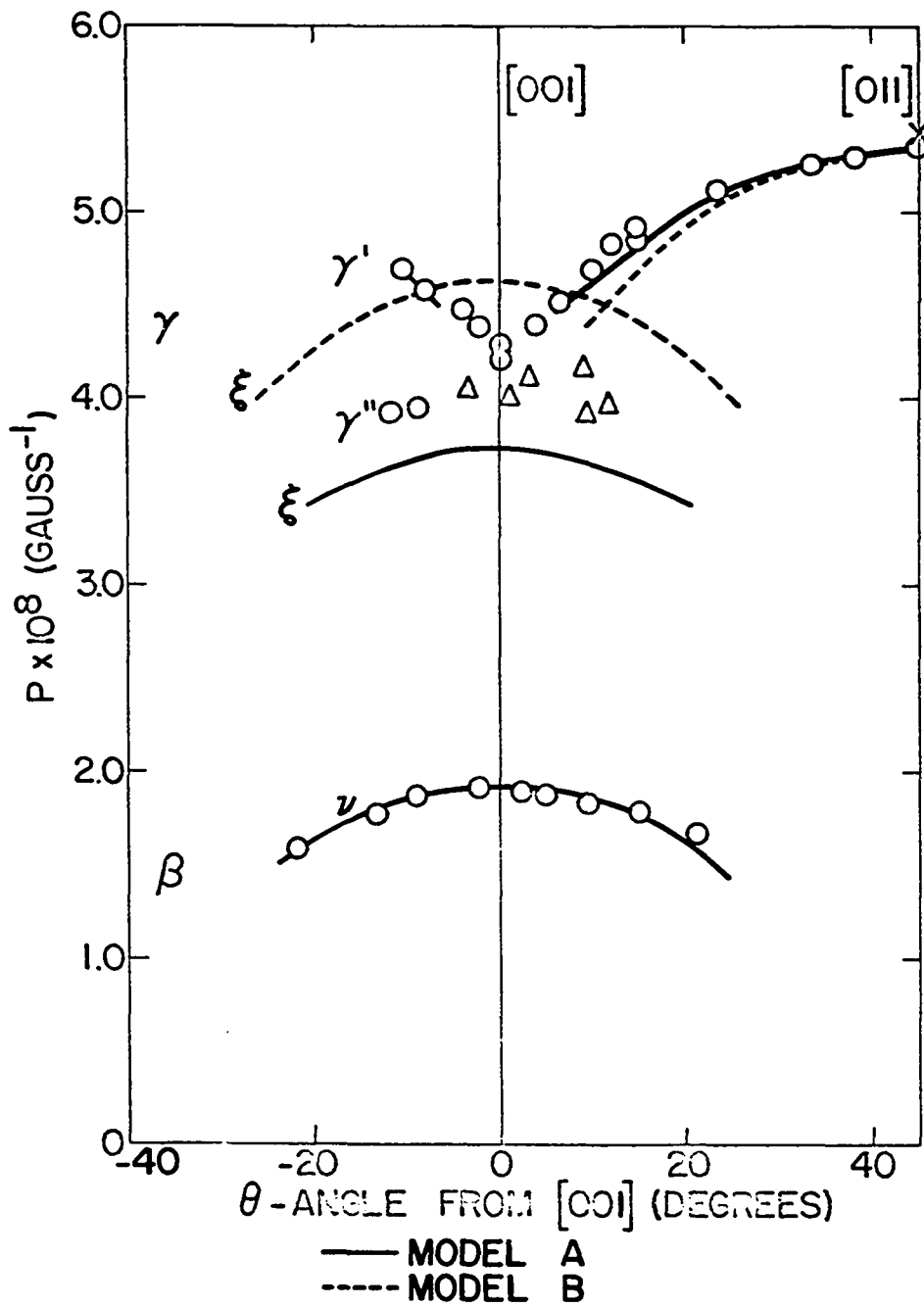


Figure 6.6. Orientation dependence of dHvA periods calculated from the two-parameter models

the cosine of the angle from $[110]$). This tapering is also suggested by the occurrence of long beats in the γ' oscillations (Chapter 4). Model A also predicts such a tapering and in fact gives a reasonable fit to the γ' oscillations; however, model B does not predict any tapering.

The orientation dependence of the β period agrees very well with the ν -orbit period estimated from either model; therefore only one curve has been drawn representing both models. The ξ -orbit period has approximately the same angular dependence as the γ'' period, but the actual period values are somewhat different. Model B gives closer agreement with these γ'' oscillations; however, in view of the uncertainties connected with these oscillations (Chapter 4), we favor model A which predicts tapering of the arms.

6.1.3. Angular range for the existence of orbits

The limiting direction of H for observation of a particular orbit can be estimated from the models with an uncertainty of possibly 4° . To within this accuracy the results predicted by models A and B are the same and in Table 6.1 only an average is given to be compared with experimental values from dHvA, magnetoacoustic, and cyclotron resonance measurements.

We must emphasize that exact agreement between the measured and calculated results is not expected, since the models should predict the maximum angular range. In this connection

Table 6.1. Angular range for existence of orbits (measured from relevant symmetry directions)

Orbit	Plane of tilt	Experimental			Calculated 2-Parameter models
		dHvA	Ultrasonic attenuation	Cyclotron resonance	
[001] ξ	(100)	19° ^a	23° ^b	25° ^{cd}	27°
[100] ν	(100)	29°		40° ^c	26°
[100] η	(110)		21° ^b	25° ^{dc}	28°
[111] θ	(211)		18° ^b	16° ^c	24°

^aGold (1958b).

^bMackintosh (ca. 1962).

^cKhaikin and Mina (1962).

^dAccording to the results of Khaikin and Mina, these two masses join at about 12° from [100].

the cyclotron resonance result for the [100] ν orbit is somewhat surprising. Possibly because of its low phase the cyclotron resonance experiment may be detecting a non-extremal orbit which would not be observed with the higher phase dHvA experiment. It is difficult in practice to determine from the model whether an orbit in a plane tilted from a symmetry direction is extremal or not.

6.1.4. Cyclotron mass and electronic specific heat

Cyclotron masses corresponding to four orbits have been calculated for the two parameter models from the relation $m^* = \hbar^2/2\pi (\partial A/\partial E)_{E_F}$ (Section 1.3.5). Figure 6.7 shows a plot of A versus E for the $[100]$ ν and $[110]$ ω orbits, and Figure 6.8 shows a similar graph for orbits $[110]$ ζ and $[110]$ α . The results for model B are shown, but model A gives almost identical values. The mass ratios for these orbits, calculated from the slopes of the curves, differ very little from the corresponding single OPW ratios calculated by Harrison's method (Harrison 1960b) (Table 6.2).

The energy contains a scaling factor which depends upon the choice of mass (Section 5.4). Here we assume that this scaling factor corresponds to the free-electron value so that all mass ratios are given with respect to this quantity. In other words, we assume the free-electron value for the mass associated with the single OPW sphere when Bragg reflections are ignored.

Also given in Table 6.2 is a comparison of mass values obtained from dHvA amplitudes with those obtained from the more direct (and more reliable) cyclotron resonance experiment (Section 1.3). These values are found to be in good agreement where comparison is possible. However, the experimental values are greater than those predicted by the single OPW and two-

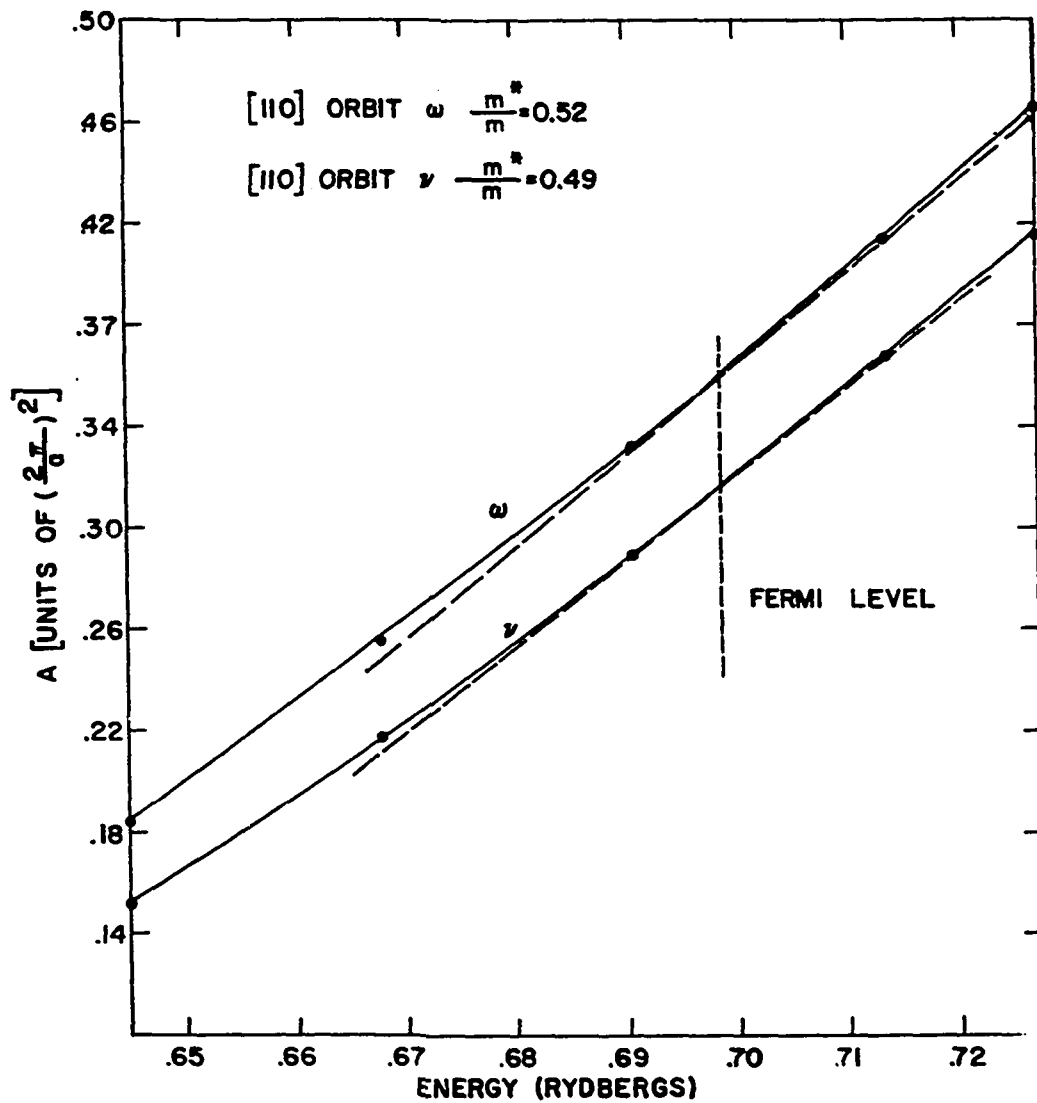


Figure 6.7. Plot of \star versus E for the orbits [100] ν and [110] ω

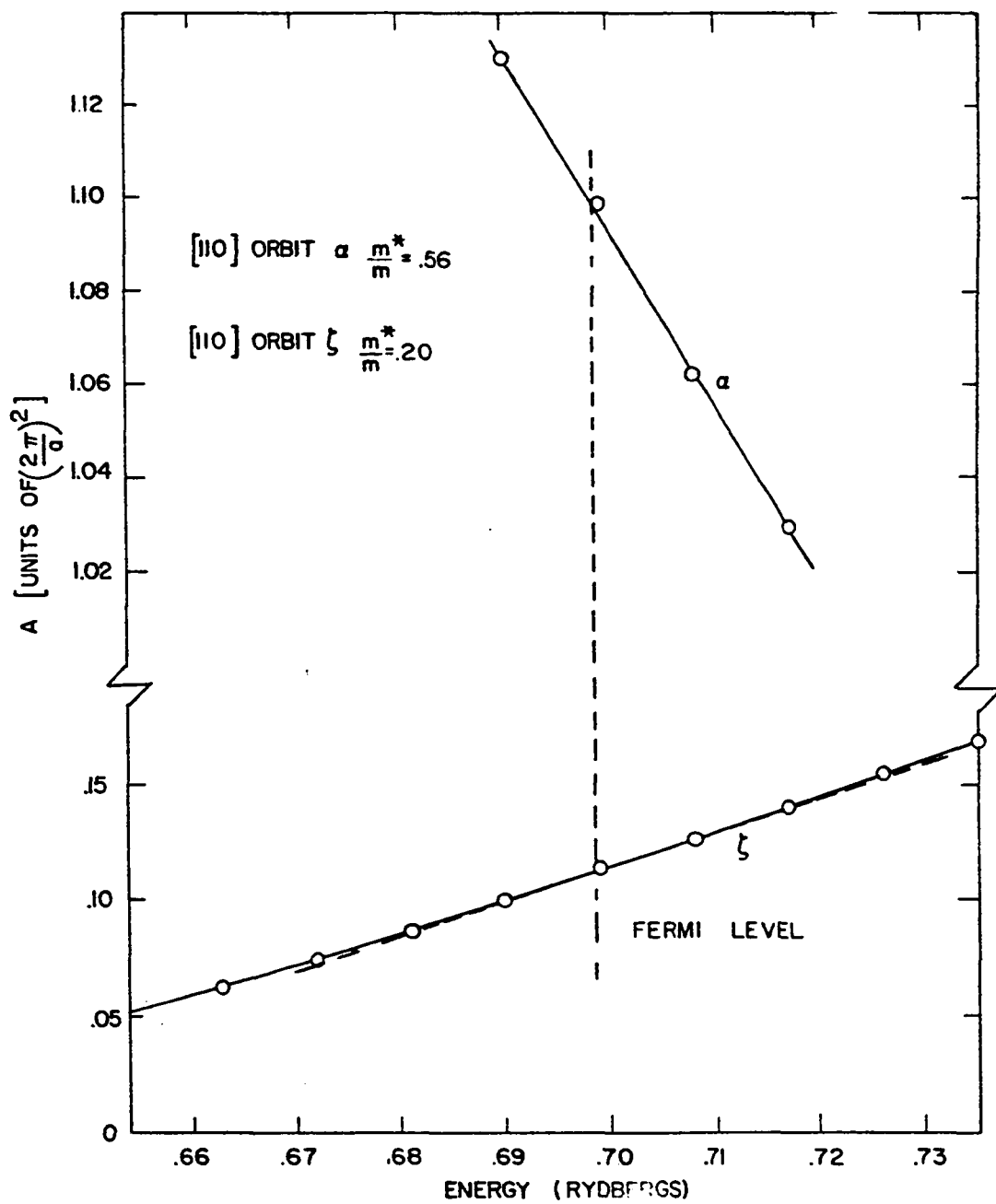


Figure 6.8. Plot of A versus E for the orbits $[110]$ ζ and $[110]$ α

Table 6.2. Cyclotron masses

Orientation	Orbit	m^*/m			
		dHvA	Cyclotron resonance	Single OPW model	Two parameter model
[110]	ζ	0.56 ± 0.06^a	0.56 ± 0.02^b 0.55^c	0.21	0.20
[110]	α	1.0 ± 0.1^a	$1.1 - 1.2^c$	0.58	0.56
[110]	ω		1.35 ± 0.04^b $1.25 - 1.4^c$	0.52	0.52
[100]	ζ		0.75 ± 0.02^b 0.75^c	0.25^d	
[100]	ξ	0.85 ± 0.1^e	0.9^c	0.19	
[100]	ν	1.3 ± 0.15	1.35^c	0.49	0.49
[100]	η		1.28^c	1.00	
[111]	α		1.21^c	0.59	
[111]	ϵ		1.26^c	0.44	

^aGold (1958b).

^bYoung (ca. 1962).

^cKhaikin and Mina (1962).

^dThis orbit is not extremal for the single OPW model.

^eThis mass has been associated with orbit ξ (possibility (b) in Section 4.3). However, if possibility (a) is the correct one, the mass would be due to a combination of the ξ and ζ orbits.

parameter models by approximately a factor of two.

This same mass discrepancy has occurred in other metals. For example, band calculations for aluminum (Heine 1957a; Harrison 1960a) give a mass ratio m^*/m of approximately unity which is too small by roughly a factor of two compared to the electronic specific heat value. As another example, for the bcc phase of sodium, Stern has estimated from specific heat measurements that m^*/m may be as high as 1.7 while $m^*/m \sim 1$ from band calculations (Quinn 1960, p. 64).

This discrepancy may well be resolved in an approximate fashion by a change of scaling factor due to electron interactions. Thus Harrison and Quinn have suggested that electron-electron and electron-phonon interactions could correct for the mass discrepancies in aluminum and sodium, and we should expect these effects to be important in lead as well. The transition temperature in lead is relatively high ($\sim 7^\circ\text{K}$) and the Debye temperature is low ($\sim 90^\circ\text{K}$), and both of these facts suggest a strong electron-phonon interaction. Also, the density of conduction electrons is roughly the same for both lead and aluminum and this fact implies similar electron-electron interactions.

The problem of treating electron-electron and electron-phonon interactions is, however, very complex. Heine (1957c) included correlation and exchange corrections from first-order Bohm-Pines theory in his band calculation of aluminum. This

gave an appreciable correction to the specific heat of the wrong sign. Fletcher and Larson (1958) extended the Bohm-Pines results to second order and a large correction of the proper sign resulted. This large correction casts doubt upon the convergence of the expansion.

It has also been shown that effects of electron-electron interactions enter differently for different experiments. For example, Kohn (1961) has shown that the cyclotron mass, as well as the dHvA period, of a free-electron gas is unchanged by electron-electron interactions, while Gell-Mann (1957) has shown that these interactions do affect the specific heat of an electron gas. Consequently, it seems reasonable not to attempt to include corrections for electron-electron or electron-phonon interactions in a band calculation or in a determination of the Fermi surface. These corrections could be included later, modifying the properties of electrons in a fixed band structure.

We have already noted from Table 6.2 that reasonable agreement with the observed cyclotron masses is obtained if the free-electron masses are, roughly speaking, scaled up by a factor of 2. The different scaling factors for various orbits can be accounted for in a semi-quantitative manner as follows. The cyclotron mass can also be written as

$$m^* = \frac{\hbar}{2\pi} \int \frac{dk_{\tan}}{v_1} , \quad (6.1)$$

where we take the integral around the orbit of the reciprocal of the component of the velocity normal to \underline{H} (Chambers 1956). We now assume that v_1 is changed from the free-electron value v_{10} because of electron interactions, and we divide the orbit up into a 'smooth part' and perturbed sections near the Bragg planes; the velocities are assumed to be different in these regions.

For example, if we consider the cross-section of an arm ($[110]$ ζ), we assume that the velocities are modified as shown in Figure 6.9a. Here α_1 , α_2 , and γ_1 are scaling factors to correct the velocities from the free-electron value; the same scaling factor γ_1 is taken to apply to all the 'smooth' portions in the third zone. Then the expression for the cyclotron mass for this orbit can be written from Equation 6.1:

$$m^* = \frac{\hbar}{2\pi} \left[\int_a^b \frac{dk_{\tan}}{\alpha_1 v_{10}} + \int_b^c \frac{dk_{\tan}}{\gamma_1 v_{10}} + \int_c^d \frac{dk_{\tan}}{\alpha_2 v_{10}} \right. \\ \left. + \int_d^e \frac{dk_{\tan}}{\gamma_1 v_{10}} + \int_e^f \frac{dk_{\tan}}{\alpha_1 v_{10}} + \int_f^a \frac{dk_{\tan}}{\gamma_1 v_{10}} \right] \quad (6.2)$$

According to the two-parameter models the shape of the orbit does not differ too much from the shape of the single OPW orbit. This suggests that the mass ratio can be determined by summing angles subtended by the arcs (ab, bc, etc.)

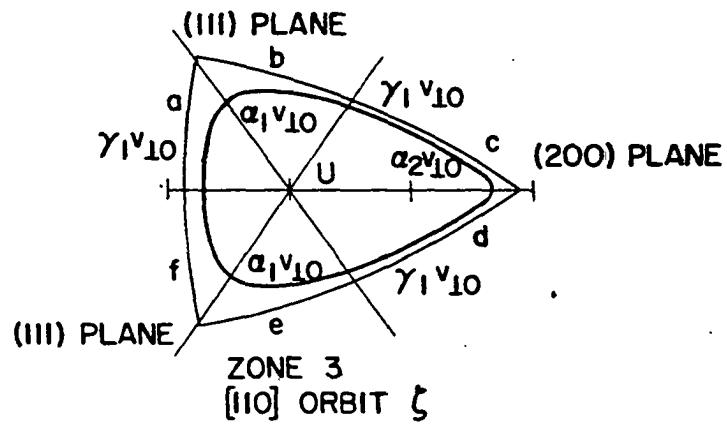


Figure 6.9a. Modified velocities for the $[110]$ ζ orbit

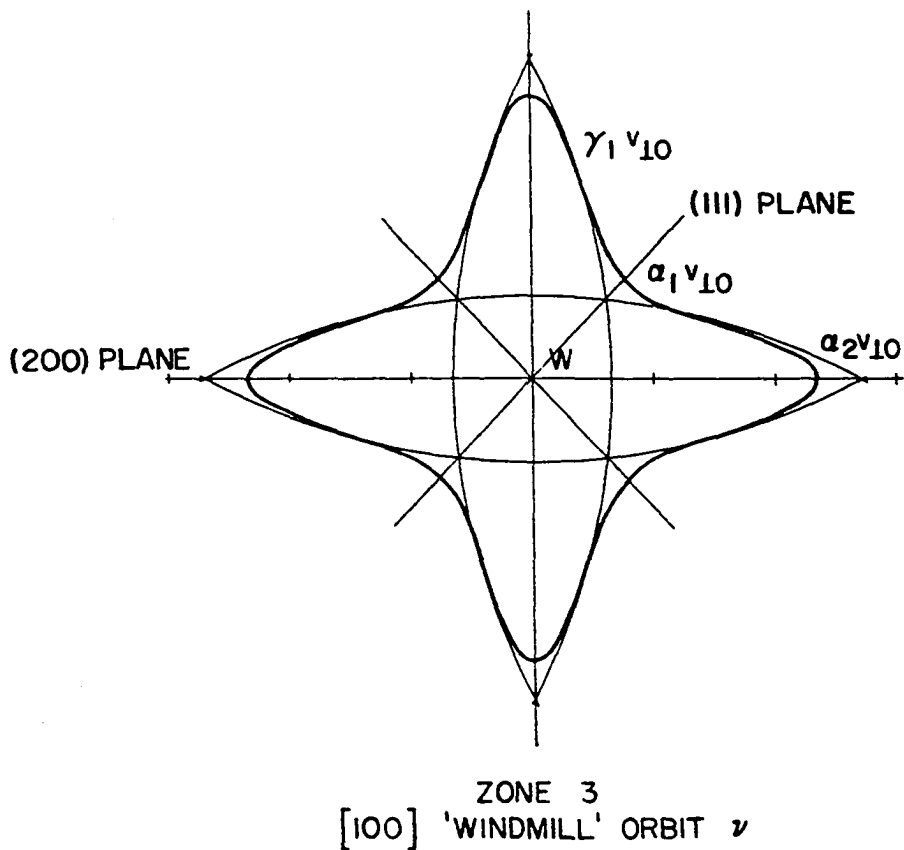


Figure 6.9b. Modified velocities for the $[100]$ ν orbit

and dividing by 2π , as is correct for the single OPW case (Harrison 1960b). If this assumption is made, Equation 6.2 can be written

$$\begin{aligned} \left(\frac{m^*}{m}\right) [\bar{1}10]_{\zeta} = & \frac{1}{2\pi} \left[\frac{\Delta\theta_{ab}}{\alpha_1} + \frac{\Delta\theta_{ef}}{\alpha_1} + \frac{\Delta\theta_{cd}}{\alpha_2} + \frac{\theta_{ad} - \Delta\theta_{ab} - \Delta\theta_{cd}}{\gamma_1} \right. \\ & \left. + \frac{\theta_{da} - \Delta\theta_{ef}}{\gamma_1} \right] \end{aligned} \quad (6.3)$$

Here m is the free electron mass; θ_{ad} and θ_{da} are the angles subtended by the arcs ad [$= (a, b) - (c, d)$] and da [$= (c, d) - (e, f) - (a, b)$] of the single OPW surface, so that

$$\frac{\theta_{ad} + \theta_{da}}{2\pi} = \left(\frac{m_0}{m}\right) [\bar{1}10]_{\zeta}, \text{ the single OPW mass ratio. The}$$

angles $\Delta\theta$ account for the rounding at the Bragg planes and can be thought of as the angles subtended by arcs at the intersections of Bragg planes with the Fermi sphere. This rounding is assumed to be the same over the entire plane, i.e. at all intersections. Then if we define

$$\beta_1 = \Delta\theta_{ab} \left(\frac{1}{\alpha_1} - \frac{1}{\gamma_1} \right) = \Delta\theta_{ef} \left(\frac{1}{\alpha_1} - \frac{1}{\gamma_1} \right) \quad (6.4)$$

and

$$\beta_2 = \Delta\theta_{cd} \left(\frac{1}{\alpha_2} - \frac{1}{\gamma_1} \right),$$

we find from Equation 6.3

$$\left(\frac{m^*}{m}\right) [\bar{1}10]_{\zeta} = \frac{1}{\gamma_1} \left(\frac{m_0^*}{m}\right) [\bar{1}10]_{\zeta} + 2\beta_1 + \beta_2 \quad (6.5)$$

The mass ratio for orbit ζ is now written in terms of three parameters. We assume that the same values of β_1 and β_2 account for all orbit intersections with (111) planes and (200) planes, respectively. Turning now to the windmill orbit ($[\bar{1}00]_{\nu}$) around W (Figure 6.9b), we find with the above assumptions

$$\left(\frac{m^*}{m}\right) [\bar{1}00]_{\nu} = \frac{1}{\gamma_1} \left(\frac{m_0^*}{m}\right) [\bar{1}00]_{\nu} + 4\beta_1 + 4\beta_2 \quad (6.6)$$

Originally it was thought that three parameters γ_1 , β_1 , and β_2 would be sufficient to adjust the single OPW masses, but the cyclotron masses for the second band hole surface were too small compared to the masses on the third band surface. Therefore, the fourth parameter γ_2 was added and the velocity on the smooth parts of the second-band surface was assumed to be scaled differently (γ_2) from that on the smooth parts of the third-band surface (γ_1); the same parameters, β_1 and β_2 , were used for the effects at the intersections with Bragg planes. Since we now had four parameters, it was necessary to use two additional cyclotron masses. These masses were chosen to be associated with the second-band hole surface and the same procedure as before was used to obtain the following mass

ratios:

$$\left(\frac{m^*}{m}\right) [110]_{\alpha} = \frac{1}{\gamma_2} \left(\frac{m_0^*}{m}\right) [110]_{\alpha} + 4\beta_1 + 2\beta_2 \quad (6.7)$$

$$\left(\frac{m^*}{m}\right) [111]_{\alpha} = \frac{1}{\gamma_2} \left(\frac{m_0^*}{m}\right) [111]_{\alpha} + 6\beta_2 \quad (6.8)$$

Substituting the values for the single OPW and observed cyclotron masses from Table 6.2 into Equations 6.5, 6.6, 6.7. and 6.8 and solving the four simultaneous equations, we find:

$$\beta_1 = -0.043, \beta_2 = -0.0166, \gamma_1 = 0.319, \text{ and } \gamma_2 = 0.495.$$

With these values the adjusted cyclotron masses for four other orbits were calculated from the free-electron values and the results are shown in Table 6.3. These we consider to be

Table 6.3. Adjusted single OPW masses compared with experimental masses

Orbit	Cyclotron Mass	
	Experimental value	Adjusted single OPW value
[100] ξ	0.90	0.53
[111] θ	1.21	1.2
[110] ω	1.35	1.39
[100] ζ	0.75	0.69

in reasonable agreement in view of the roughness of our estimate. The only important discrepancy is for the $[100]$ ξ mass.

The above procedure does not work for an orbit following a "ridge" instead of crossing it. Therefore, the mass ratio corresponding to orbit η , for example, cannot be determined.

It is also possible to estimate the electronic specific heat by means of this procedure and the formula for the density of states at the Fermi surface:

$$N(E_F) = \frac{1}{2\pi^2 \hbar^2} \int_{\text{Fermi surface}} m^*(k_z) dk_z, \quad (6.9)$$

where $m^*(k_z)$ is the total cyclotron mass in a plane $k_z =$ constant. In order to make this estimate the intersections of the free-electron sphere with planes parallel to one another and normal to $[110]$ have been considered. The extended-zone picture has been employed and the values of α_1 , α_2 , β_1 , and β_2 as determined above have been used to estimate the cyclotron masses for the various plane sections. For example, for a (110) plane through Γ we find $\frac{m^*}{m}(k_z = 0) = 2.21$ (equivalent to the sum of the contributions from a hole surface and two arm cross-sections). Similar values were estimated for eight planes perpendicular to the $[110]$ direction at various distances from the origin under the assumption that the fourth band was empty. These values were found to change

very little with k_z , so that an average value could be used to determine approximately the density of states $N(E_F)$ as in Equation 6.9. This density of states was divided by the free-electron density of states $N_0(E_F)$ to give $N(E_F)/N_0(E_F) \cong 2.28$. This result is in good agreement with the experimental value $N(E_F)/N_0(E_F) = 2.1$ obtained from electronic specific heat measurements (Decker et al. 1958).

6.2. Extremal Dimensions of the Fermi Surface

6.2.1. Kohn effect

Brockhouse et al. (1961) have studied dispersion curves of lead for lattice vibrations propagating in the $[111]$, $[110]$, and $[100]$ directions, while Paskin and Weiss (1962) have made similar studies using x-rays. We see from Figure 6.10 that so-called Kohn anomalies or kinks can be observed (Section 1.3). However, it is difficult to give a criterion to determine the exact phonon wave-vectors at which these kinks occur. In fact, a kink observed in the $[110]$ dispersion curve (Figure 6.10) was originally thought to occur for a phonon wave-vector of $0.41 (2\pi/a)$, but from the same data Kohn later suggested a value of $0.47 (2\pi/a)$. The positions of the kinks have been estimated for this and other dispersion curves using Brockhouse's interpretations when they were given. The extremal dimensions determined from these wave vectors are shown in Table 6.4 along with values calculated from the two-

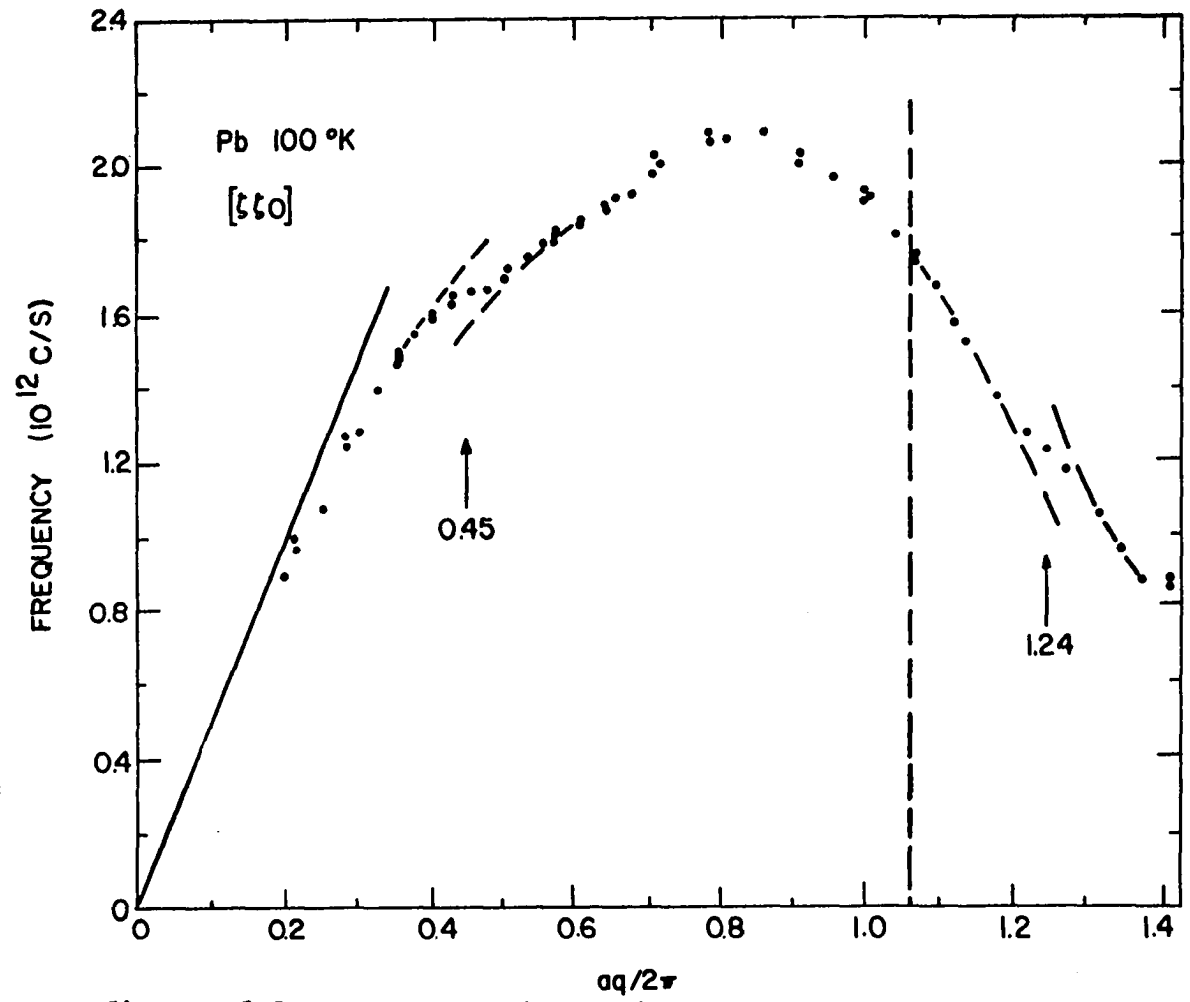


Figure 6.10. Phonon dispersion curve for lead
(after Brookhouse et al. 1961)

Table 6.4. Extremal dimensions of Fermi surface of lead (units of $2\pi/a$)

Orbit	Direction of extremal dimension	Figure reference	Single OPW	Calculation models*		Magneto-acoustic effect	Kohn effect
				A	B		
[110] α	[100]	6.1 a	1.54	1.50	1.510	1.45**	
[110] ζ	[100]	6.1 d	0.465	0.33	0.35	0.35**	***
[100] ν	[100]	5.6 f	1.05	0.91	0.87		0.75-0.9 [†] 0.87-0.97 [‡]
[100] ξ	[100]	6.5 l	0.54	0.64	0.38		
[100]	[100]	6.5 m	1.46	1.36	1.63		
[100] α	[100]	6.3 s	1.50	1.49	1.490		
[110] ω	[100]	6.2 v	0.48	0.37	0.606		

*Model A: $|V_{111}| = 0.069$ ry, $V_{200} = -0.039$ ry; Model B: $V_{111} = 0.045$ ry, $V_{200} = 0.052$ ry.

**Rayne (1962).

***Brockhouse (1961).

[†]There is uncertainty about the existence of this anomaly.

[‡]Paskin and Weiss (1962).

Table 6.4 (Continued).

Orbit	Direction of extremal dimension	Figure reference	Single OPW	Calculation models*		Magneto-acoustic effect	Kohn effect
				A	B		
[111] e	[211]	6.4 i	0.86	0.88	0.88	~0.73//	
[111] σ	[211]	6.4 k	1.78	1.56	1.64		
[111] α	[211]	6.4 p	1.08	0.97	0.96		
[111] c	[211]	6.4 r	0.54	0.38	0.40		
[110] ω	[211]	6.2 w	1.07	0.74	0.90		
[110] α	[111]	6.1 z ₁ z ₂	0.99 0.74	1.0 0.73	0.97 0.76		1.0*** 0.96# 0.73***0.77#
[110] ω	[111]	6.2 x	~0.54	~0.62	~0.68		0.61***

parameter and single OPW models. The letters labeling the extremal dimensions refer to Figures 5.6 and 6.1 - 6.5. The agreement is satisfactory except for the extremal dimension of the $[100]$ ξ orbit in the $[110]$ direction. Although several extremal dimensions determined from the model have approximately the same value as the result obtained from the dispersion curve, only the $[110]$ extremal dimension from the $[100]$ ξ orbit would cause the downward kink observed. This discrepancy will be mentioned again in connection with the magnetoacoustic data. Another possible kink occurs in the longitudinal branch for the wave vector in the $[100]$ direction with magnitude $0.75 (2\pi/a) - 0.9 (2\pi/a)$ and this has been included in the table as a questionable result. In some ionic crystals such as NaI (Woods 1960) a similar shape in the $[100]$ dispersion curve near the zone boundary has been observed and can be fitted using a consistent model of force constants between the atoms. Therefore, this rather pronounced kink might be explained without consideration of the effects of conduction electrons.

6.2.2. Magnetoacoustic effect

Rayne (1962) and Mackintosh (ca. 1962) have estimated some extremal dimensions from their magnetoacoustic data (Section 1.3). Their results are included in Table 6.4. Unfortunately, the unpublished data we have received from Rayne

are rather incomplete and we have no information about the accuracy of the extremal dimensions given. However, the magnetoacoustic values are probably more accurate than neutron scattering values in view of the uncertainty in positioning the kink.

The $[110]$ dimension for the $[100]$ ξ orbit determined from the two-parameter models is in good agreement with magnetoacoustic results. The Kohn effect appears to predict a value larger by about 10%, but in view of the uncertainties mentioned above the magnetoacoustic prediction is more reliable.

Another extremal dimension in the $[110]$ direction obtained from magnetoacoustic measurements, namely $0.39 (2\pi/a)$, could be associated with any of three orbits, $[110]$ ζ , $[110]$ ω , or $[100]$ ν , since both models A and B predict similar $[110]$ dimensions for these orbits. Whatever the interpretation, there appears to be a difference of about 10% between the experimental value and the calculated values. The results available at present do not help us to choose between model A and model B.

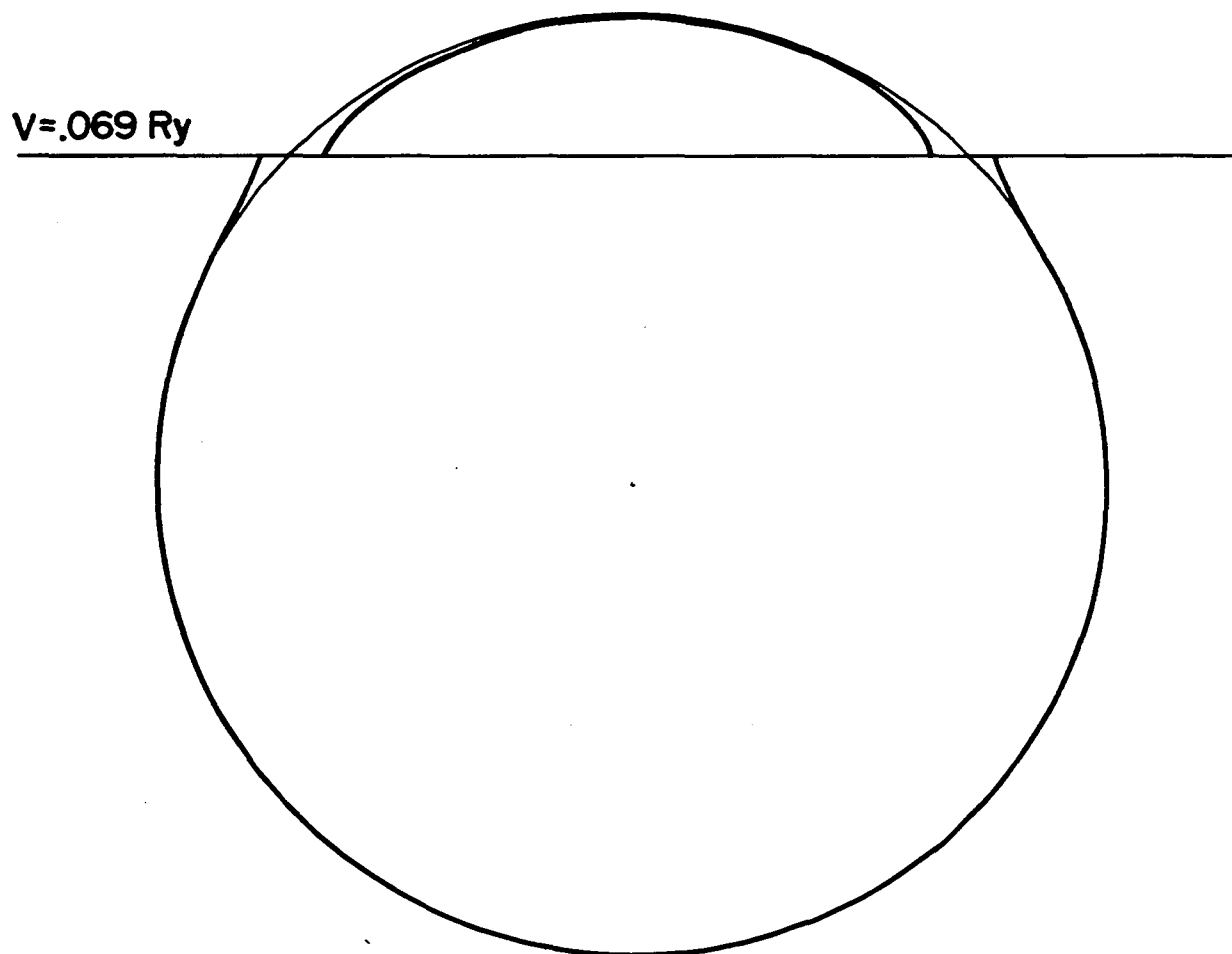
6.3. Surface Area

The effect of the pseudopotential on the total area of the Fermi surface can be estimated if we consider the effect of one Bragg plane at a time. If the decrease in surface area

due to a single Bragg plane is small, the decrease in area due to all Bragg planes intersecting the Fermi sphere should be approximately the sum of the changes for individual planes; this is because the shape of the Fermi surface in the extended-zone scheme remains practically spherical, except in the immediate neighborhood of a Bragg plane (Figure 5.10). Thus the effect of any particular plane may be regarded as being independent of the presence of other planes.

In Figure 6.11 we see the modification of the free-electron sphere by a single Bragg plane of type $[111]$ at a distance $0.866 (2\pi/a)$ from the origin, corresponding to a matrix element $|V_{111}| = 0.069$ ry as in model A. The change in surface area is not difficult to determine since the modified sphere is still a figure of revolution about the central $[111]$ axis normal to the Bragg plane. The decrease in area ΔS due to this plane is graphically found to be $\Delta S = 0.50 \pm 0.08 (2\pi/a)^2$; and, since the surface area of the free-electron sphere $S_{FE} = 19.3 (2\pi/a)^2$, we have $\Delta S/S_{FE} = 0.026 \pm 0.004$. Similar estimates have been made for other distances and associated potentials as shown in Table 6.5. This calculation was made before the final parameter values were chosen for models A and B, but the use of these values would not change the results significantly.

For the fcc structure there are 8 $\{111\}$ planes and 6 $\{200\}$ planes intersecting the Fermi sphere for four electrons



**MODIFICATION OF FREE ELECTRON SPHERE
BY A SINGLE BRAGG PLANE.**

Figure 6.11. Modification of free-electron sphere
by a single Bragg plane

Table 6.5. Effect of Bragg planes on surface area

Plane	Distance from origin ($2\pi/a$)	Matrix element $ V $ (ry)	ΔS ($a/2\pi$) ²	$\Delta S/S_{FE}$ (per plane)
[111]	0.866	0.067	0.50 \pm .08	0.026 \pm .004
[111]	0.866	0.045	0.35 \pm .07	0.018 \pm .004
[200]	1.0	0.035	0.20 \pm .07	0.010 \pm .003
[200]	1.0	0.050	0.50 \pm .08	0.026 \pm .003

per atom. The total surface area is approximately the same for both models: $S/S_{FE} = 0.73\pm.1$ (model A) and $S/S_{FE} = 0.70\pm.1$ (model B).

Aubrey (1960) has determined the area of the Fermi surface in lead from measurements of the anomalous skin effect (Section 1.3). He finds $S/S_{FE} = 0.55\pm.05$. However, the accuracy of the experimental value of the Fermi surface area is not high because of several systematic errors which might not have been fully allowed for in Aubrey's estimated error. These arise because:

a. The crystallites in the polycrystalline sample may have a preferred orientation introduced during the extrusion process (cf. Barrett 1943, p. 382).

b. A surface property is measured and this depends critically on surface polish. A poor surface polish will give

a surface area that is too low (Chambers 1952).

c. Effects of relaxation and finite mean-free path require correction. This correction amounts to only a few per cent in measurements on magnesium, zinc, and cadmium (Fawcett 1961).

d. In the estimate of surface area it is assumed that $\langle R_{\infty}^{-3} \rangle$ may be replaced by $\langle R_{\infty} \rangle^{-3}$ where $\langle R_{\infty} \rangle$ is the average of the surface resistance in the anomalous region (Section 1.3). This assumption will not be valid if $R_{\infty}(\theta, \phi)$ is very anisotropic. For both copper and tin, detailed studies of the anisotropy of R_{∞} have been made and the ratio $\langle R_{\infty}^{-3} \rangle / \langle R_{\infty} \rangle^{-3}$ has been estimated. For copper this ratio is found to be 1.11 and for tin 1.25 (Fawcett 1961). These figures in some way reflect the distortion of the Fermi surface from the free-electron sphere. No data on the anisotropy of $R_{\infty}(\theta, \phi)$ for lead are available at present, but we may assume that the surface distortion might be comparable to that in tin. Fawcett (1960) has given an uncorrected value $S/S_{FE} = 0.55$ for tin which is the same as Aubrey's uncorrected value for lead. Thus if Aubrey's result for lead is scaled up by the factor of 1.25 for tin, the ratio of the surface area to that for a free-electron sphere becomes $S/S_{FE} \approx 0.68$. This result is in fair agreement with the calculated results, especially in view of the uncertainties in both estimates.

6.4. Open Orbits

Alekseevskii and Gaidukov (1962) have made very complete magnetoresistance measurements on lead, and their stereographic projection of open orbit directions is shown in Figure 6.12. The magnetoresistance increases quadratically with H over a wide range of field directions (Region II). Saturation of resistance occurs only for H in a (111) plane (Region III) where narrow minima occur for the current perpendicular to a $[111]$ direction and also for H in the $[110]$ direction; here a narrow minimum occurs independent of the direction of current.

To interpret their results, Alekseevskii and Gaidukov used the results of Lifshitz and Peschanski (1959), who classified open orbits into two types:

I. Open orbits in one direction of k -space giving a one-dimensional region of field directions over which the orbit exists. These can occur only when the magnetic field lies in a symmetry plane and region III is an example of this.

II. Open orbits existing at the boundary between a region of electron orbits and a region of hole orbits. In this case a two-dimensional region of field directions would exist where open orbits occur. Region I on the stereographic projection is of this type. Region II is a region where no open orbits exist.

In discussing open orbits we shall for simplicity consider

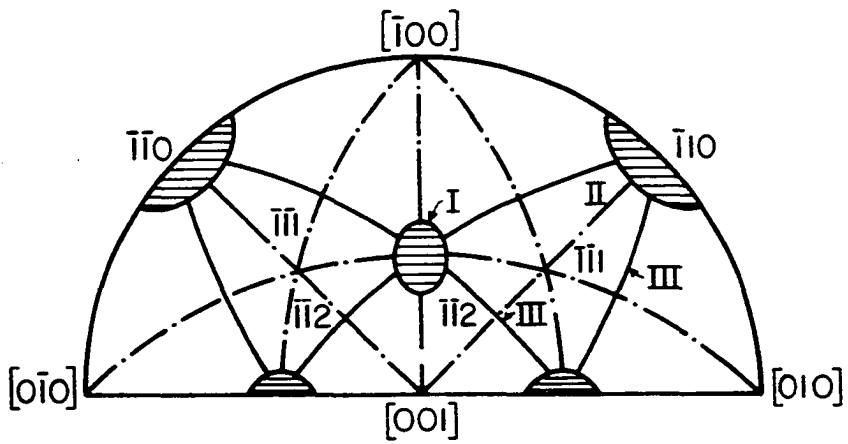


Figure 6.12. Stereogram of magnetic field directions for which open orbits were found to exist (after Alekseevskii and Gaidukov 1962)

the single OPW Fermi surface since it has a shape very similar to the 2 parameter Fermi surface. Young (ca. 1962) has demonstrated that the single OPW model for lead is compatible with these results of Alekseevskii and Gaidukov, contrary to the interpretation originally given by these authors. He has shown that when the orbit τ (the large hole orbit in Figure 4.4) exists, a plane slightly tilted from the $[110]$ contains regions of electron orbits and regions of hole orbits and an open orbit exists at the boundary between the two regions. Therefore, Region I on the stereographic projection extends over the same range as the orbit τ . According to the single OPW model τ can exist over a range of magnetic field directions $5^\circ - 10^\circ$ from $[110]$ in any direction, in agreement with the results of Alekseevskii and Gaidukov.

Figure 6.13 shows a type I open orbit based on the single OPW model. Here H is in a $[211]$ direction and the orbit runs in the $[111]$ direction. This orbit is the orbit ρ shown on the pipe model in Figure 4.4. As H rotates from the $[211]$ direction in a (111) plane, the orbit ρ ceases to exist when H is a few degrees from $[110]$ because τ exists instead.

The "whiskers" shown on the stereogram of Figure 6.12 for H perpendicular to $[100]$ and $[110]$ and within a few degrees of the $[110]$ direction are also due to the presence of type I open orbits. Figure 6.14 shows such an open orbit

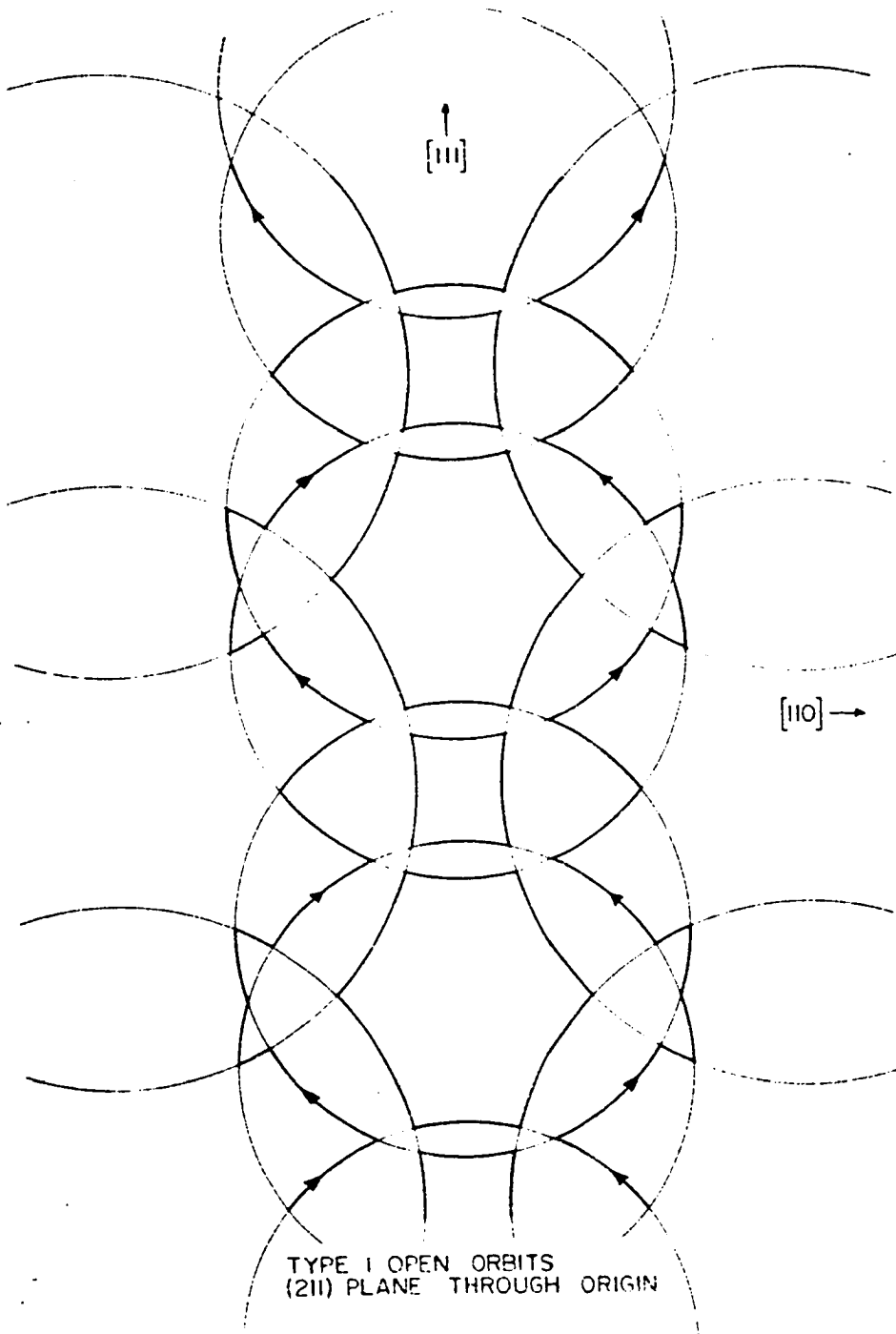


Figure 6.13. Type I open orbits as given by the single OPW model

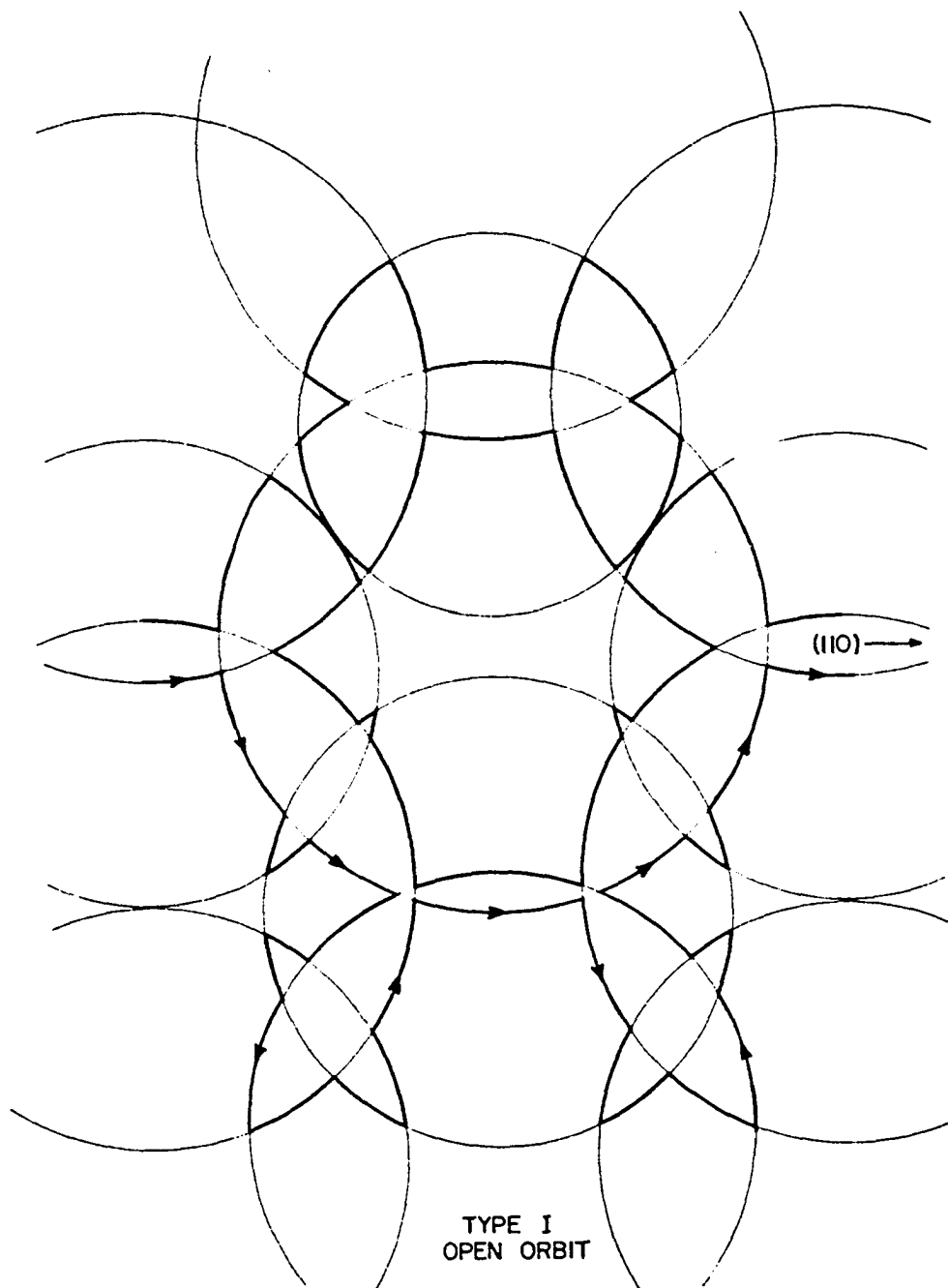


Figure 6.14. Type I open orbit as given by the single OPW model (H tilted 5° from $[110]$ in a (110) plane)

running in the general $[110]$ direction for H tilted 5° from $[110]$ in a (110) plane.

Thus the third-band surface of the single OPW model, or slight modifications of it, as in our two parameter models, can account very well for the magnetoresistance results.

6.5. Fitting the β Oscillations into a Particular Model of the Fermi Surface

In his study of lead, Gold associated the β oscillations for H near $[100]$ with the third-band hole orbit ξ inside the square face of the fundamental Brillouin zone shown in Figure 4.4. In the present calculation we have assumed, instead, that the β oscillations correspond to the electron orbit ν around the intersection of four arms. Although experiments were attempted to verify this choice, some uncertainty remains. This problem of the assignment of the β oscillations is of such paramount importance (these being used in the determination of our OPW models) that we devote the following paragraphs to a discussion of the reasons for this association:

a. Agreement with the single OPW approach

The observed dHvA periods fit quite well into a single OPW model and, as was pointed out in Chapter 4, the association of the β oscillations with the ν orbit is consistent with this model. The experimental area corresponding to the period of the β oscillations is $0.31 (2\pi/a)^2$, which agrees better

with the single OPW area $A_{\nu} = 0.30 (2\pi/a)^2$ than with $A_{\xi} = 0.13 (2\pi/a)^2$, as in Gold's original interpretation. If the area A_{ξ} were increased to fit the value of $0.31 (2\pi/a)^2$, we would have a large perturbation from the single OPW model.¹ Also, an increase in the area of A_{ξ} would probably put too much taper in the arms to fit the orientation dependence of the γ' period (Figure 6.6). In addition to the agreement of the absolute magnitudes, the orientation dependence of the ν -orbit period, as predicted by either the single OPW or the two-parameter models, agrees closely with the dependence of the β period shown in Figure 6.6.

However, if this interpretation for the β -oscillations is correct, the γ'' oscillations, which we have associated with ξ are of rather low amplitude and this result is puzzling. Both A_{ν} and A_{ξ} are extremal and the single OPW model predicts that the curvature factor $(\partial^2 A / \partial k_z^2)^{-1/2}$, which occurs in the amplitude expression 3.8, is roughly the same for both areas, namely 0.9 for A_{ν} and 0.6 for A_{ξ} . A factor P^{-2}

¹It is true that the cross-section of an arm A_{ξ} would have to be decreased from the single OPW value by nearly 50% to agree with experiment, but both V_{111} and V_{200} help with this reduction. For A_{ν} , on the other hand, inclusion of V_{111} tends to increase the area while V_{200} causes the area to decrease. Thus we might expect A_{ν} to be little changed from its single OPW value as appears to be true experimentally.

occurs in Equation 3.8 and the period associated with the orbit ξ is about twice the period associated with orbit ν . On the other hand, the single OPW ξ mass is smaller than the ν mass by, roughly speaking, a factor of two (Table 6.2) and the same holds for the observed masses; this result has the opposite effect on the amplitudes. Thus from a combination of these factors we would expect $A_{\xi} \cong \frac{1}{3} A_{\nu}$ for $H = 80$ kG if the relaxation time is taken to be the same for both orbits ($x = 1^{\circ}\text{K}$), whereas in practice we find $A_{\xi} < A_{\nu}$. A further puzzling feature is that the oscillations μ associated with the orbit ω , also at the junction of four arms, have very low amplitude whereas we might expect this amplitude to be comparable to that of the β oscillations. Possibly lattice broadening effects could be different for different orbits and this problem remains for further study.

b. Mass Agreement

The cyclotron mass values agree well with the values determined from the temperature dependence of the dHVA amplitudes. As was discussed in Section 6.1, the free-electron masses can be scaled up by a factor of roughly two to agree with the experimental masses; however it can be seen from Table 6.2 that an abnormally large scaling factor of seven would be required if the high-mass β oscillations were associated with the orbit ξ rather than orbit ν . Young (ca. 1962) (and probably Khaikin and Mina 1962) has studied rf polariza-

tion effects (Section 1.3) and decided that the mass corresponding to the β oscillations must refer to an orbit for which the velocity in the field direction averaged around an orbit \bar{v}_z may be zero, but that $v_z \neq 0$ at some places on the orbit. For orbit ξ , $v_z = 0$ at all points on the orbit, while this is not true for the orbit ν . This is probably the most important reason for associating orbit ν with the β oscillations.

c. Alloy studies

We have shown that better overall agreement is obtained if the ν orbit is associated with the β oscillations, but it should be possible to establish this definitely by studying the effects of alloying on the dHVA periods. Accordingly some studies were attempted using lead alloys with about 1/2% bismuth, 1/2% thallium, and a combination of 1/4% bismuth and 1/4% thallium. If a rigid band structure is a reasonable approximation, we might expect the addition of thallium to increase the period of the β oscillations if they refer to the electron orbit ν and decrease the period if they refer to the hole orbit ξ . For the bismuth alloy the opposite effect should occur, while the ternary alloy should give a partial check on the rigid-band model, being of the same electron concentration as pure lead. Unfortunately the added elements considerably reduced the mean free path and although oscillations were observed, there were not enough cycles to obtain sufficiently accurate period measurements. This experiment

should be repeated using more care in the alloy preparation together with beat techniques (Chapter 7).

Further careful period measurements as a function of orientation should be made for the field near the $[100]$ direction. If only one γ oscillation period is observed for H exactly parallel to $[100]$, this oscillation should correspond to orbit ξ which is definitely extremal for our model, i.e. possibility (b) in Section 4.3. (It is unlikely that the ξ and ζ periods would have exactly the same value for $H // [100]$.) However, with techniques giving better resolution, it is quite possible that more than one period might be extracted from the rather complex oscillograms of the γ oscillations. Khaikin and Mina (1962) observed two masses for $H // [100]$ with values close to the single value found from the γ oscillations in this experiment (Section 4.4). One of their masses was associated with orbit ξ and one with the arm cross-sections ζ , which need not be extremal. Thus this possibility of two γ periods at $[100]$ should be checked carefully with the dHVA effect.

7. CONCLUDING DISCUSSION AND SUGGESTIONS FOR FURTHER STUDY

In this study it has been shown that the Fermi surface of lead is very free-electron-like. In fact, models using only two components of the pseudopotential to perturb the free-electron sphere have been found to fit the available experimental data rather closely. (We are inclined to favor model A over model B because model A predicts the taper of the third-band arms (Section 6.1).) In this respect lead is similar to aluminum (Harrison 1960a; Priestley 1961), indium (Rayne and Chandrasekhar 1962), zinc (cf. Harrison 1962), and magnesium (Priestley 1961). The results of many experiments suggest that all polyvalent metals may have a free-electron-like Fermi surface. Possible exceptions might be the transition and rare-earth metals, on account of their unfilled core states, but as yet the experimental results for such metals are fragmentary.

A brief discussion of the necessity for models is in order here. If the Fermi surface has a simple form (centrosymmetric and convex), its shape can be uniquely determined from, for example, the complete orientation dependence of dHvA periods; Lifshitz and Pogorelov (1954) have given an exact mathematical procedure for doing this. However, for polyvalent metals such as lead the Fermi surface may take a com-

plicated shape and may even be multiply-connected: then it is difficult, if not impossible, to obtain an unambiguous shape for such surfaces from experimental data alone. Moreover, it will not in general be possible to fit the observed surface areas into the Brillouin-zone scheme without the aid of a consistent model. Such a model must first be guessed and then compared with experiment. Once adopted, the model may predict further features and suggest additional measurements, as was the case for lead. Finally, the model is modified, as suggested by the new results, until reasonable agreement is obtained.

Some of the details of the Fermi surface of lead require further experimental investigation. Also, lead appears to be a good metal for detailed studies of periods and amplitudes and their dependences upon temperature, magnetic field, crystal perfection, and alloying. It seems worthwhile to list some of these problems:

a. Orientation dependence of the new sets of oscillations in lead. The orientation dependence of the δ_1 oscillations is presently under investigation.

b. Analysis of the oscillations present for H near [100] (Chapter 4). A technique with better resolution is required and this problem is being considered at present. 'Artificial' time-varying frequencies $\nu = \dot{H}/PH^2$ will be produced to be mixed with the dHvA signal. Measurements of the

difference frequencies should give an accurate determination of the dHvA periods. In the future, a computer might be used in conjunction with correlation techniques to sort out the periods.

c. Study of the dHvA periods in alloys to determine whether the oscillations are due to electron or hole orbits (Section 6.5).

d. Cyclotron masses should be determined for the new sets of oscillation. In this connection the reasons should be found for the considerable scatter in the amplitude measurements as a function of temperature (Section 4.4).

e. Study of the effects of the resonance technique when used in a determination of relaxation times from the field dependence of amplitude (Section 3.3). The fact that the relaxation times obtained in this manner are much shorter than the estimates from electrical conductivity (Gold 1958b) should also be considered from a theoretical point of view.

f. Investigation of possible differences between dHvA oscillations from orbits for which only $\bar{v}_z = 0$ and orbits for which $v_z = 0$ at every point on the orbit (Section 6.5).

g. Study of the possible effects of frequency modulation due either to replacement of H by B in the formula for magnetization (Section 4.4) or to interband effects.

h. Study of a crystal for H exactly parallel to $[110]$ in order to look for long beats due to eddy currents (Section

3.3).

i. Search for oscillations due to non-extremal orbits. For example, end points as well as stationary points might contribute to the integral over k_z for the oscillatory component of magnetization (Section 4.3).

j. Optical studies. For example, one might look for the effects of a very small energy gap between the Fermi level and the fourth band near W (Figure 5.11).

k. Studies of the anomalous skin effect in lead single crystals (Section 6.3).

Returning to more theoretical aspects, we might improve upon the pseudopotential interpolation model. A program is presently being carried out to include a fourth OPW at all points of calculation in the zone. This program should allow a more systematic description of the Fermi surface. The values of the matrix elements may be modified, but the shape of the Fermi surface should change very little. The inclusion of a spin-orbit term would also be desirable (Appendix C).

Once model A or model B has been finally selected, this particular model could also be used to obtain an analytic description of the Fermi surface if the coefficients in a symmetrized triple Fourier series are adjusted to fit the band energies at many points throughout the zone. (Each band must be considered separately.) This procedure would tend to smooth out the mismatches made in taking different OPW's at

different points; more important, we could then determine analytically the orientation dependence of the areas, the total surface area, and the open-orbit directions, etc. We would also have a description of the Fermi surface in a form which would be more convenient for a calculation of transport properties.

The possibility now exists for a complete band calculation from first principles (page 126). This calculation is highly desirable in view of the considerable amount of experimental data now at hand. Also, such a calculation should enable us to distinguish between the two models A and B. Probably the OPW method should be used for the band calculation, where the separation between the third band energies at W or U and the Fermi level would be estimated from our two-parameter models.

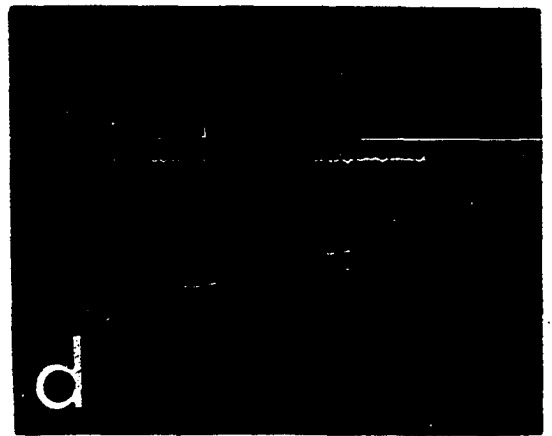
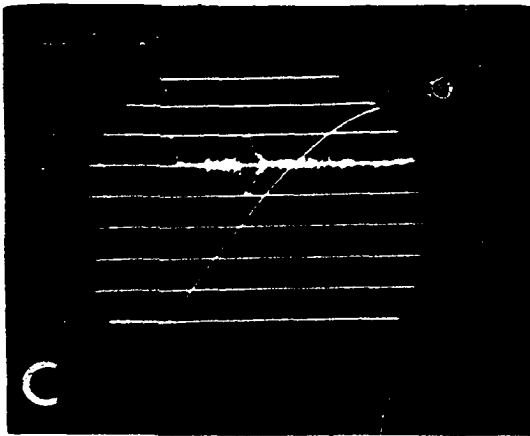
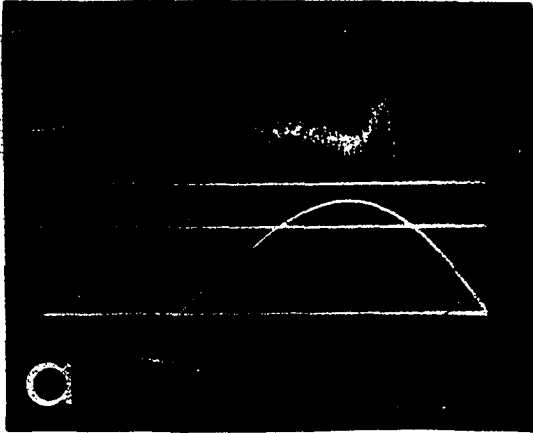
8. PRELIMINARY DHVA STUDIES OF IRON

During the concluding stages of the study of lead de Haas-van Alphen oscillations were discovered in iron whiskers, the first time that the effect has been observed in a ferromagnetic metal. The whiskers were obtained from Dr. R. W. De Blois at General Electric Research Laboratory, Schenectady, New York, and were grown by the Brenner process, hydrogen reduction of ferrous bromide (Brenner 1956). These were roughly 0.1 mm - 0.2 mm in diameter and 5 mm - 8 mm in length. The resistivity ratio $\rho_{293^\circ}/\rho_{4.2^\circ}$ was found to be between 200 and 300, a very satisfactory figure for iron.

Figure 8.1a shows the overall pulse which gave the first recognizable oscillations. A resonant frequency of ~ 18 kc/s was used and, under these conditions, the field at which the oscillations occurred was surprisingly low, about 40 kG. In Figure 8.1b the same oscillations have been spread out for counting. We note from Figure 8.1a that the oscillations are observed for $\dot{H} < 0$. This fact is probably connected with heating due to eddy currents and to the magnetization of the iron. When the iron whiskers were remounted in larger glass capillaries, allowing better access for liquid helium, oscillations were also found for $\dot{H} > 0$. Furthermore this remounting greatly improved the signal to noise ratio as can be seen by comparing Figure 8.1b with 8.1d.

Figure 8.1. Examples of dHvA oscillations in iron

- a. Overall picture for $H // [100]$.
Calibration lines at 0, 114.2 and 171.3 kG.
2.0 ms/cm sweep
- b. Oscillations in (a.) spread out.
Baseline = 34.26 kG and calibration lines at intervals of 11.42 kG.
0.2 ms/cm sweep
- c. Oscillations for $H // [110]$.
Baseline = 0 kG and calibration lines at intervals of 11.42 kG.
1.0 ms/cm sweep
- d. Oscillations in (c.) spread out.
Baseline = 22.84 kG and calibration lines at intervals of 11.42 kG.
0.2 ms/cm sweep



Observation of the oscillations for rising field is further hampered by a violent ringing which occurs at the start of the pulse (right-hand side of Figure 8.1a). This ringing is strictly periodic in time and most probably is a consequence of the increased Q of the pickup coil when it contains the iron whisker.

Since the iron whiskers grow preferentially with axis along a $[100]$ direction, most of our samples were of this orientation and only one sample has been studied for $H // [110]$. The results are qualitatively similar for the two orientations.

While one distinct set of oscillations with $P \sim 10^{-7}$ Gauss $^{-1}$ has been observed (Figures 8.1b and 8.1d), there are indications that oscillations of still longer period ($P \sim 10^{-6}$ Gauss $^{-1}$) exist as well. However, so far we have no clear evidence of faster oscillations corresponding to large portions of the Fermi surface.

Because of the large internal magnetization in iron, a serious complication arises in the determination of dHVA periods. From Equation 1.16, the oscillatory component of magnetization has been written:

$$M = M_0(H, T) \sin \left(\frac{2\pi}{PH} + \frac{\pi}{4} - 2\pi\gamma \right), \quad (8.1)$$

but actually the H in this equation (which we have previously assumed to be equal to the applied field) should always be

replaced by the magnetic induction B (Chapter 3). This correction is essential in ferromagnetic materials. For the very high pulsed fields used in this experiment we would expect that the magnetization would reach saturation almost immediately after the start of a pulse (The applied field necessary to completely magnetize iron is less than 1 kG.) (cf. Piety 1936). Therefore we have added a constant field $4\pi\alpha M_s$ to the applied field H in Equation 8.1, where the saturation magnetization $4\pi M_s$ is 21.8 kG at $T = 0^\circ\text{K}$ (Bozorth 1951, p. 54) and α is an adjustable parameter.

In Chapter 3 a method for period determination was described which consisted of plotting H^{-1} at oscillation maxima or minima versus intergers. For lead, straight lines were obtained and the periods were determined from the slopes. For iron this procedure does not yield straight lines. It is necessary to make a plot of $(H + 4\pi\alpha M_s)^{-1}$ rather than H^{-1} , where α is adjusted to give the best straight line as determined by a least-squares fit. A detailed least-squares computer program has been prepared to extract the true period P_0 and the best value of α .

Another approach was to plot H at oscillation maxima versus integers n and draw a smooth curve through the points. Then if we consider n to be a continuous variable and determine dH/dn , we find

$$n + \beta = P_0^{-1/2} |dH/dn|^{-1/2} \quad (8.2)$$

where β is an unknown constant. A plot of $|dH/dn|^{-1/2}$ versus n should result in a straight line with slope $P_0^{-1/2}$. Figure 8.2 shows such a plot for the oscillations shown in Figure 8.1b. The considerable scatter in the points is partly due to taking derivatives, but a reasonable straight line can nevertheless be drawn. From such graphs of our preliminary data we find $P_0 \approx 10^{-7}$ Gauss $^{-1}$ and α is found to lie between two and three. These values are as yet very approximate.

The surprising fact that α is approximately two or three rather than unity is not understood at present. However, a similar increased value of α has been noted in the anomalous Hall effect in ferromagnetic materials (cf. Volkenshtein and Fedorov 1960). It appears that this effect is related to the spin-orbit coupling in ferromagnets (cf. Kondo 1962).

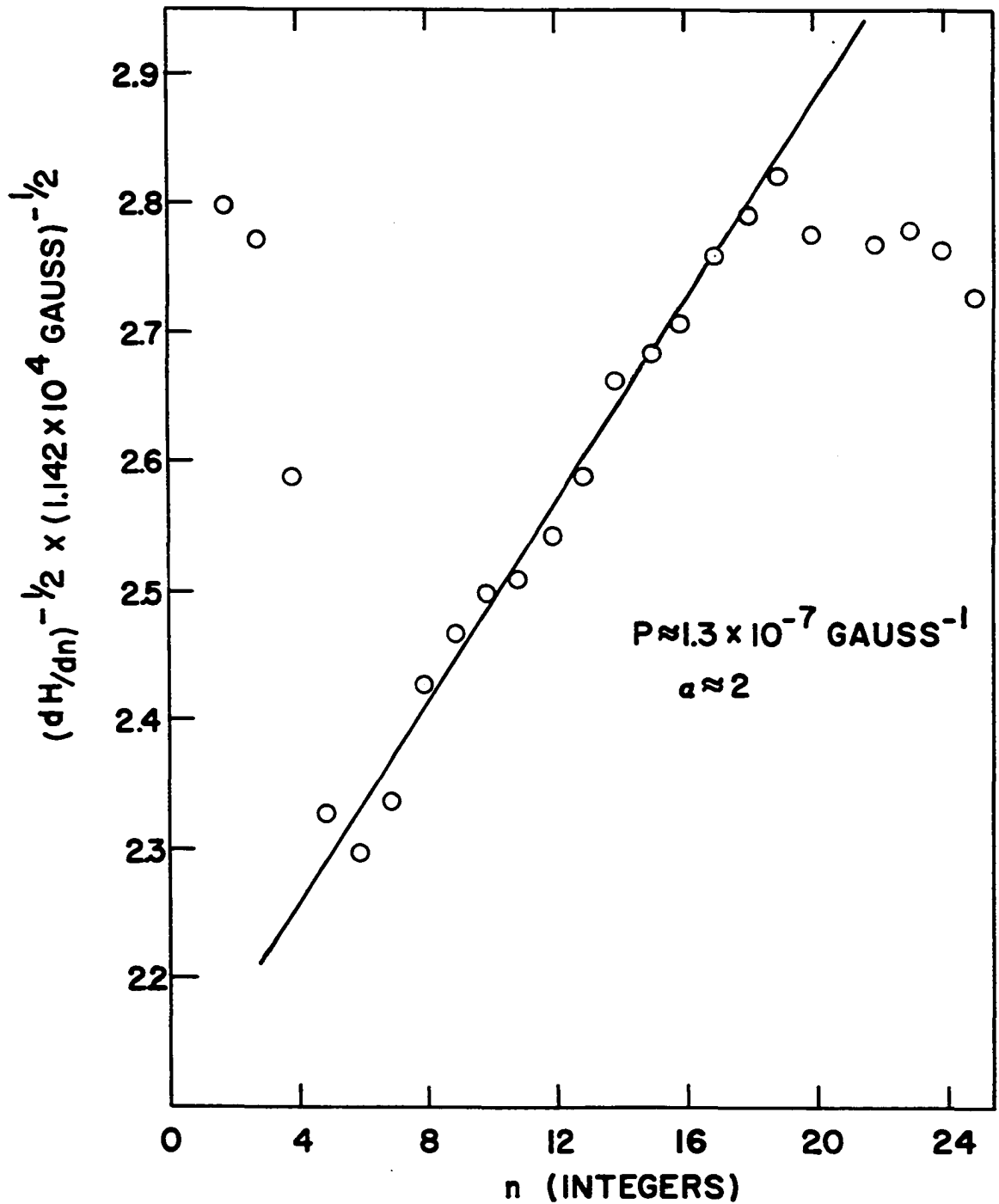


Figure 8.2. Derivative method for determining periods in iron

9. REFERENCES

- Alekseevskii, N. E. and Gaidukov, Yu. P. (1962) Soviet Physics, JETP 41, 14.
- Alekseevskii, N. E., Gaidukov, Yu. P., Lifshitz, I. M., and Peshanski, V. G. (1961) Soviet Physics, JETP 39, 827.
- Aubrey, E. (1960) Phil. Mag. 8, 1001.
- Azbel, M. Yu. and Kaner, E. A. (1956) Soviet Physics, JETP 3, 772.
- Azbel, M. Yu. and Kaner, E. A. (1957) Soviet Physics, JETP 5, 730.
- Barber, N. F. and Ursell, F. (1948) Phil. Mag. 39, 345.
- Barrett, Charles S. (1943) Structure of metals. New York, McGraw-Hill Book Company, Inc.
- Bassani, F. and Celli, V. (1961) Journal of Physics and Chemistry of Solids 30, 66.
- Bouckaert, L., Smoluchowski, R., and Wigner, E. (1936) Phys. Rev. 50, 58.
- Bozorth, R. M. (1951) Ferromagnetism. New York, D. Van Nostrand Company, Inc.
- Brenner, Sidney S. (1956) Acta Metallurgica 4, 62.
- Brillouin, Leon. (1953) Wave propagation in periodic structures. New York, Dover Publications, Inc.
- Brockhouse, B. N., Rao, K. R., and Woods, A. D. B. (1961) Phys. Rev. Letters 7, 93.
- Chambers, R. G. (1952) Proc. Roy. Soc. (London) A215, 481.
- Chambers, R. G. (1956) Canadian Journal of Physics 34, 1395.
- Chambers, R. G. (1960) Magnetoresistance. In Harrison, W. A. and Webb, M. B., eds. The Fermi surface. pp. 100-124. New York, John Wiley and Sons, Inc.

- Cohen, M., Harrison, M., and Harrison, W. A. (1960) Phys. Rev. 117, 937.
- Cohen, M. and Heine, V. (1961) Phys. Rev. 122, 1821.
- Condon, E. U. and Shortley, G. H. (1935) The theory of atomic spectra. New York, The Macmillan Company.
- Cotti, P., Luthi, B., and Olsen, J. L. (1962) Pulsed field magnetoresistance measurements in metals. In Kolm, Henry, Lax, Benjamin, Bitter, Frances, and Mills, Robert, eds. High magnetic fields. pp. 523-527. New York, John Wiley and Sons, Inc.
- Decker, D. L., Mapother, D. E., and Shaw, R. W. (1958) Phys. Rev. 112, 1888.
- Dhillon, J. S. and Shoenberg, D. (1955) Phil. Trans. Roy. Soc. (London) A249, 1.
- Dingle, R. B. (1952) Proc. Roy. Soc. (London) A211, 517.
- Falicov, L. M. and Heine, V. (1961) Advances in Physics 10, 57.
- Fawcett, E. (1955) Proc. Roy. Soc. A232, 519.
- Fawcett, E. (1960) Anomalous skin effect in aluminum. In Harrison, W. A. and Webb, M. B., eds. The Fermi surface. pp. 197-202. New York, John Wiley and Sons, Inc.
- Fawcett, E. (1961) Journal of Physics and Chemistry of Solids 18, 320.
- Fletcher, J. F. and Larson, D. C. (1958) Phys. Rev. 111, 455.
- Garcia-Moliner, F. (1958) Phil. Mag. 3, 207.
- General Radio Experimenter. (1961) 35, No. 7, 1. West Concord, Massachusetts, General Radio Company.
- Gell-Mann, M. (1957) Phys. Rev. 106, 367.
- Gold, A. V. (1958a) High field de Haas-van Alphen studies in lead. Unpublished Ph. D. thesis. Cambridge, England, Library, University of Cambridge.
- Gold, A. V. (1958b) Phil. Trans. Roy. Soc. (London) A251, 85.

- Gold, A. V. (1960) *Phil. Mag.* 5, 70.
- Gold, A. V. and Priestley, M. G. (1960) *Phil. Mag.* 5, 57.
- Ham, Frank S. (1960) Band calculations of the shape of the Fermi surface in the alkali metals. In Harrison, W. A. and Webb, M. B., eds. *The Fermi surface*. pp. 9-27. New York, John Wiley and Sons, Inc.
- Harrison, W. A. (1959) *Phys. Rev.* 116, 555.
- Harrison, W. A. (1960a) *Phys. Rev.* 118, 1182.
- Harrison, W. A. (1960b) *Phys. Rev.* 118, 1190.
- Harrison, W. A. (1960c) Electronic structure from the one-OPW or nearly-free-electron point of view. In Harrison, W. A. and Webb, M. B., eds. *The Fermi surface*. pp. 28-38. New York, John Wiley and Sons, Inc.
- Harrison, W. A. (1962) *Phys. Rev.* 126, 497.
- Harrison, W. A. and Webb, M. B. (1960) *The Fermi surface*. New York, John Wiley and Sons, Inc.
- Heine, V. (1957a) *Proc. Roy. Soc. (London)* A240, 340.
- Heine, V. (1957b) *Proc. Roy. Soc. (London)* A240, 354.
- Heine, V. (1957c) *Proc. Roy. Soc. (London)* A240, 361.
- Herman, Frank and Skillman, Sherwood (1962) *Bulletin of American Phys. Soc.* 7, 214.
- Herring, C. (1940) *Phys. Rev.* 57, 1167.
- Jones, H. (1960) *The theory of Brillouin zones and electronic states in crystals*. Amsterdam, North-Holland Publishing Company.
- Khaikin, M. S. and Mina, R. T. (1962) *Zhur. Eksp. i Teoret. Fiz.* 42, 35.
- Kip, A. F., Langenberg, D. N., and Moore, T. W. (1961) *Phys. Rev.* 124, 359.
- Kittel, C. (1956) *Introduction to solid state physics*. New York, John Wiley and Sons, Inc.
- Kohn, W. (1959) *Phys. Rev. Letters* 2, 393.

- Kohn, W. (1961) Phys. Rev. 123, 1242.
- Kondo, J. (1962) Progr. Theoret. Phys. (Kyoto) 27, 772.
- Kosevich, A. M. (1958) Soviet Physics, JETP 6, 564.
- Lax, Benjamin. (1958) Reviews of Modern Physics 30, 122.
- Lifshitz, I. M., Azbel, M. Ya., and Kaganov, M. I. (1957) Soviet Physics, JETP 4, 41.
- Lifshitz, I. M. and Kosevich, A. M. (1956) Soviet Physics, JETP 2, 636.
- Lifshitz, I. M. and Peschanski, V. G. (1959) Soviet Physics, JETP 8, 875.
- Lifshitz, I. M. and Pogorelov, A. V. (1954) Doklady Akad. Nauk, SSSR 96, 1143.
- Liu, L. (1962) Phys. Rev. 126, 317.
- Luthi, B. (1960) Helv. Phys. Acta 33, 161.
- Luttinger, J. M. (1960) Theory of the Fermi surface. In Harrison, W. A. and Webb, M. B., eds. The Fermi surface. pp. 2-8. New York, John Wiley and Sons, Inc.
- Luttinger, J. M. (1961) Phys. Rev. 121, 1251.
- Luttinger, J. M. and Ward, J. C. (1960) Phys. Rev. 118, 1417.
- Mackintosh, A. R. (ca. 1962) Proc. Roy. Soc. (London) - to be published. Ultrasonic attenuation in lead.
- Manley, R. G. (1945) Waveform analysis. New York, John Wiley and Sons, Inc.
- Mott, N. F. and Jones, H. (1958) The theory and properties of metals and alloys. New York, Dover Publications, Inc.
- Onsager, L. (1952) Phil. Mag. 43, 1006.
- Paskin, A. and Weiss, R. J. (1962) Phys. Rev. Letters 9, 199.
- Phillips, J. C. and Kleinman, L. (1959) Phys. Rev. 116, 287.

- Phillips, J. C. and Kleinman, L. (1960a) Phys. Rev. 117, 460.
- Phillips, J. C. and Kleinman, L. (1960b) Phys. Rev. 118,
1153.
- Piety, R. G. (1936) Phys. Rev. 50, 1173.
- Pines, David. (1955) Solid State Physics 1, 367.
- Pippard, A. B. (1957) Phil. Trans. Roy. Soc. (London) A250,
323.
- Pippard, A. B. (1960a) Proc. Roy. Soc. (London) A257, 165.
- Pippard, A. B. (1960b) Reports on Progress in Physics 23,
176.
- Pippard, A. B. (1961) The dynamics of conduction electrons.
In DeWitt, C., Dreyfus, B., and De Gennes, P. G., eds.
Low temperature physics: lectures delivered at Les
Houches Summer School of Theoretical Physics. pp. 1-146.
New York, Gordon and Breach, Science Publishers, Inc.
- Priestley, M. G. (1961) The de Haas-van Alphen effect at
high magnetic fields. Unpublished Ph. D. thesis.
Cambridge, England, Library, University of Cambridge.
- Quinn, John J. (1960) Electron-phonon interaction in normal
metals. In Harrison, W. A. and Webb, M. B., eds. The
Fermi surface. pp. 58-66. New York, John Wiley and
Sons, Inc.
- Rayne, J. A. (1962) Bulletin of the American Phys. Soc. 7,
223.
- Rayne, J. A. and Chandrasekhar, B. S. (1962) Phys. Rev. 125,
1952.
- Roaf, D. J. (ca. 1962) Phil. Trans. Roy. Soc. (London) - to
be published. The Fermi surfaces of copper, silver, and
gold, Part II: calculation of the Fermi surfaces.
- Segall, B. (1961) Phys. Rev. 124, 1797.
- Shoenberg, D. (1957) The de Haas-van Alphen effect. In
Gorter, C. J., ed. Progress in low temperature physics.
Vol. 2, pp. 226-265. New York, Interscience Publishers,
Inc.

- Shoenberg, D. (1960) The de Haas-van Alphen effect. In Harrison, W. A. and Webb, M. B., eds. The Fermi surface. pp. 74-83. New York, John Wiley and Sons, Inc.
- Shoenberg, D. (ca. 1962) Phil. Trans. Roy. Soc. (London) - to be published. The Fermi surfaces of copper, silver, and gold, Part I: the de Haas-van Alphen effect.
- Slater, J. C. (1956) The electronic structure of solids. In Flüge, S., ed. Handbuch der Physik. Vol. 19, pp. 1-136. Berlin, Springer-Verlag.
- Volkenshtein, N. V. and Fedorov, G. V. (1960) Soviet Physics, JETP 11, 48.
- Wallace, P. R. (1960) Solid State Physics 10, 1.
- White, G. K. (1962) Phil. Mag. 7, 271.
- Woll, E. J. and Kohn, W. (1962) Phys. Rev. 126, 1695.
- Woods, A. D. B., Cochran, W., and Brockhouse, B. N. (1960) Phys. Rev. 119, 980.
- Young, R. C. (ca. 1962) Phil. Mag. - to be published. Cyclotron resonances in lead at 36,000 mcs/sec.

10. ACKNOWLEDGEMENTS

The author wishes to express his gratitude to Dr. G. C. Danielson for initiating the entire Fermi surface Program and for his encouragement and suggestions, and to Dr. A. V. Gold for his suggestion of the problem and for his guidance throughout the course of this study.

Especial thanks are due to Mr. P. H. Sidles for help in design and construction of the dHvA apparatus and to Mr. O. Sevde, who kept everything working.

The author also wishes to thank Dr. W. A. Harrison for many stimulating and valuable discussions on the OPW approach and to thank Dr. J. M. Keller for explaining many concepts in physics and introducing him to the ideas of group theory. The author is also grateful to Dr. R. C. Young and Dr. A. R. Mackintosh for many useful suggestions and for the use of the drawing of the pipe model.

Especial thanks are due to Mr. R. F. Girvan for help in constructing equipment and taking data and to Mrs. Evelyn Blair for carrying out many of the calculations.

The work of Mr. R. C. Dillon in setting up the computer program is gratefully acknowledged. The author is also indebted to Mr. T. F. Stromberg, Mr. D. R. Torgeson, and Mr. D. J. Genin for help in coil calibration. The aid of Mr. R. A. Phillips, Mr. P. T. Panousis, Mr. Stewart Keaton, and Mr. D.

R. Stone in carrying out the calculations and taking data is sincerely appreciated.

11. APPENDIX

11.1. Appendix A: Determination of Constant Energy Curves Near U

An OPW at U (Figure 4.1) has the same energy as two other OPW's whose wave vectors differ by the reciprocal lattice vectors $(0, 0, 2)$ and $(1, 1, 1)$.¹ The wave vectors of these three OPW's are:

$$\begin{aligned}\underline{K}_1 &= \left(\frac{1}{4}, \frac{1}{4}, 1\right) \\ \underline{K}_2 &= \underline{K}_1 - (0, 0, 2) = \left(\frac{1}{4}, \frac{1}{4}, -1\right) \\ \underline{K}_3 &= \underline{K}_1 - (1, 1, 1) = \left(-\frac{3}{4}, -\frac{3}{4}, 0\right)\end{aligned}\tag{11.1}$$

$$\text{where } K_1^2 = K_2^2 = K_3^2 = K^2.$$

In the limit that the pseudopotential goes to zero, these three OPW's would be degenerate and consequently they are the only ones considered near U.

An OPW of wave vector $\underline{k} + \underline{K}_1$, $\underline{k} = (k_x, k_y, k_z)$, in the region near U is connected by the same reciprocal lattice vectors to two other OPW's having nearly the same energy. Mixing with any other states is neglected and the procedure of Harrison (1960a) is followed to write the Hamiltonian

¹All wave vectors in Appendices A, B, and C have been divided by $2\pi/a$.

matrix as:

$$H = \begin{pmatrix} T(\underline{k} + \underline{K}_1) & V'_{200} & V'_{111} \\ V'_{200} & T(\underline{k} + \underline{K}_2) & V'_{111} \\ V'_{111} & V'_{111} & T(\underline{k} + \underline{K}_3) \end{pmatrix} \quad (11.2)$$

$T(\underline{k})$ is assumed to be spherically symmetric and is written in the form $T(\underline{k}) = (\hbar^2/2m)(2\pi/a)^2 k^2$ as for free electrons (Chapter 5). Thus the Hamiltonian matrix 11.2 can be rewritten with these assumptions as:

$$H = \begin{pmatrix} (\underline{k} + \underline{K}_1)^2 & V_{200} & V_{111} \\ V_{200} & (\underline{k} + \underline{K}_2)^2 & V_{111} \\ V_{111} & V_{111} & (\underline{k} + \underline{K}_3)^2 \end{pmatrix} \quad (11.3)$$

where $(\hbar^2/2m)(2\pi/a)^2$ has been divided out of every matrix element; the shape of the Fermi surface is independent of this quantity.

The matrix 11.3 can be reduced to a slightly simpler form by a similarity transformation which takes account of the symmetry when $\underline{k} = 0$, i.e. at U. This gives

$$H' = SHS^{-1} \quad (11.4)$$

$$= \begin{pmatrix} K^2 + \underline{k}^2 + \frac{k_x + k_y}{2} + V_{200} & \sqrt{2}V_{111} & 2ik_z \\ \sqrt{2}V_{111} & K^2 + \underline{k}^2 - \frac{3}{2}(k_x + k_y) & 0 \\ -2ik_z & 0 & K^2 + \underline{k}^2 + \frac{k_x + k_y}{2} - V_{200} \end{pmatrix},$$

where

$$S = \frac{\sqrt{2}}{2} \begin{pmatrix} 1 & 1 & 0 \\ 0 & 0 & \sqrt{2} \\ -1 & 1 & 0 \end{pmatrix} \quad (11.5)$$

For an expansion in the $k_x = k_y$ plane, for example, we set $k_x = k_y = k$ and the secular determinant to be solved for the intersection of this plane with the constant energy surfaces is given by:

$$\begin{vmatrix} K^2 + 2k^2 + k_z^2 + k + V_{200} - E & \sqrt{2}V_{111} & 2ik_z \\ \sqrt{2}V_{111} & K^2 + 2k^2 - 3k + k_z^2 - E & 0 \\ -2ik_z & 0 & K^2 + 2k^2 + k + k_z^2 - V_{200} - E \end{vmatrix} = 0 \quad (11.6)$$

In special cases Equation 11.6 can be factored, but in general the result is a cubic equation:

$$\begin{aligned}
F(w, k) &= w^3 + w^2(-4 - 3C - k + 6k^2) + w[3C^2 + 4C - (V_{200}^2 \\
&\quad + 2V_{111}^2) + k(12 + 2C) + k^2(-12C - 13) - 4k^3 \\
&\quad + 12k^4] + C(V_{200}^2 + 2V_{111}^2) - C^3 + 2V_{111}^2 V_{200} \\
&\quad + k(-C^2 - 2V_{111}^2 + 3V_{200}^2) + k^2(5C + 6C^2 - 2V_{200}^2 \\
&\quad - 4V_{111}^2) + k^3(-3 + 4C) + k^4(-10 - 12C) - 4k^5 \\
&\quad + 8k^6 \\
&= 0, \tag{11.7}
\end{aligned}$$

$$\text{where } w = k_z^2 \text{ and } C = E - k^2.$$

This cubic equation can be solved for w as a function of k for fixed C to give sections of the constant energy surfaces normal to the $[110]$ direction. This was initially done by hand for a few cases and later programmed for the IBM 704. The area \star and effective mass ratio $(\hbar^2/2\pi)(\partial\star/\partial E)$ were calculated for different values of V_{111} , V_{200} , and C . All energies are given in calculation units CU where the Fermi energy for four free electrons per atom becomes 1.538 CU. If the free electron mass is chosen, 1 CU = 0.454 ry.

Figure 11.1 shows a sample plot of these results. Only results for $k_z \geq 0$ are shown, but a complete plot would be symmetric with respect to the axis of the abscissae. Curve I with its mirror image corresponds to a small closed cross-section through an arm in the third zone (orbit ζ). This area was one of the two used in fitting to the dHvA data (Section

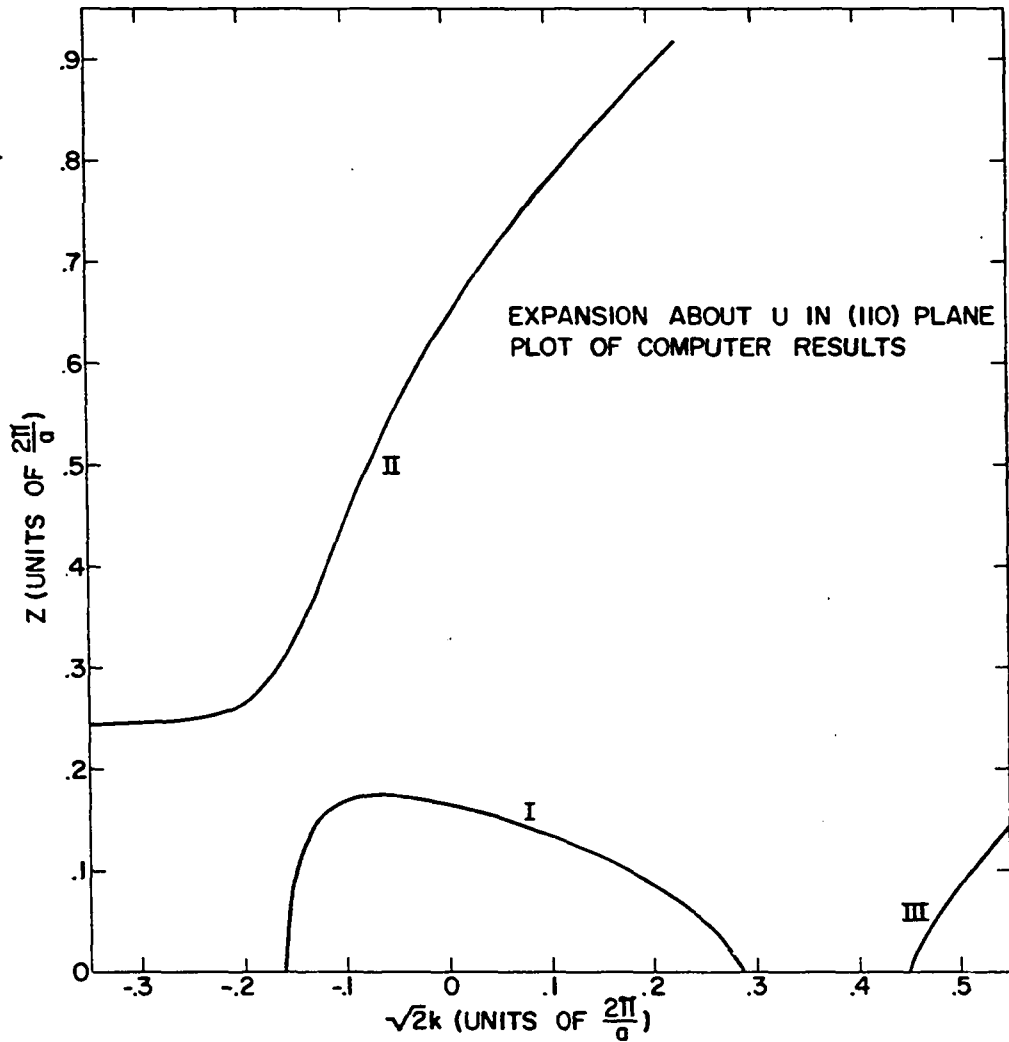


Figure 11.1. Plot of second-band and third-band constant energy surfaces for a (110) section through Γ
 $|V_{111}| = 0.10$ CU, $V_{200} = 0.11$ CU,
 $C = 0.413$ CU

5.4) Curves II and III of Figure 11.1 are boundaries of the second-zone hole surface.

A similar calculation in (110) planes is possible about any point P on the line U - W (Figure 4.1). Equation 11.7 can still be used if E is replaced by $E' = E - 2\gamma^2$ and $C = E' - k^2$. $\sqrt{2} \gamma$ is the distance to P along the line U - W measured from U. This same substitution can be used to find the associated cyclotron mass ratio. At W, as will be discussed in Appendix B, a fourth OPW is included in the expansion. The inclusion of this fourth OPW becomes important as γ approaches 0.25. Even with the use of the computer inclusion of the fourth state in the Hamiltonian 11.2 would have complicated the calculations considerably, and so only three states were kept for simplicity.

Along the line U - W the energy levels were found from Equation 11.6 by setting $k_z = 0$. The resulting energy levels are:

$$\begin{aligned} E_1 &= k^2 + 2\gamma^2 - V_{200} \\ E_2 &= k^2 + 2\gamma^2 + V_{200}/2 - ((V_{200}/2)^2 + 2V_{111}^2)^{1/2} \\ E_3 &= k^2 + 2\gamma^2 + V_{200}/2 + ((V_{200}/2)^2 + 2V_{111}^2)^{1/2} \end{aligned}$$

The energy levels were also calculated along the line U - W with the addition of a fourth OPW, $K_4 = \underline{k} + \underline{K}_1 - (1, -1, 1)$. Both the four OPW results and the three OPW results are shown in Figure 11.2 for two sets of parameters V_{111} and V_{200} chosen

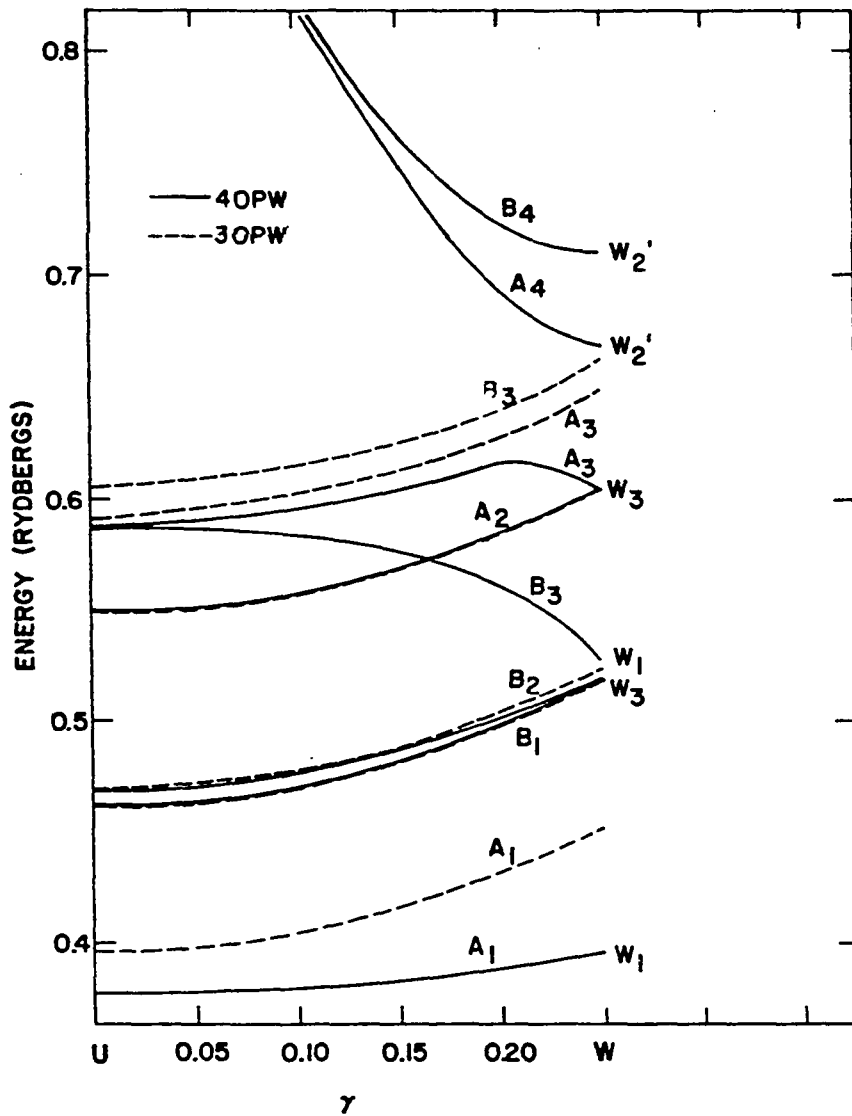


Figure 11.2. $E(\underline{k})$ curves along the symmetry line U - W

to obtain the best fit to two observed dHvA periods (Chapter 5). The discrepancy in the third-band energy at U arising from the use of three OPW's rather than four is roughly 0.002 ry for model A and 0.01 ry for model B; the calculated cross-section of an arm is too large when only three OPW's are used. In order to obtain the required area an increase of roughly 0.001 ry (model A) or 0.008 ry (model B) in each matrix element would be necessary, but the increase would change the shapes of the constant energy surfaces very little. We have therefore made no correction for this difference and the four OPW energy curve was shifted to fit the three OPW value at U; this in turn left a small discrepancy at W. Then the difference between the three OPW and four OPW energies $\Delta E_3(P)$ was used to estimate the effect of the fourth OPW on the shape of the constant energy surfaces. It was assumed that the energies of the third-band states in a (110) plane containing P were also shifted by $\Delta E_3(P)$. This gave for each point P new values of C to be used in Equation 11.7 as given below:

γ	Model A		Model B	
	C(CU)	$\star(\gamma)$	C(CU)	$\star(\gamma)$
0	0.413	0.110	0.413	0.113
0.05	0.410	0.108	0.416	0.115
0.10	0.398	0.100	0.420	0.117
0.15	0.378	0.0883	0.433	0.126
0.20	0.358	0.0767	0.473	0.155
0.25	0.378	0.0883	0.543	0.205

($\star(\gamma)$) is also given in units of $(2\pi/a)^2$ and shows the taper-

ing predicted by model A.) In this manner the approximate shape of the arm could be determined in the vicinity of U. The second-band hole surface was changed very little by the addition of the fourth OPW and no correction was necessary.

The contribution from each Bragg plane (matrix element $V_{\underline{K}}$) as included by second order perturbation theory lowers the energy of a state. If, for example, we consider orbit ζ , the energy at U is lowered and so for fixed E_F , $\star \zeta$ will be increased; this can be considered approximately equivalent to holding the state energy fixed (at U) and effectively raising E_F . On the other hand, if we consider the electron gas as a whole, the effect on the Fermi energy due to $V_{\underline{K}}$ is a decrease given by second-order perturbation theory as:

$$\frac{\delta E_F}{E_{F_0}} \approx -\frac{1}{8} \left| \frac{V_{\underline{K}}}{E_{F_0}} \right|^2 \kappa \ln \left| \frac{1+\kappa}{1-\kappa} \right| \text{ for } |\underline{K}| \neq 2k_F, \quad (11.10)$$

where $\kappa = \left| \frac{2k_F}{K} \right|$, k_F is the radius of the Fermi sphere,

and E_{F_0} is the free-electron Fermi energy.

These two effects tend to cancel each other although the first is larger. Therefore, the shift in the Fermi energy is neglected for Bragg planes omitted from the calculation. If two Bragg planes are considered as in the Hamiltonian matrix 11.2, Equation 11.10 implies a correction of the order of 0.4% to the Fermi energy. Again this decrease in Fermi energy would

make a small change in the values chosen for the matrix elements, but would have little effect upon the shape of the Fermi surface, and therefore the calculation has been made neglecting this decrease.

The results of this calculation give the cross-sectional area determined by the orbit ζ on the third-band surface and also part of the second-band hole surface as functions of V_{111} and V_{200} .

11.2. Appendix B: Determination of Constant Energy Curves about W

To find constant energy curves in the neighborhood of W, four OPW's are considered, since four free-electron states are degenerate at W. At W the OPW's considered have wave vectors given by

$$\begin{aligned}
 \underline{k}_{W1} &= (1/2, 0, 1) \\
 \underline{k}_{W2} &= \underline{k}_{W1} - (0, 0, 2) = (1/2, 0, -1) \\
 \underline{k}_{W3} &= \underline{k}_{W1} - (1, 1, 1) = (1/2, -1, 0) \\
 \underline{k}_{W4} &= \underline{k}_{W1} - (1, -1, 1) = (1/2, 1, 0)
 \end{aligned}
 \tag{11.11}$$

where

$$k_{W1}^2 = k_{W2}^2 = k_{W3}^2 = k_{W4}^2 = k_W^2$$

In an expansion around W an OPW corresponding to $\underline{k}_{W1} + \underline{k}$ and three other OPW's related by the reciprocal lattice vectors above are considered. Then the Hamiltonian matrix be-

comes:

$$H = \begin{pmatrix} T(\underline{k} + \underline{k}_{w1}) & V_{200} & V_{111} & V_{111} \\ V_{200} & T(\underline{k} + \underline{k}_{w2}) & V_{111} & V_{111} \\ V_{111} & V_{111} & T(\underline{k} + \underline{k}_{w3}) & V_{200} \\ V_{111} & V_{111} & V_{200} & T(\underline{k} + \underline{k}_{w4}) \end{pmatrix} \quad (11.12)$$

As before a simpler form is obtained if a similarity transformation is made:

$$H' = SHS^{-1} \quad (11.13)$$

$$= \begin{pmatrix} k_w^2 + k^2 + 2V_{111} + V_{200} & k_x & \sqrt{2}ik_z & -\sqrt{2}ik_y \\ k_x & k_w^2 + k^2 - 2V_{111} + V_{200} & \sqrt{2}ik_z & \sqrt{2}ik_y \\ -\sqrt{2}ik_z & -\sqrt{2}ik_z & k_w^2 + k^2 + k_x & 0 \\ \sqrt{2}ik_y & -\sqrt{2}ik_y & 0 & k_w^2 + k^2 - k_x - V_{200} \end{pmatrix}$$

Here $\underline{k}^2 = k_x^2 + k_y^2 + k_z^2$

and

$$S = 1/2 \begin{pmatrix} 1 & 1 & 1 & 1 \\ 1 & 1 & -1 & -1 \\ -i\sqrt{2} & i\sqrt{2} & 0 & 0 \\ 0 & 0 & -i\sqrt{2} & i\sqrt{2} \end{pmatrix} \quad (11.14)$$

At W ($k_x = k_y = k_z = 0$), the eigenvalues are:

$$\begin{aligned} E_1 &= K_w^2 + V_{200} + 2V_{111} \\ E_{2,3} &= K_w^2 - V_{200} \quad (\text{doubly degenerate}) \\ E_4 &= K_w^2 + V_{200} - 2V_{111} \end{aligned} \quad (11.15)$$

For non-zero \underline{k} the secular determinant obtained from H' can be factored only for some special values such as $k_x = 0$ or $k_y = 0$. In order to obtain the 'windmill' orbit ν in a (100) plane, we set $k_x = 0$. This gives a quartic equation which can be solved for k_y^2 as a function of k_z^2 or vice versa:

$$\begin{aligned} G(u, w) &= u^4 + 4u^3(w - B - 1) + 2u^2[3w^2 + 6w(-B - 1) + 4B \\ &\quad + 3B^2 - V_{200}^2 - 2V_{111}^2] + 4u[w^3 - 3w^2(B + 1) \\ &\quad + w(4 + 4B + 3B^2 - V_{200}^2 - 2V_{111}^2) - B^3 - B^2 \\ &\quad + B(V_{200}^2 + 2V_{111}^2) + 2V_{111}^2 V_{200} + V_{200}^2] + w^4 \\ &\quad - 4w^3(B + 1) + 2w^2(4B + 3B^2 - V_{200}^2 - 2V_{111}^2) \\ &\quad + 4w[-B^2 - B^3 + B(V_{200}^2 + 2V_{111}^2) + 2V_{111}^2 V_{200} \\ &\quad + V_{200}^2] + B^4 - 2B^2(V_{200}^2 + 2V_{111}^2) - 8BV_{111}^2 V_{200} \\ &\quad + V_{200}^4 - 4V_{111}^2 V_{200}^2 \\ &= 0 \end{aligned} \quad (11.16a)$$

where $u = k_y^2$, $w = k_z^2$; and $B = E - K_w^2$. $B = 0.288$ CU for a sphere corresponding to four conduction electrons.

V_{111} , V_{200} , and B were treated as parameters and Equation 11.16 was solved for u as a function of w . Figure 11.3 shows a sample plot of these results. In this example the fourth-zone pockets of electrons are absent since they disappear for

$$V_{200} + 2 |V_{111}| > B \quad (11.17)$$

For the 'dogbone' orbit w normal to the $[011]$ direction we set $k_y = -k_z$ in the secular equation resulting from H' (Equation 11.13) and solve the quartic equation:

$$\begin{aligned} H(w, x) = & w^4 + 4w^3(x^2 - C - 1) + w^2 [6x^4 + x^2(-12C - 10) \\ & + 80 + 6C^2 + 4 - 2V_{200}^2 - 4V_{111}^2] + 4w[x^6 \\ & + x^4(-3C - 2) + x^2(3C + 3C^2 - 1 - V_{200}^2 - 2V_{111}^2) \\ & - C^3 - C^2 + V_{200}^2 C + 2V_{111}^2 C + 2V_{111}^2 V_{200} + V_{200}^2] \\ & + x^8 + 2x^6(-2C - 1) + x^4(6C^2 + 4C + 1 - 2V_{200}^2 \\ & - 4V_{111}^2) + x^2(-2C^2 - 4C^3 + 4V_{200}^2 C + 8V_{111}^2 C \\ & + 8V_{111}^2 V_{200} - 2V_{200}^2 + 4V_{111}^2) + C^4 - 2V_{200}^2 C^2 \\ & + V_{200}^4 - 4V_{111}^2 C^2 - 8CV_{111}^2 V_{200} - 4V_{111}^2 V_{200}^2 \\ & = 0 \end{aligned} \quad (11.16b)$$

where $w = 2z^2$ and $x = k_x$.

Figure 11.4 shows a sample plot of these results. Notice that the fourth-zone pockets of electrons at W have appeared as predicted by 11.17.

Figure 11.3. Plot of second-band and third-band constant energy surfaces for a (100) section which contains orbit ν
 $|V_{111}| = 0.10 \text{ CU}$, $V_{200} = 0.11 \text{ CU}$,
 $B = 0.288 \text{ CU}$

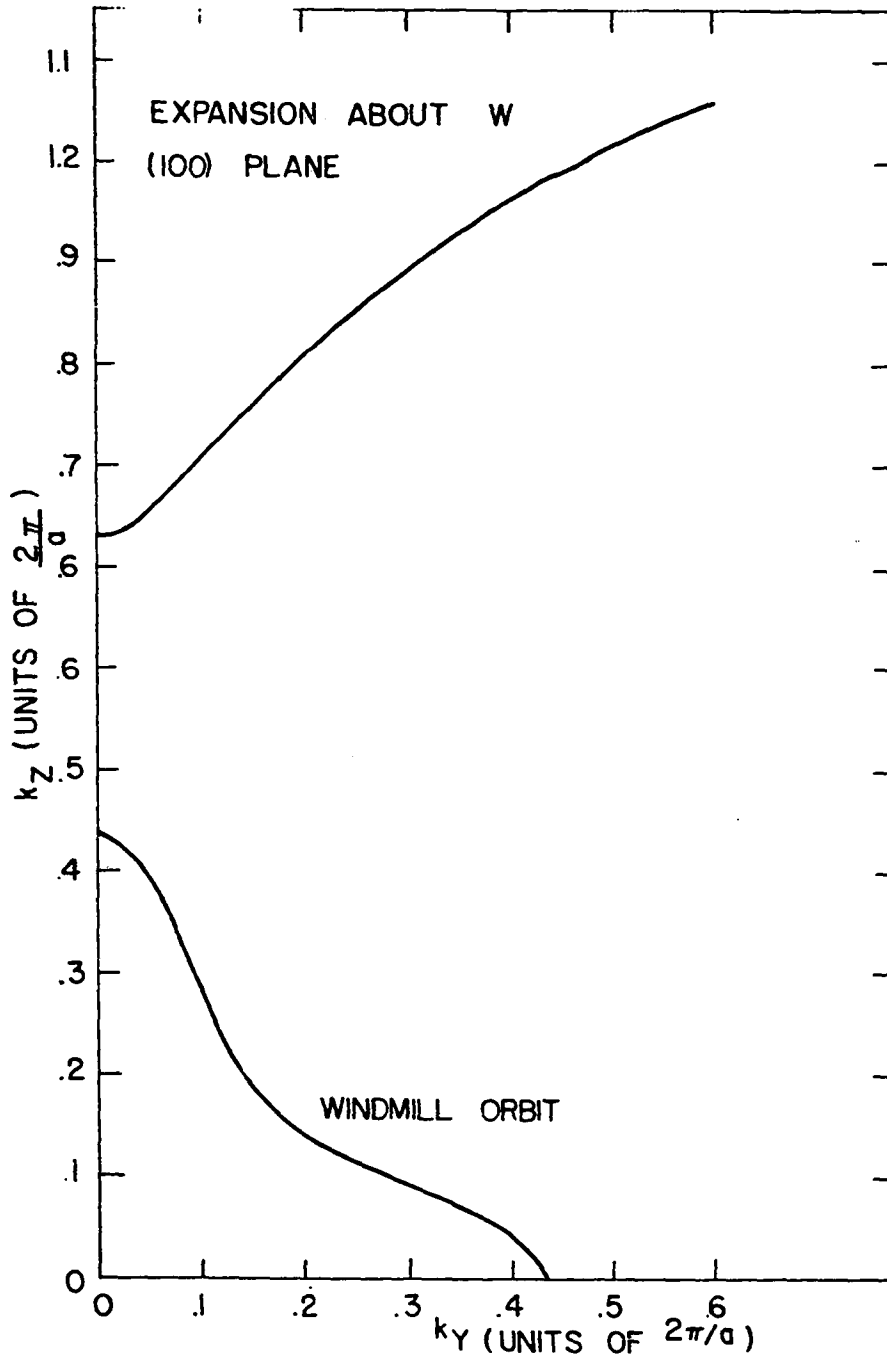
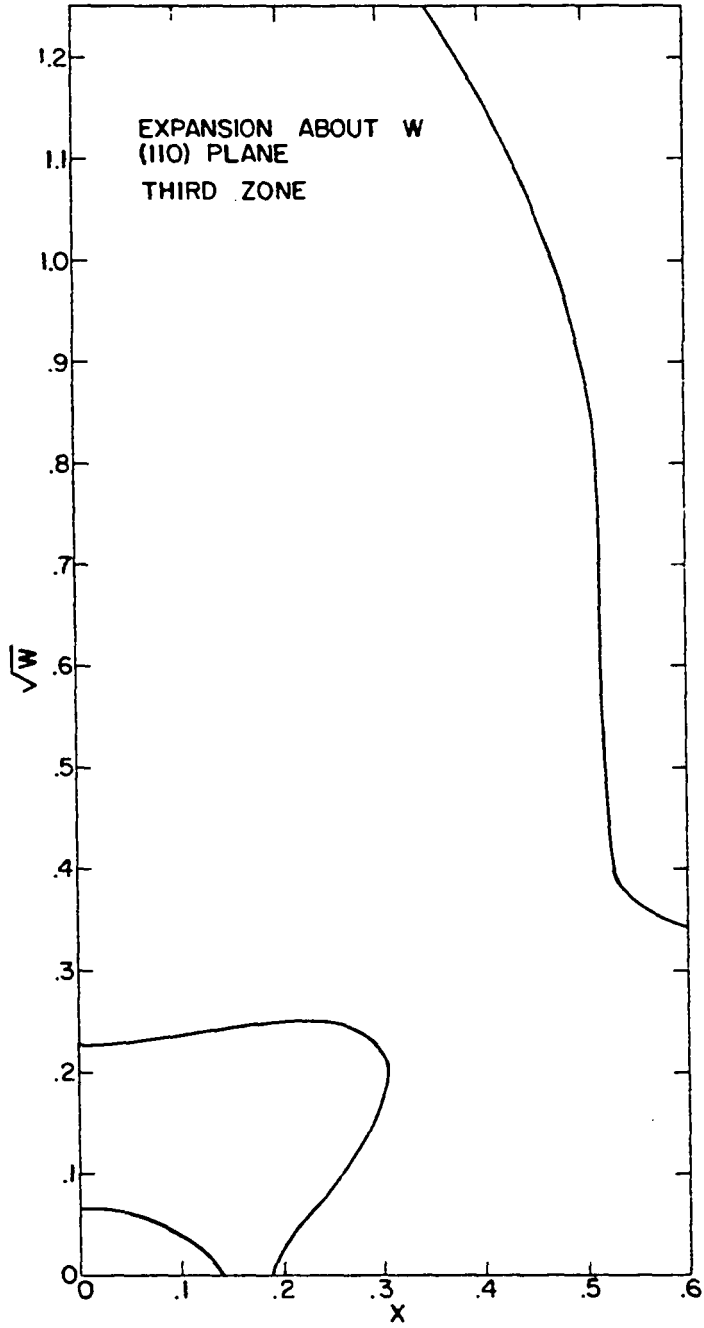


Figure 11.4. Plot of second-band and third-band energy surfaces for a (110) section which contains orbit W
 $|V_{111}| = 0.155 \text{ CU}$, $V_{200} = -0.070 \text{ CU}$,
 $B = 0.288 \text{ CU}$



11.3. Appendix C: Spin-Orbit Coupling

The spin-orbit coupling term in the Hamiltonian has the form (cf. Jones 1960, p. 247)

$$H_{so} = \frac{\hbar}{4m^2c^2} (\nabla V \times p) \cdot \underline{\sigma} \quad (11.18)$$

which becomes for free atoms:

$$H_{so} = \frac{1}{2m^2c^2} \left(\frac{1}{r} \frac{\partial V(r)}{\partial r} \right) \underline{L} \cdot \underline{S} = \xi(r) \underline{L} \cdot \underline{S} \quad (11.19)$$

Condon and Shortley (1935, p. 237) give for the one electron atomic parameters in cm^{-1} :

	Ge	Sn	Pb
ξ_{nl}	880.1	2097.3	7294

where

$$\xi_{nl} = \hbar^2 \int_0^{\infty} R_{nl}^2(r) \xi(r) r^2 dr, \quad (11.20)$$

and R_{nl} is the radial part of the wave function. Thus the spin-orbit interaction increases with atomic number and is important in lead ($= 0.066$ ry); it should therefore not be neglected in a complete band calculation.

In our case, where the matrix elements are estimated by fitting to de Haas-van Alphen effect data, it is difficult to know how to include this interaction. It is probably reasonable to take the atomic spin-orbit interaction as a first approximation in the crystal, since the main contribution

occurs near the ion cores where the wave functions should be similar to those of the free atom and the potential is spherically symmetric if overlap is neglected. However, Liu (1962) has suggested that the splitting may be enhanced over that in the atom because the conduction electron wave function is larger near the ion cores due to normalization within the unit cell.

In order to include spin effects in the OPW equations we consider

$$H = T + V + V^{SO} \quad (11.21)$$

where V is the same potential function considered in Chapter 5 and V^{SO} is the spin-orbit interaction. With this addition Equation 5.10 becomes:

$$\langle \phi_{\underline{k}}^{K'} | T + V^p | \theta_{\underline{k}} \rangle + \langle \psi_{\underline{k}}^{K'} | V^{SO} | \chi_{\underline{k}} \rangle = E_{\underline{k}} \langle \phi_{\underline{k}}^{K'} | \theta_{\underline{k}} \rangle \quad (11.22)$$

Substituting

$$\chi_{\underline{k}} = \sum_{\underline{K}} c_{\underline{k}}^{\underline{K}} \psi_{\underline{k}}^{\underline{K}} \quad \text{and} \quad \theta_{\underline{k}} = \sum_{\underline{K}} c_{\underline{k}}^{\underline{K}} \phi_{\underline{k}}^{\underline{K}}$$

into Equation 11.22, we obtain

$$\sum_{\underline{K}} c_{\underline{k}}^{\underline{K}} (T_{\underline{K}\underline{k}}^{\underline{k}} + V_{\underline{K}\underline{k}}^{p\underline{k}}) + \sum_{\underline{K}} c_{\underline{k}}^{\underline{K}} V_{\underline{K}\underline{k}}^{SO\underline{k}} = E_{\underline{k}} c_{\underline{k}}^{\underline{K}'} \quad (11.23)$$

where

$T_{\underline{K}\underline{K}'}^{\underline{k}} + V_{\underline{K}\underline{K}'}^{p\underline{k}}$, is defined in Equation 5.12 as

$$T_{\underline{K}\underline{K}'}^{\underline{k}} + V_{\underline{K}\underline{K}'}^{p\underline{k}} = \left(\phi_{\underline{k}}^{\underline{K}'} \mid T + V^p \mid \phi_{\underline{k}}^{\underline{K}} \right),$$

and

$$V_{\underline{K}\underline{K}'}^{so\underline{k}} = \left(\phi_{\underline{k}}^{\underline{K}'} \mid V^{so} \mid \phi_{\underline{k}}^{\underline{K}} \right). \quad (11.24)$$

Equation 11.23 is now in a form in which the spin-orbit interaction can be introduced. $V_{\underline{K}\underline{K}'}^{p\underline{k}}$, are assumed to depend only on $\underline{K} - \underline{K}'$ (Chapter 5). The spin-orbit matrix elements are written with the entire OPW as basis element and we assume that near the ion cores (where the spin-orbit interaction is most important) the OPW's are like the free atom wave functions which are orthogonal to the core wave functions.

The problem in this calculation, where no wave functions are actually obtained, is to decide what spherical harmonics are contained in the OPW's or what spherical harmonics to associate with a particular value of \underline{k} . Segall (1961) has computed for his wave functions for aluminum the ratios of the p and d components to the s components at the surface of the sphere inscribed in the Wigner-Seitz cell. These are compared with the corresponding quantities for the nearly free electron case. He finds good agreement and his results indicate that the p and d contributions are roughly the same. This result actually depends upon the radius at which the comparison is made and is arbitrary to that extent.

In lead, for simplicity, we ignore the d contribution and consider only s and p components. We assume our OPW's are orthogonalized to the atomic wave functions and near the ion cores are of the form of the next higher atomic states (in lead 6s and 6p). We also require that the wave function assumed near the ion core be a basis vector of the group of \underline{k} . The same number of states are considered as were considered when spin-orbit coupling was neglected. The wave functions near the core are chosen as a combination of a p function directed along \underline{k} with sufficient s function to allow normalization and orthogonalization to the other degenerate or nearly-degenerate states. These atomic wave functions were combined with spin functions and the results used to suggest the spin-orbit contribution to the $E(\underline{k})$ curves.

For example, for two OPW's with wave vectors $\underline{K}_1 = (k_x, 0, 1)$ and $\underline{K}_2 = \underline{K}_1 - (0, 0, 2) = (k_x, 0, -1)$ the space parts of the wave functions used in calculating the spin-orbit term were assumed to have the form:

$$\begin{aligned}\psi_1 &= A(r) + B(r)\{-Y_1^0 \cos \theta + \frac{\sin \theta}{\sqrt{2}} (Y_1^1 - Y_1^{-1})\} \\ \psi_2 &= -A(r) + B(r)\{-Y_1^0 \cos \theta - \frac{\sin \theta}{\sqrt{2}} (Y_1^1 - Y_1^{-1})\}\end{aligned}\tag{11.25}$$

where

$$\int A^2(r)r^2 dr = \cos 2\theta \int B^2(r)r^2 dr,\tag{11.26}$$

and

$$\int A^2(r)r^2 dr + \int B^2(r)r^2 dr = 1,$$

$\theta = \tan^{-1}(k_x)$, and the Y_l^m are spherical harmonics. In this case the introduction of the spin-orbit interaction leads to a Hamiltonian matrix of the form

$$\begin{pmatrix} T(\underline{K}_1) & V_{200} & 0 & -Q/2 \\ V_{200} & T(\underline{K}_1) & Q/2 & 0 \\ 0 & Q/2 & T(\underline{K}_1) & V_{200} \\ -Q/2 & 0 & V_{200} & T(\underline{K}_2) \end{pmatrix} \quad (11.27)$$

where

$$Q = \sin 2\theta \int \xi B^2 dr = \tan \theta \xi_p \quad (11.28)$$

(ξ_p is the atomic parameter for lead).

This matrix is equivalent to the matrix obtained by making a Hermitean 2×2 matrix into two real matrices and therefore the 4×4 matrix has the same eigenvalues as

$$H = H_t + H_{so} = \begin{pmatrix} T(\underline{K}_1) & V_{200} + iQ \\ V_{200} - iQ & T(\underline{K}_2) \end{pmatrix} \quad (11.29)$$

Since off-diagonal elements are complex conjugates, we may treat this two-OPW case with spin-orbit coupling considering only

$$\begin{pmatrix} T(\underline{K}_1) & V_{200}^+ \\ V_{200}^+ & T(\underline{K}_2) \end{pmatrix}$$

and adjusting the values of V_{200}^+ to fit the data. $V_{200}^+ = |V_{200} + iQ|$, where this is taken as some average value over the region of interpolation.

In a similar manner an estimate of the effect of the spin-orbit term for 3 OPW's was made along the line U - W. However, here it was not possible to relate the results to the two real matrices obtained from a 3 x 3 Hermitean matrix, although the resulting 6 x 6 matrix factored into a 3 x 3 matrix and its complex conjugate.

The 3 x 3 matrix was written as

$$H = H_t + H_{so}$$

$$= \begin{pmatrix} P^2 + V_{200} & \sqrt{2}V_{111} + iF_1 & -iF_2 \\ \sqrt{2}V_{111} - iF_1 & P^2 & -iF_3^* \\ iF_2^* & iF_3 & P^2 - V_{200} \end{pmatrix} \quad (11.30)$$

where

$$P^2 = K^2 + 2\gamma^2 \quad 0 \leq \gamma \leq 4$$

$$U \rightarrow W.$$

$$F_1 = 1/2 \tan \beta \sin 2\alpha \left(\frac{\cos 2\beta}{1 - \sin^2 \beta (1 + \sin^2 2\alpha)} \right)^{1/2} \xi_p,$$

$$F_2 = \frac{e^{-i\alpha}}{2} \tan \beta \xi_p, \quad (11.31)$$

and

$$F_3 = \frac{e^{-i\alpha}}{2} \left(\frac{\cos 2\beta}{1 - \sin^2\beta(1 + \sin^2 2\alpha)} \right)^{1/2} \xi_p.$$

Here

$$\begin{aligned} \alpha &= \pi/4 - \tan^{-1}(2\sqrt{2}\gamma) & 0 \leq \alpha \leq \pi/4 \\ \text{and} \quad \beta &= \tan^{-1}(2\gamma^2 + 1/8)^{1/2} & 0 \leq \beta \leq \pi/4. \end{aligned} \quad (11.32)$$

Figures 11.5 and 11.6 show a plot of energy versus wave number along $U - W$ derived from the secular determinant obtained from the Hamiltonian matrix 11.30 for several values of the lattice potential. The atomic spin-orbit parameter $\xi_p = 0.066$ ry (page 225) has been assumed for this calculation. For comparison $E(\underline{k})$ curves for which $\xi_p = 0$ are shown on the same graph. Although the spin-orbit parameter is of comparable magnitude to the matrix elements of the lattice potential, the shapes of the curves are modified very little by the addition of ξ_p . In fact a particular $E(\underline{k})$ curve for $\xi_p = 0$ can be fitted quite closely for $\xi_p \neq 0$ if V_{111} and V_{200} are changed. In this calculation the third-band surface was used for fitting and addition of the spin-orbit term should not alter the shape appreciably although the band gaps would be changed.

At W four OPW's have been used to determine the energy levels as a function of the spin-orbit coupling parameter. This additional interaction splits the doubly-degenerate level, an especially important modification if the highest level were degenerate. However, for the parameter values chosen for this

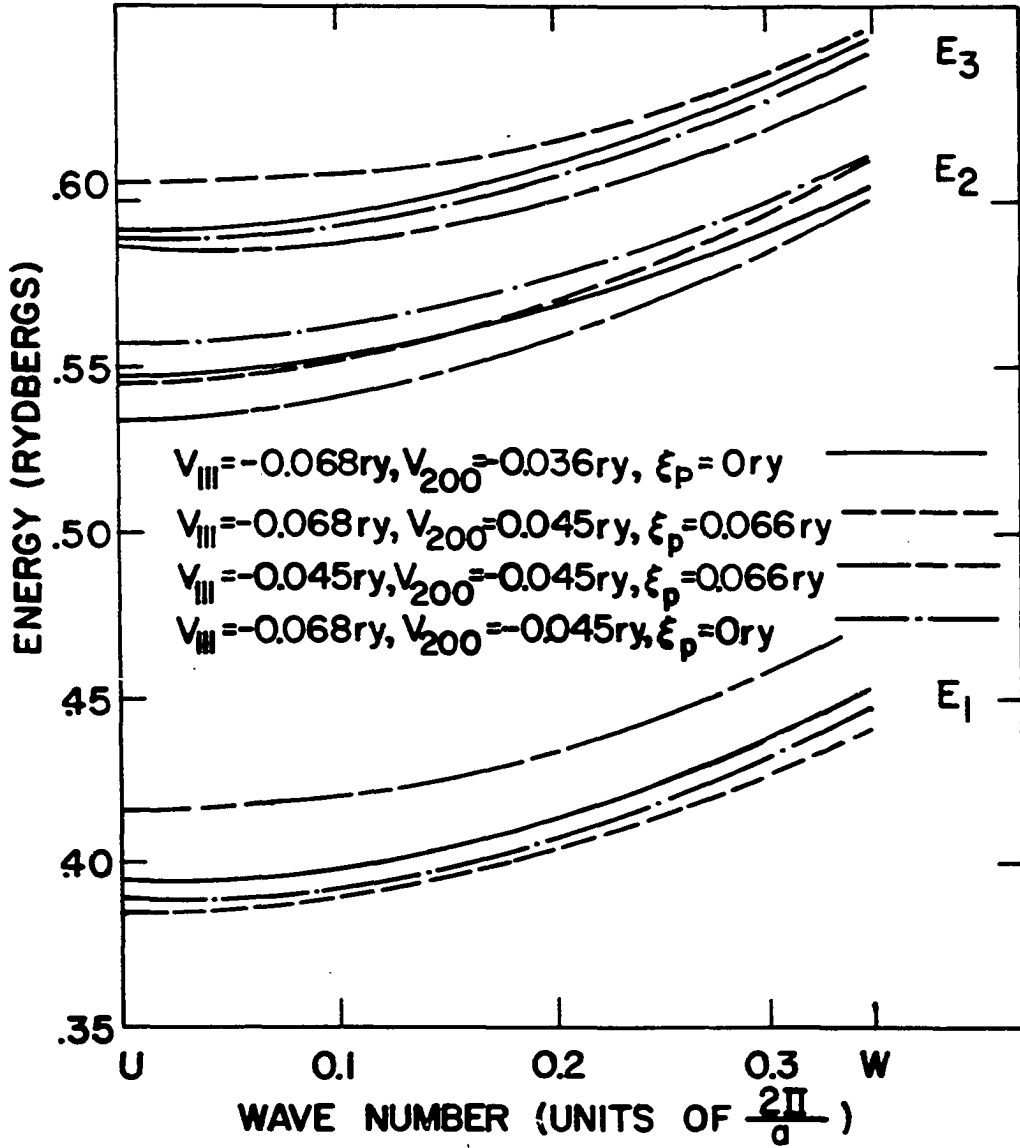


Figure 11.5. $E(\underline{k})$ along the symmetry line U - W showing the effect of spin-orbit coupling

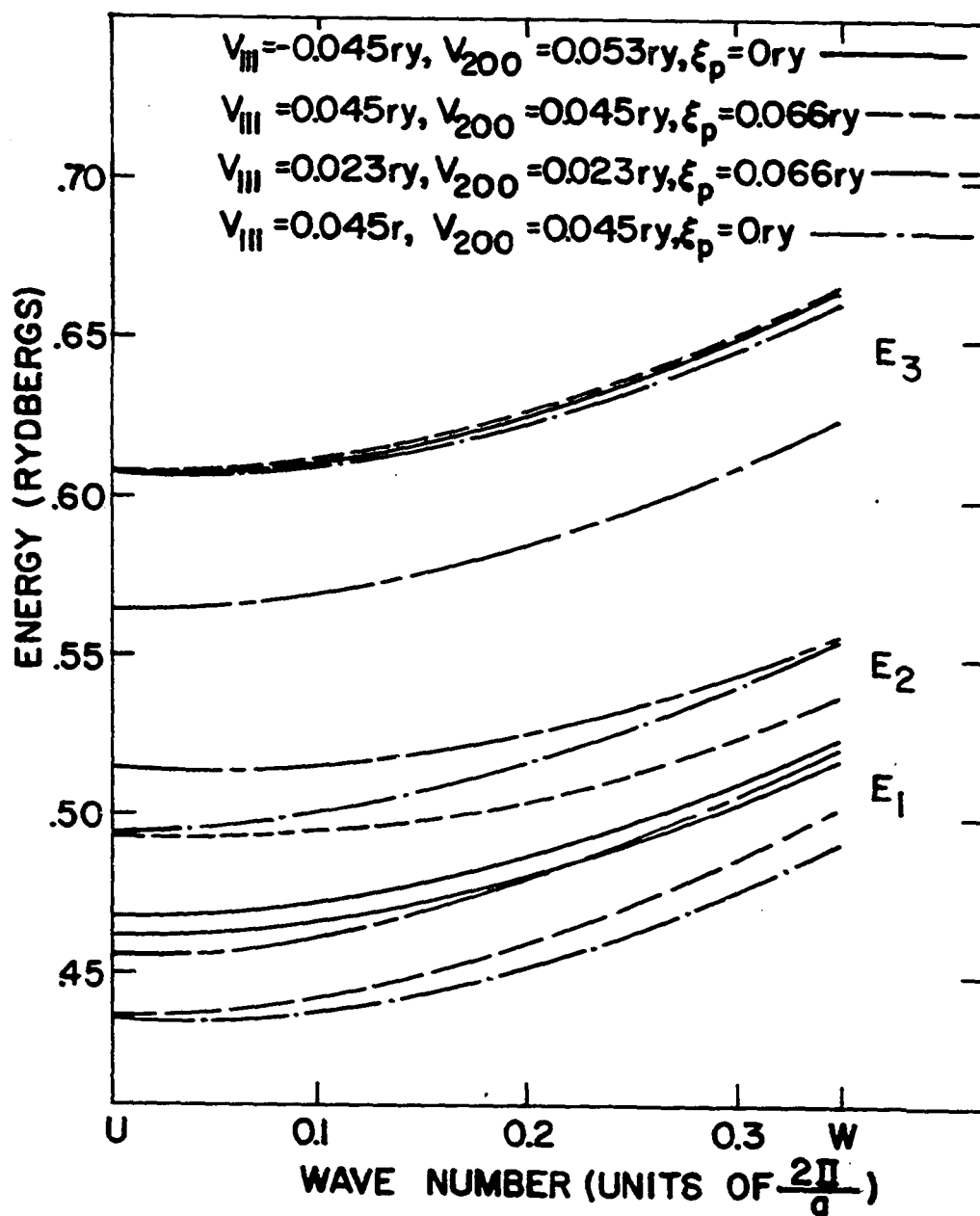


Figure 11.6. $E(\underline{k})$ along the symmetry line U - W showing the effect of spin-orbit coupling

calculation, the separation between third and fourth bands is changed very little as can be seen in Figure 11.7. The fourth band energy at W increases as the value of the coupling parameter is increased; this suggests that for model A for a reasonable choice for this parameter the fourth band energy at W may be raised above the Fermi level. In addition the separation between the second and third bands is changed thus affecting the shape of the hole surface.

To summarize, we see that the addition of the spin-orbit coupling term can be important, helping to empty the fourth band of model A. The band gaps would be modified, but the shape of the fitted surface (third band in this case) would be changed very little.

Figure 11.7. Energy levels at W as a function of the spin-orbit coupling parameter

— — — Model A

———— Model B

